Department of Mechanical Engineering

Design and Implementation of Bio-inspired Underwater Electrosense

Ke Wang

This thesis is presented for the Degree of
Doctor of Philosophy
of
Curtin University

November 2017

Declaration

To the best of my knowledge and belief this thesis contains no material previously published by any other person except where due acknowledgement has been made. This thesis contains no material which has been accepted for the award of any other degree or diploma in any university.

Ke Wang

30/11/2017

Acknowledgements

Studying for a Ph.D. degree is a long way with many hard works and many thanks to all the people connected to me on this journey.

I would first like to thank Dr. Lei Cui, who has always been an encourager and a thoughtful leader. I would also like to thank Prof. Khac Duc Do, who informed me with literature in research and broadened my eyes in many scientific areas. They consistently allowed papers to be my own works but steered me in the right direction by reviewing them patiently.

I would like to acknowledge the undergraduate students and experts in the mechatronic laboratory who were involved in the building prototypes for this research project. Without their participation and input, the experiment could not have been successfully conducted.

I would also like to thank my peer Ph.D. students: Hamed, Zefang, and Thibault. We had many interesting and inspiring talks, and we spent much memorable time together.

Finally, I would like to express my sincere gratitude to my family for their tireless support and constant encouragement in my years of study and research. Without them, this accomplishment is impossible.

Abstract

As humans are moving forward to the deep ocean for resource and adventure, building more flexible, robust and energy-saving sensory systems for future underwater robots is an urgent challenge. Underwater electrosense, manipulating underwater electric field for sensing purpose, is a fast developing technology that is bio-inspired by weakly electric fish. Compared to widely used computer vision and sonar systems, the omnidirectionality and feasibility in turbid and cluttered water enable it to be a significant complementary sensing technology.

In this thesis, we aimed to develop active underwater electrosense for close-range sensing in turbid waters. To achieve this aim, we proposed the following specific objectives: (1) Model the underwater field using proper physical theory and formulate the sensing problem; (2) Design sensing algorithms to localize an object in a 3-dimensional underwater space and to identify objects with similar volume but different edges; (3) Implement the sensor with simulations and prototypes to evaluate sensing algorithms.

We formulated the underwater electric field using electroquasistatic theory and divided the sensing problem into forward and inverse procedures. The environmental impedance distribution is the system parameter, whereas measurements taken on the sensor boundary are observations. To predict observations from parameters is a physically well-posed forward problem. But to infer the parameters of the model from observations is an ill-posed inverse problem, which can be formulated using a probabilistic way that allows for a unified and consistent view.

The first approach used techniques from electrical impedance tomography (EIT) for sensing modeling. The EIT uses versatile finite element method (FEM) as a forward model to calculate observations and representing the environment. An eel-like electrosensor was designed and simulated using proposed techniques. This work explored the feasibility of EIT methods for electrosensor.

The second approach targets on reducing the computational burden of the

forward problem by introducing the method of discrete dipole approximation (DDA). Techniques in light scattering problems were for the first time expanded to active underwater electrosense. We found that only DDA was suitable for conductive mediums. The connection between DDA and a well-known sphere perturbation formula was further established. DDA was found to perform more than 100 times faster than FEM with only a 10% relative difference in underwater electrosense problems.

Based on the fast DDA solution of the forward problem, two types of sensing algorithms, unscented Kalman filters (UKF) and neural networks (NN), were designed to localize and identify an object in front of the sensor. The convolutional neural network (CNN) was for the first time used in underwater electrosense to identify objects with similar volumes but different edges. We built two editions of prototypes to test and validate the planar sensor design and algorithms, including a 5×5 sensor with electronics from National Instrument and a 16×16 sensor driven by a self-made analog signal chain. Experimental results of the first sensor showed that the detection and localization of our prototype were quick and accurate, with the error of around 10 mm using neural network mapping. In the second experimental test, the prototype with 16×16 electrode array achieved an overall success rate of 95.0% on identifying the specified cube, sphere and rod.

Through investigations in this thesis, we found the vast potential of underwater electrosense and laid a solid foundation for applications on practical robots. By further shrinking the electronics and adapting sensing algorithms, artificial electrosense emulating the biological sensing system can be deployed on autonomous underwater robots for monitoring and supervising ecological environment of rivers, lakes or oceans.

Contents

List of Figures

Chapter 1

Introduction

1.1 Active Sensing Techniques

A robot or an intelligent agent (IA) has three functional parts: sensor, processor, and actuator. By collecting environment information and incorporating tasks, actuators are executed following the processing results. Robot's sensors and actuators are coordinated by processing unit that together builds up a sensorimotor loop. The sensing ability, more specifically, is the ability to detect physical entities or their changes in the environment. The physical entities can be sound, light, electric, pressure, heat or other phenomena. But eventually, they are mechanical or electromagnetic waves and can be converted to electrical signals (current or voltage) for processing in electrical circuits.

The IA sensing overview is illustrated in Fig. 1.1, indicating the sensing relationship between IAs and the environment. The IA can passively listen the signal from the environment, or it can actively transmit energy that appeared as some physical entities to the environment and listen to the feedback signal. Two IAs actively transmitting energy between each other create a communication channel through the environment.

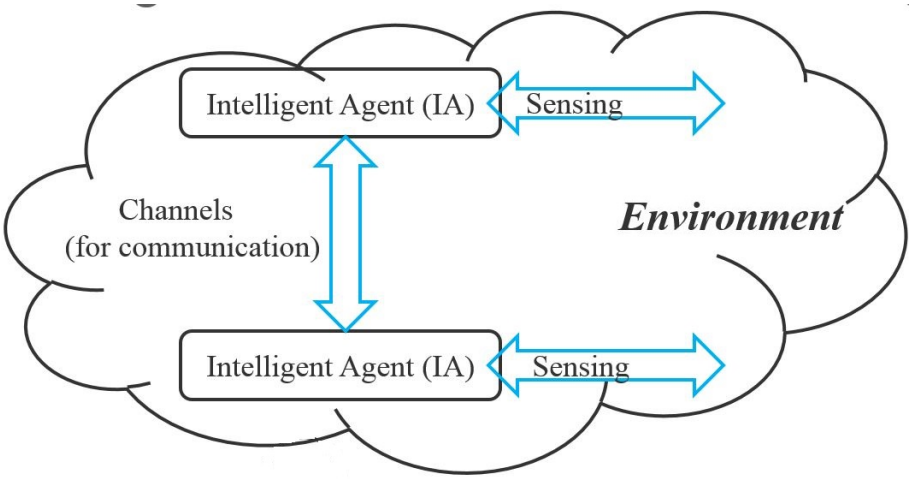

Figure 1.1: *Overview of the IA sensing.*

Active sensing widely exists in animal behaviors. Teleceptive active sensing collects information by propagating energy and detecting objects using cues such as time-of-flight, return signal strength, etc. For example, bat echolocation is an active perceptual system in which ultrasonic sounds are emitted for listening echoes. By comparing the outgoing and the returning signals, bats can get detailed images of its surrounding environment, which allows them to detect, localize, and identify prey in darkness. Whales and dolphins can also use echolocation for hunting and navigation but with a much lower sound frequency to adapt to the underwater conditions. Weakly electric fish uses a self-created electric field to find and localize near-range preys, which will be described in detail later. Contact active sensing uses physical contact between organism and stimuli with examples such as whiskers and insect antennae.

When a man holds a torch to illuminate the road, he is actively using the visionary system for navigation and detection. Modern active sensing technologies include radar in the air, underwater sonar, medical ultrasonography, etc. In this chapter, we first reviewed some active sensing techniques using electromagnetic (EM) field, and we mainly reviewed electric field for sensing purpose in detail.

Then the project topic 'underwater electrosense' was proposed and reviewed with state of the art.

1.2 Electric Field for Sensing

From the vision to radar, electromagnetic wave has been the first-rank sensing medium used by humanity. We are interested in properties of the electromagnetic wave in the liquid water by looking at the diagram of absorption spectrum [96] across a wide wavelength range in Fig. 1.2. Visible light is almost transparent to water perfectly, a property which is good for photosynthesis and production of both oxygen and biomass. Or conversely, the evolution of mechanism of photosynthesis and the ocular system was determined by the electromagnetic wave absorption in the liquid water.

Radar uses radio waves in the air to detect objects and determine their range, angle, or velocity. However, radio waves suffer considerable attenuation in the water, especially in salt water, making them unsuitable for underwater sensing. Currently, fast developing Lidar (light detection and ranging) uses a visible laser to determine a target distance by sending pulsed laser light, and at the same time measuring the time-of-flight and strength of the reflected pulses. There were successful applications of Lidar in underwater environment [62, 42].

Maxwell's equations indicate wherever a magnetic field is propagated then an electric field is presented. Modern smartphones and computers rely on information encoded into the magnetic field (the B field), and many mechatronic devices use Hall Effect sensors to detect positions of metal objects. In this section, we will review some typical applications using the electric field (the E field) for sensing purpose.

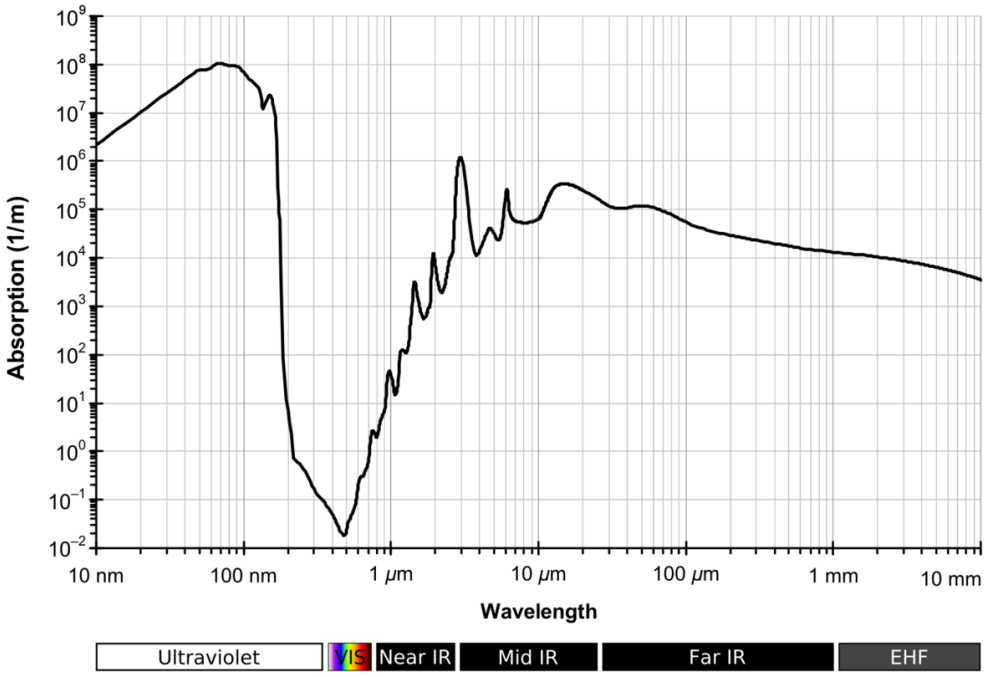

Figure 1.2: *Liquid water absorption spectrum across a wide wavelength range.*

1.2.1 Sensing Applications of Electric Field

Capacitive touchscreens used on modern mobile phones or tablets are the most common implementation of the human hand sensing through the electric field. Same principles were also pursued by Theremin, a type of fancy musical instrument dates back to 1921, which used distortion of the electric field caused by the human body to generate different tones and pitches [83].

The work from MIT Media lab studied using the electric field to track the 3-Dimensional position of two hands without contact, using electric field generated and received by elaborately designed apparatus [76], and they applied it to a robotic hand for pre-touching [77]. These applications make use of the electric field change that is detectable by displacement current, induced by a polarization of the dielectric or charges redistribution of conductors.

Comparably, electrical impedance tomography (EIT) is another example of sensing a self-created electric field, mainly based on the conductive current stim-

ulated by active sources [16]. In the 1920s, resistivity imaging was started to be commonly used by geophysicists who used arrays of electrodes inserted into the earth to estimate a resistive map of the subsurface [29]. It is also a fast developing technology in medical and industrial applications, where internal activities in such as human bodies [70] or oil pipelines [59] can be imaged.

We will see in next chapter that electric fields used in hand-tracking and EIT applications are not a purely static field but a quasi-static field. In other words, the electric field runs at a low frequency that some material properties like conductivity and permittivity, which are used for identifying different objects, can be defined in such situation.

1.2.2 Bio-inspiration of Aquatic Animals

We are interested in looking at nature because some complex problems and their solutions have already been formulated by thousands of years revolution of biological systems. About 70% surface of the earth is covered by water, and the species diversity of aquatic animals is significantly greater than any other group of vertebrates (for example, fish, at 32,000 named species so far) [88]. Living in the dark, noisy, and the cruel underwater world needs more efficient sensing methods to survive. There are two types of vision-less sensory systems (lateral line [26] and electrosensory system [58]) owned by aquatics, among which some live in the deeply dim ocean or completely dark caves, some live in much brighter places like quiet lakes, rivers or along the coasts. Therefore, it is not surprising that the modalities or the organizations of sensors can be quite diverse.

Field sense is a series of sensing ability to acquire information of near-range surrounding environment represented by vector field (flow field or electric field). The lateral line is a hair cell-based sensing system for most fishes or amphibious

to feel the low frequency (less than 200 Hz) flow field caused by turbulent or steady water motion [64]. Electric field sensing system that can feel the low-frequency electric field, however, is much more specialized than the lateral line. Only limited aquatic species hold the ability to passively perceive the electric field and even fewer species called weakly electric fish can actively perceive the self-generating electric field [93, 87]. These signals will be processed by nerves system to instruct different behavioral activities, such as preying, orientation and navigation, communication and schooling.

The examples of aquatic animals here mainly consist of fishes and marine mammals. Besides, numerous mammals are living in or relying on the water, whose ancestors are believed to move into the water from the land by most scientists. Marine mammals like dolphins and whales completely rely on ocean environment for all their lifetime, whereas seals feed in the ocean but breed on land.

The biological sensing mechanism can be divided into several categories according to their physical principles: mechanosensory, chemosensory, electromagnetic sensory and vision system. The reason to classify the vision to a single category is that higher mammals like humans or apes living on the ground heavily rely on their vision for object detection, discrimination, and spatial orientation. Vision seems to become the most sophisticated form of sense because it is tightly connected to the intelligence of mammals. Vision is an enhanced electromagnetic sensory system specifically designed for radiation with a frequency roughly between 400 THz to 790 THz, and it will cost much energy and material in the brain to process the image signals.

But some animals, especially those fishes living in the deep dark world, can survive well without looking at their surroundings, and they even do not waste precious resources developing eyes. It makes sense as an evolutional strategy

to living in in an environment where vision is impractical, useless and even impossible. Take an example of weakly electric fish, the components of an electric sensory system are an exciting source and many electroreceptors. Weakly electric fish evolved an electric organ for to create an active electric field, and thousands of electroreceptors distributed on the skin to sense the deduced transdermal currents. The current distribution is an electrosensory 'image' determined by external objects or other electric fish.

1.2.3 Biological Sensory Systems

Biological sensory systems are sophisticated in energy and materials saving, sensibility and selectivity [88]. Thus, these varied species established excellent sensory models for us to tackle with challenges in continually moving forward. Although the attempt of designing engineering projects or artificial systems by using principles of sensory systems found in nature has existed for a long time, only recently scientists and engineers started to build some prototypes of biomimetic apparatus in the real sense. Due to the advancement of some highly analytical methods and developed technologies that have become available now, on the one hand, the modern molecular biology help to analyze the complicated biological sensory organs and nerves system, and on the other hand the micro- and nano-fabrication technologies in engineering can help to simulate those systems.

The intrinsic widely interrelated biological systems show that there exist some universal principles when nature builds the biological sensory systems [26]. Keeping in mind these principles of naturally built sensory systems is helpful when we study the diversity of biological sensors and think on how to transform them into artificial works.

a) Energy saving. It is the most important part of the secret of living in the

harsh environment. Successful foraging is hard and uncertain, so it is better to evolute the skill of minimizing the energy cost when sensing and hunting.

b) Material saving. Although the sensory systems of animals are varied significantly, the cell types for building these systems are very conservative and refined. Evolution tends to redesign the existing system to realize a new function, or to serve a completely new purpose.

c) Redundancy and Parallelization. There may be hundreds of receptor organs, each of which is built with several receptor cells. These numerous redundant sensor cells work in parallel, not only in the sensory sampling level but also in neural processing level, which will improve the signal-to-noise ratio and reduce the likelihood of errors. The conception of redundancy and parallelization is quite uncommon in artificial systems as we usually built them in a serial way, just as we do in contemporary computing architectures.

d) Specificity. There is no universal method to achieve all the sensing tasks effectively and economically simultaneously; specified sensory function is a reasonable option. Nevertheless, vision system of higher mammals is an exception, as vision is quite universal and cost considerable energy by processing images from eyes. That is a trade-off in evolution, because one of the meanings of the intelligent is the adaptive ability for the environment, being universal means higher and smarter. But for fishes, they will not understand images in the same way with higher mammals, and eyesight is often useless as it is dark under the illimitable ocean.

1.2.4 Biological Electrosense

Electrosense is a biological ability to receive natural electrical stimuli, which has been discovered in many underwater animals including aquatic or amphibious

animals. For example, sharks and catfishes are equipped with the sense of passive electrolocation, which means they can detect and receive electric signals from the environment or other fishes and estimate the location of such signal [41]. Shark has a susceptible electroreception system, which can find preys hidden in sand or mud by sensing the electricity they produce.

Passive electrosense relies upon ampullary receptors which are sensitive to low-frequency stimuli (below 50 Hz). These receptors have a jelly-filled canal leading from the sensory receptors to the skin surface [17].

Living in the dark, noisy, and the cruel underwater world needs more efficient sensing methods to survive. Since Lissmanns discovery [58], experiments on weakly electric fish show that by manipulating the electric sensory system they can exact information of objects in surrounding environment, such as location [93], geometrical properties (size and shape) [90] and electric properties (conductivity and permittivity) [87]. Further, the information will be processed to conduct high-level behaviors such as navigation, prey tracking or hunting, and communication of interspecies [88].

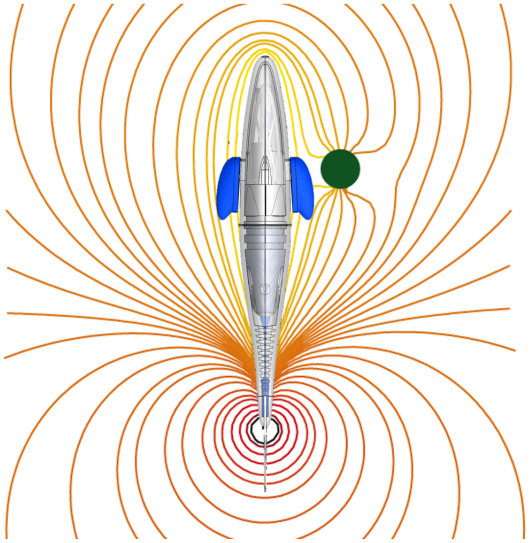

Figure 1.3: *A robotic fish with electrosense. Simulation shows the potential map of weakly electric fish.*

For weakly electric fish, take black ghost knife fish for example, there is a specialized electric organ in their tail to emit electric current, which is called electric organ discharges (EODs). The corresponding self-built electric field, normally effective in 1-2 body length range, encompassing the fish will be distorted by nearby objects that hold different impedance (conductivity and permittivity) other than ambient water, and the perturbations will be perceived by hundreds of cutaneous electroreceptor organs distributed over the skin of fish [40]. As in Fig. 1.3, the electric field surrounding the weakly electric fish is represented by a potential map as in Fig. 1.3.

The term 'weakly' means that the emitted electric field by EOD is not strong, typically less than 1 volt in amplitude. Strongly electric fishes like electric eels or electric rays can generate very invasive electric to stun prey, typically ranged from 10 to 600 volts with the current up to 1 ampere according to the surrounding water conditions [86]. Evidence shows that to guide an attack on a small prey (2 mm) at a distance about one-quarter of a body length, even only 0.1% transdermal voltage change through the fish skin can be sensed, which indicates a very high sensitivity level [66].

Apart from the ampullary electroreceptor organs possessed by all passive electroreceptive fishes, weakly electric fishes have additionally second class of electroreceptor organs, for encoding the phase and amplitude of their EOD signals. This kind of electroreceptor for active electric fish is most sensitive to the own EOD dominant frequencies of the fish. In other words, active electroreception mainly relies upon tuberous electroreceptors which are susceptible to high frequency (20-20,000 Hz) stimuli [97].

In the fishs environment, most objects such as stones and mud are mainly resistive and only change the amplitude of the EOD signals. But living creatures usually have capacitive properties, which will shift the phase of the waveform in

addition to amplitude changes [89]. For an impulse type fish, the detected range of the electrical capacity rely on the duration of its EODs, i.e., shorter EODs detect lower capacitances. There is research confirmed that the frequencies of the EOD signals are related to the range of capacitive values of animated objects of such fishes natural habitat [30].

1.3 Artificial Underwater Electrosense

Sensing by manipulating electromagnetic field, electric field, and the magnetic field is an extensive and interconnected field. This section concentrates on reviewing the directly related state of the art on artificial underwater electrosense - manipulating underwater electric field for sensing purpose, which is the center topic of this thesis. Several technologies have been developed to achieve underwater sensing, including widely used sonar and vision. However, contemporary underwater sensory systems cannot be satisfactory in certain circumstances, especially for those potential applications of future biomimetic fish, as in Fig. 1.3, which is usually envisaged to monitor the aquatic environment naturally and execute tasks that cannot be accomplished by present underwater machines.

Electric field sensing technique is supposed to be outstanding in several aspects. First, electrosense is omnidirectional and operated in near range, so it is quite suitable for navigation in a confined environment. Further, compared to sonar or vision, electrosense can additionally identify the electric properties of the targets, for instance, the difference between a fish-shape stone and another real fish in a similar scale. Second, electrosense is unaffected by light attenuation, which is a severe problem in vision. Besides the high cost of computational energy in processing images, AUVs using vision require tethers for enough power to illuminate in the dark water. Electrosense, however, naturally consumes much

less energy, as the electric field (stimulating current) can be weak. Last but not least, in turbid and cluttered water sonar will fail because of small particles and numerous obstacles caused interfering reflections and diffraction of the signals, whereas electric field sensing system still works well in such situations. Additionally compared to sonar, electrosense operates without any delays, which may lead to some control strategies such like reactive control.

1.3.1 Theoretical Studies

The electric field from the weakly electric fish, considered as perception bubble encircling the fish body, is their material truck's prolongation. Physically speaking, the problem for fish to solve is to recover the factual impedance distribution in that encircling bubble. If the exciting source and the boundary conditions are well defined, Maxwell equations and constitutive relations of materials will determine the distribution of the electric field, which states the forward problem.

In forward problems, numerical techniques such as finite element method (FEM) can be used to solve the partial differential equations (PDEs), i.e., calculating the electric potential on each discrete element with interpolation. An alternative numerical approach is boundary element method (BEM) [8], which can improve the computational speed as the number of nodes dramatically decreased.

For electric sensing system what needs to be solved is an inverse problem, given the exciting sources and field distribution over some specified boundary (fish or robot skin). Due to the ill-posedness character of such inverse problem, it is challenging to try how much information of the surrounding environment that the electric sensing system can reveal. Although in biology researched intensely, the active electric field sensing was infrequently studied in robotic [60].

Perturbation Method

Perturbation model is the most prevalent method in underwater electrosense that have been studied by several research groups. An object entering the near-region is electrically polarized by the original electric field of the sensor. The polarization in return generates a weaker electric field (called perturbation) that superimposes to the original field. When we measure the electric field, the perturbation induces a variation of the measured voltage or current on the electrode.

Different objects have different perturbations regarding their geometrical and electrical properties. In some simplest cases like a sphere or ellipsoid, the perturbation can be calculated in a closed-form formula.

The group headed by Malcolm Maciver from Northwestern University published first paper on the biorobotic electrosensory system in 2001 [61]. This work proposed a sensor model to emulate the electric fish skin and electric organ discharge. Rasnow [68] in 1996 first applied a sphere perturbation formula to model the electrolocation of the fish, called U-U mode by using voltage source as excitation and measuring induced voltages on the boundary, and such model was expended and implemented in later researchers of the same group [80, 79, 73].

The group headed by Frederic Boyer is an energetic player in studying electric field sensing and applications on underwater robots, whose works were supported by project ANGELS (ANGuilliform Robot with ELectric Sense) funded by European Commission [56, 46]. They proposed to measure the current through electrodes on the skin, which was defined as U-I mode, instead of measuring the voltages (U-U mode) with high input impedance. The initial design [10] proposed two theoretical perturbation models of emitter-sensors, including a 2-spheres model and a 4-hemispheres model. They were used for localization of wall obstacles using extended Kalman filter. The perturbation model was based

on the image method.

A sensor composed of several spherical electrodes was designed using poly-spherical model (PSM) [46]. Some spherical electrodes emitted current whereas others acted the role of current-receivers. The ambient environment impedance was described by an analytical formula using voltages and currents measured on all electrodes. This model was tested on objects for which the perturbation expression is known (such as sphere and ellipsoid).

Either 2-spheres model or poly-spherical model, only the electrodes were considered that the sensor body effect (the sensor body that holds electrodes) was neglected. To obtain a semi-analytical solution for the real sensor concerning sensor body effect, reflective model (RM) that developed in the field of small numbers hydrodynamics was used [19, 46]. Then the analytical result was compared with the one came from BEM simulation.

Applications based on perturbation model included studying the obstacle avoidance in a confined underwater environment [23, 73, 27]. A reflex navigation method [23] was designed based on a set of reactive control laws to avoid any ellipsoid made from plastic or metal. In another similar work [73], the sensor was placed in a water tank filled with plastic tubes, and the sensing task is to avoid these tubes when moving. This work used a particle filter to estimate the orientation and an extended Kalman filter to estimate locations. By changing the sensor form into a circle from a pipe, a work [27] used wide-field integration methods to avoid obstacles from all directions. It demonstrated navigation in a straight tunnel.

For object discrimination, the complex impedance can be extracted by measuring both amplitude and phase perturbations due to the presence of objects [14, 12]. Inspired by EOD signals of fishes, a mathematical model [3] for electrolocation of actual fish is derived and simulated using multifrequency MUSIC

(MULtiple Signal Classification) algorithms. In such model, given the shape of targets (disk or ellipse for instance), the size and electric properties can be reconstructed separately.

EIT-based Method

Electrical impedance tomography (EIT) is a category of techniques in clinical, industrial or geophysical applications [18, 39]. It shares similar principles of weakly electric fish to image the inside impedance distribution of the matter by using the electric field. For example, medical EIT uses an array of electrodes wrapped around the portion of the body, and two electrodes are used for injection current and the remaining measure the corresponding voltages. Thorax EIT can be used to look at the lung perfusion and cardiac cycle [24].

For applications in industrial process monitoring, an array of electrodes can be bounded around a pipe to observe the resistance or capacitance variation of the flowing liquid [98]. For geophysical areas, EIT can be used to image the impedance distribution of sub-surface structures for mineral deposit exploration. A planar gridded array of electrodes on the surface of the earth or embedded in boreholes [101].

Methods of EIT are mainly based on the numerical solution using finite element model [65, 11]. The FEM discretizes the continuous domain into non-uniform and non-overlapping elements through nodes. The FEM solves the potentials on nodes and further approximate potentials of other points using interpolating functions. The natural advantages of using FEM in EIT problems come from two aspects: the FEM is a general approach that widely used in solving partial differential equations; the discretized domain is suitable for sensing representation like the matter distribution or object location.

The significant difference between usual EIT applications and underwater

electrosense is whether the sensing domain is open. The work in [78] used an EIT-based method in electrosense for estimation of object position and velocity, and the result was compared with a simpler method using cross-correlation in which a uniform field was assumed. The EIT-based method required heavier computational effort but provide more accurate estimations. There were other open domain EIT applications as well such as geophysical exploration from the surface, breast and skin cancer imaging [49, 38]. In these cases, electrodes are all arranged on a plane and looking at one side. In this thesis, we will study the EIT approach to underwater electrosense for sake of improving works in [78] and evaluate sensing performance under different sensor morphologies.

GPT-based Method

Generalized polarization tensors (GPTs) was proposed and developed by Habib Ammari based on studies of layer potential theory and small volume expansions [6, 4]. The GPTs are the basic building blocks for the asymptotic expansions of the boundary voltage perturbations due to the presence of small conductivity inclusions inside a conductor. Based on this expansion, efficient algorithms to determine the location and some geometric features of the inclusions can be further designed.

The GPTs contain important geometrical information on the inclusion. With each domain, an infinite number of tensors, called the generalized polarization tensors (GPTs), is associated. The GPTs contain significant information on the shape of the domain thus can be used for shape description, and they hold invariance properties under translation, rotation, and scaling [5]. For example, the perturbation of a sphere with a closed-form formula turns out to the simplest GPT of an object.

In a recent work [54], the object was localized by MUSIC algorithm (Mul-

tiple Signal Classification) that was first developed in localization problems of radio wave emitter. And the GPT was used for shape estimation in numerous experiments. The system of estimating shape had an average error of 16%, and self-aligning the sensor with the ellipsoid through a reactive feedback achieves an estimation error of 10%.

1.3.2 Empirical Studies

Theoretical study of electrosense only concern the calculations or simulations, which depend on the ideal measurements and other simplifying assumptions. However, building real underwater electrosensors involves more practical activities. Empirical studies inspired by electric fishes are more concerning the circuit nature, i.e., the quantities of voltage and current that can be measured directly in the circuit.

Artificial electrosensors can be classified by different types of signal (current or voltage) transmissions and measurements. Some biomimetic electrosensors hold voltage between active electrodes and measure currents through probing electrodes (U-I mode) [20, 21, 55, 22], or measure voltages between those probes (U-U mode) [81, 15, 28]. Some others emit current and measure induced voltages (I-U mode) using techniques from electric impedance tomography (EIT) [78, 2].

The number of electrodes of current sensors varied from four [81] to sixty-four [78] and they were much sparser than the biological systems. The biological electrosensory system was found to be sophisticated due to its thousands of extremely sensitive electroreceptors. It can localize the object, estimate the object size, and tell the difference between varied shapes [93, 91]. On the contrary, engineering electrosensors still have a tremendous potential to be improved. Overall, choices on specific configurations mainly rely on the electronics and sensing algorithms

that are used.

Several experiments on applying electric sensing models to robots and exploring corresponding control problems have been conducted. Rasnow [68] proposed a simple method to manufacture the experimental electrode using silver wire and Bunsen burner, and this method was later utilized in the research [80, 79] on a setup of four-point electrodes driven by a rigid Cartesian moving robot, which is a direct implementation of the Rasnow model.

This group then expended such model to a sensor pod, which consists of an emitter/ground oscillating pair on the front and back that generates the electric field and 35 voltage sensing electrodes on the pod's surface to detect the changes of the perturbation [78]. These sensor described above implemented voltage-sensing electrodes (U-U mode) with high input impedance.

The ANGELS project created several generations of experimental pod platforms based on U-I mode model [10, 46, 56], and they designed an underwater reconfigurable robot using this electric field sensing [63]. One such sensor uses seven electrodes and can perform object identification and localization tasks.

As a further application of the electrosensor, a reconfigurable underwater robot [72] was designed. It was an anguilliform (eel-like) swimming robot that can detach into several rigid modules and self-attached using the electric field for docking. Each rigid module is independent and equipped with three propellers, and a swarm of modules can either explore confined environment or combine an eel-like robot to improve perception and locomotion.

Another potential application of underwater electrosense is electric docking stations [22]. For example, a ship is equipped with a electrosensor that can detect the electric field. A docking device with several current receiving electrodes is bounded by insulating walls that shape the electric field. All electric lines converge to a current emitting electrode which turns to be the docking point.

The pre-docking vehicle would follow the electric line to touch the docking point - the current emitting electrode. The is an electric docking process before the mechanical anchoring, and in other words, before the conventional mechanical docking, the electric docking station can be used as an intermediate phase.

1.4 Research Objectives and Methods

The research project proposed in this article is an in-depth theoretical and experimental study on underwater bio-inspired electric field sensing technology, which is aimed to equip the future biomimetic robotic fish or underwater vehicles. Lissmann found that electric field actively generated by weakly electric fish is in fact utilized for spatial visualization and perception, just like vision and sonar (sound echolocation). Since then abundant biological researches on active electric field sensing have revealed more details on features and mechanism behind. Recently, due to the promising applications of electric field sensing system in the severe underwater environment, scientists and engineers started to rebuild such system in artificial ways and apply it to autonomous underwater vehicles (AUVs). The objectives of this research are as follows:

a) Perform the study on the physical mechanism behind the electric field sensing hold by weakly electric fish, and design the feasible artificial model aiming at achieving similar functions of its biological counterpart, including object location and discrimination as well as environment reconstruction.

b) Derive analytical (or semi-analytical) solutions and perform numerical simulations on electric field sensing model. Simultaneously perform studies on the general approach defined as an inverse problem and engineering approaches using simplified sensing models. As this artificial sensor is primarily designed to equip future biomimetic robotic fish, the feasibility of putting into practical application

and operating in real-time should be considered in both hardware and algorithm aspects.

c) Design and construct experimental apparatus and platform suitable for verifying and consummating the production of a) and b).

Several levels of research should be conducted to achieve the goal we anticipate. A complete study on the physical and mathematical mechanism of the electric field sensing comes the first, in which we need to exploit all the possible approaches to reconstruct the ambient environment. What makes the problem more complicated is that electric field sensing is naturally integrated with the locomotion of the fish both in substantial physical mechanism and biological behavior. For instance, black ghost fish evolved into a ventral elongated median fin to swim agilely but can also keep its body relatively stiff, which is assumed to maintain a certain stability of electric field. As a result, when we study the sensing mechanism and sensor design, the model of the motion should be considered as well.

Another level would be an experimental investigation to provide data, with which we can verify and support the claims made from the aforementioned theoretical research. As the close relationship between the sensing principle and the sensor movement, we plan to build a platform driven by a Cartesian robot with an additional rotational freedom.

1.5 Contributions

In this thesis, we aimed to develop active underwater electrosense for close-range sensing in turbid waters. First, we formulated the underwater electric field using electroquasistatic theory and divided the sensing problem into forward and inverse procedures. The open-boundary FEM formulation was an improvement

compared to conventional method in a confined area. The approach of electrical impedance tomography (EIT) to underwater electrosense was successfully implemented, and compared to previous works this approach was extended to complicated cases such as an eel-like electrosensor. Second, we developed a new approach targets on reducing the computational burden of the forward problem by introducing the method of discrete dipole approximation (DDA). Techniques in light scattering problems were for the first time expanded to active underwater electrosense. We found that only DDA was suitable for conductive mediums. The connection between DDA and a well-known sphere perturbation formula was further established. DDA was found to perform more than 100 times faster than FEM with only a 10% relative difference in underwater electrosense problems. Based on the fast DDA solution of the forward problem, two types of sensing algorithms, unscented Kalman filters (UKF) and neural networks (NN), were designed to localize and identify an object in front of the sensor. The convolutional neural network (CNN) was for the first time used in underwater electrosense to identify objects with similar volumes but different edges.

1.6 Overview

This chapter introduced the background and motivation of the artificial underwater electrosense. Chapter 2 formulated the underwater electrosense problem using electroquasistatic equations. The sensing problem was stated as an inverse problem. As the inverse problem was ill-posed and not determined, a unified probabilistic approach under a Bayesian view was formulated. Chapter 3 applied an electrical impedance tomography approach to the underwater electrosense, in which forward problem was modelled using finite element method, and the inverse problem was to reconstruct the variations of conductivity on each grid. Chapter

4 proposed a novel approach to the forward problem of underwater electrosense, discrete dipole approximation, using principles transplanted from light scattering problem. This approach has several advantages compared to finite element method in the context of underwater electrosense, and simulation and experiment validated it. Chapter 5 designed 1-D and 2-D electrosensors. Two categories of sensing algorithms, including unscented Kalman filters and convolutional neural networks, were designed and simulated. Chapter 6 discussed experimental rigs and electronics that used in this project. More experimental results were presented and discussed. Chapter 7 recap and concluded the thesis and outlined future works.

Chapter 2

Problem Formulation

2.1 Introduction

As a weakly electric fish model, the conductivity of internal body (10,000) is much higher than the water (200-500). The skin is thin and less conductive, with conductivity according to different locations on the body. At the tail, the skin is more conductive (50) and gradually reduced to a small number (0.25). It means the current flow from the electric organ cannot penetrate the skin directly, but through the electroreceptors that measure the current spatial distribution on the skin. The electric organ can be treated as a current source, rather than a voltage source [7].

The models of common artificial electrosense have a few differences from the fish. First, the artificial sensor usually uses electrodes as exciting source and electroreceptors as well, and it can measure the field either by current or voltage due to the electronics widely used by us. Second, the artificial source can be controlled regarding current, voltage, or total power.

The classification of current artificial systems can be based on such a voltage-current configuration. We have seen the biomimetic systems by controlling emit-

ting voltage and measuring currents through probes, and also systems by holding emitting voltage and measuring voltages between probes. EIT (Electric Impedance Tomography), which is tightly related to this topic and intensively studied in geophysical and medical imaging techniques, usually emitters control an amount of current into the sensing region and collects the deduced voltages.

This chapter focus on formulating the underwater electrosense problem. Maxwell's equations build a standpoint for all the electromagnetic problems. However, as the field in electrosense has low frequencies, it can be tackled as an electroquasistatic problem. Material's real electrical properties, interactions between the field and the matter, are always complex and need to be tackled approximately.

The electroquasistatic field is a simplification of the full electromagnetic wave when the problem is electrically small, and the main phenomenon is the conductive current. But the field still has a low frequency that can have a phase shift due to displacement current effect. For the pure static case, only objects with different conductivities from water can be sensed; for the electroquasistatic case, permittivity is another electrical property that can be sensed, and the effects of conductivity and permittivity twist with each other.

The electrical properties, including conductivity and permittivity, are assumed to be linear, isotropic, ohmic, and stable with the frequency. This greatly simplifies the problem in the formulation, and it is, in fact, a proper assumption in electrosense. In the real implementation of electrosense, multiple frequencies should be used to plot the magnitude-phase diagram.

2.2 Electroquasistatic Field

Maxwells equations (2.1) fully describe the origin and coupling propagation of the electromagnetic field. Among five equations listed in (2.1), only three of them

are independent. In order to apply Maxwell's equations, the relations between displacement field $\mathbf{D}$ and the electric field $\mathbf{E}$, as well as the magnetizing field $\mathbf{H}$ and the magnetic field $\mathbf{B}$ need to be specified.

$$\begin{aligned} \nabla \times \mathbf{E} &= \partial \mathbf{B}/\partial t \\ \nabla \times \mathbf{H} &= \partial \mathbf{D}/\partial t + \mathbf{J}_f \\ \nabla \cdot \mathbf{D} &= \rho_f \\ \nabla \cdot \partial \mathbf{B} &= 0 \\ \nabla \cdot \mathbf{J}_f &= -\partial \rho/\partial t. \end{aligned} \tag{2.1}$$

First, for linear, isotropic, and ohmic materials that are considered in this section, simple relations (2.2) can be assumed. The relation of free current $\mathbf{J}_f$ and charge ρ is also given as the Ohm's Law.

$$\begin{aligned} \mathbf{D} &= \epsilon \mathbf{E} \\ \mathbf{B} &= \mu \mathbf{H} \\ \mathbf{J} &= \sigma \mathbf{E}, \end{aligned} \tag{2.2}$$

Coefficients are permittivity, permeability and conductivity respectively, describing the field and material interaction at a microscopical level.

Second, if the ratio between the time of traveling longest length-scale of the problem and the smallest time that count, for example, the period of the wave, such case is referred to an electroquasistatic formulation. Which means the field is not purely static, but the frequency is low enough that some simplifications can be applied to the full wave equations.

Following the way in [31] we can define a ratio parameter α for scaled time $\tau = \alpha t$. For static or quasi-static cases, the dynamic process is so fast that a time period t can be compressed into τ with a small number (compression scale) α,

and when α approaches to zero the process approaches to static. Then the field can be Taylor expanded into different orders at variable $\tau = 0$:

$$\begin{aligned}
\mathbf{E}(x,y,z,t) &= \mathbf{E}(x,y,z,\tau,t) \\
&= \mathbf{E_0}(x,y,z,\tau) + \alpha\mathbf{E_1}(x,y,z,\tau) + \alpha^2\mathbf{E_2}(x,y,z,\tau) + ... \\
\mathbf{B}(x,y,z,t) &= \mathbf{B}(x,y,z,\tau,t) \\
&= \mathbf{B_0}(x,y,z,\tau) + \alpha\mathbf{B_1}(x,y,z,\tau) + \alpha^2\mathbf{B_2}(x,y,z,\tau) + ...,
\end{aligned} \tag{2.3}$$

Where

$$\begin{aligned}
\mathbf{E}_0(x,y,z,\tau) &= [\mathbf{E}(x,y,z,\tau,t)]_{\alpha=0} \\
\mathbf{E}_1(x,y,z,\tau) &= \left[\frac{\partial \mathbf{E}(x,y,z,\tau,t)}{\partial\alpha}\right]_{\alpha=0} \\
\mathbf{E}_k(x,y,z,\tau) &= \frac{1}{k!}\left[\frac{\partial^k \mathbf{E}(x,y,z,\tau,t)}{\partial\alpha^k}\right]_{\alpha=0}, k = 1,2,...
\end{aligned} \tag{2.4}$$

For the first equation in (2.1) because $\frac{\partial \mathbf{B}}{\partial t} = \frac{\partial \mathbf{B}}{\partial \tau}\frac{\partial \tau}{\partial t} = \alpha\frac{\partial \mathbf{B}}{\partial \tau}$, we have:

$$\nabla \times \mathbf{E} = -\alpha\partial\mathbf{B}/\partial\tau, \tag{2.5}$$

Substitute (2.3) into (2.5) we have:

$$\nabla \times \mathbf{E}_0 + \alpha(\nabla \times \mathbf{E}_1 + \partial\mathbf{B}_0/\partial\tau) + \alpha^2(\nabla \times \mathbf{E}_2 + \partial\mathbf{B}_1/\partial\tau) + ... = 0, \tag{2.6}$$

Then each item in brackets equals to zero and they are corresponding to different orders of dynamic process with respect to compression variable α:

$$\begin{aligned}
&\nabla \times \mathbf{E}_0 = 0 \\
&\nabla \times \mathbf{E}_1 + \partial\mathbf{B}_0/\partial\tau = 0 \\
&\nabla \times \mathbf{E}_2 + \partial\mathbf{B}_1/\partial\tau = 0.
\end{aligned} \tag{2.7}$$

Same procedures can be applied to other equations in (2.1). In the electroquasistatic case, only zeroth order (2.8) and first order (2.9) we need to deal with.

$$\begin{aligned}
\nabla \times \mathbf{E}_0 &= 0 \\
\nabla \times \mathbf{H}_0 &= \mathbf{J}_{f0} \\
\nabla \cdot \epsilon \mathbf{E}_0 &= \rho_{f0} \\
\nabla \cdot \mu \mathbf{H}_0 &= 0 \\
\nabla \cdot \mathbf{J}_{f0} &= 0,
\end{aligned} \tag{2.8}$$

$$\begin{aligned}
\nabla \times \mathbf{E}_1 &= -\mu \partial \mathbf{H}_0 / \partial t \\
\nabla \times \mathbf{H}_1 &= \epsilon \partial \mathbf{E}_0 / \partial t + \mathbf{J}_{f1} \\
\nabla \cdot \epsilon \mathbf{E}_1 &= \rho_{f1} \\
\nabla \cdot \partial \mathbf{H}_1 &= 0 \\
\nabla \cdot \mathbf{J}_{f1} &= -\partial \rho_{f0} / \partial t.
\end{aligned} \tag{2.9}$$

Start from the zeroth order free charge density ρ_{f0}, which may come from the electrochemistry reaction or other sources in the real world. Noticing that zeroth order field $\mathbf{E}_0$ is induced by ρ_{f0}, if the material is conductive and ohmic, zeroth order current density is simultaneously induced according to $\mathbf{J}_{f0} = \sigma \mathbf{E}_0$. However, the divergence of current density is zero until in the first order equations the movement of free charges gives the current source $\mathbf{J}_{f1}$. In active underwater electrosense, $\mathbf{J}_{f1}$ is the injected current from the electrical organ or electrodes, and $\mathbf{J}_{f0}$ is the mediums conductive current.

As only zeroth order field is significant in electroquasistatic formulation, we can neglect $\mathbf{E}_1$ and $\mathbf{H}_1$. To establish the relation between current and electric field, take divergence of second equations in both orders, and due to the divergence

of curl is zero:

$$\nabla \cdot (\nabla \times \mathbf{H}_0 + \nabla \times \mathbf{H}_1) = \nabla \cdot (\epsilon \partial \mathbf{E}_0 / \partial t \ + \mathbf{J}_{f0} + \mathbf{J}_{f1}) = 0. \tag{2.10}$$

The term $\mathbf{J}_d = \epsilon \partial \mathbf{E}_0 / \partial t$ is the so-called displacement current. Substitute $\mathbf{J}_{f0} = \sigma \mathbf{E}_0$ into (2.10):

$$\nabla \cdot (\epsilon \partial \mathbf{E}_0 / \partial t \ + \sigma \mathbf{E}_0) = -\nabla \cdot \mathbf{J}_{f1} = \partial \rho_{f0} / \partial t. \tag{2.11}$$

Set $\mathbf{E}_0 = \bar{\mathbf{E}}_0 e^{i\omega t}$, ω is the angular frequency:

$$\nabla \cdot (\sigma + i\omega\epsilon)\mathbf{E}_0 = -\nabla \cdot \mathbf{J}_{f1} = \partial \rho_{f0} / \partial t. \tag{2.12}$$

As we neglect higher order electric field and $\nabla \times \mathbf{E}_0 = 0$ that $\mathbf{E}_0$ is irrotational, electric potential u can be define to be $\mathbf{E}_0 = \nabla u$:

$$\nabla \cdot (\sigma + i\omega\epsilon)\nabla u = -\nabla \cdot \mathbf{J}_{f1} = \partial \rho_{f0} / \partial t. \tag{2.13}$$

For the space with no current source or free charges we get Laplace equation:

$$\nabla \cdot (\sigma + i\omega\epsilon)\nabla u = 0. \tag{2.14}$$

It is worth pointing out that in the electroquasistatic case, although we do not need to consider higher order coupling effect of electric field and magnetic field, the zeroth order magnetic field caused by the conductive current is significant according to second equation of the zeroth order in (2.8). It contains information on current density distribution according to the Biot-Savart Law. Thus, for an artificial underwater electrosense problem, besides the current and potential

measurement, we can also measure the magnetic field.

The most significant difference of the underwater electroquasistatic field, compared to the traditional DDA approach situation, is its dominant conductive current or volume conduction as the term used in bioelectromagnetism. That is to say, the conductivity contrast between the invaded object and ambient water is the first rank parameter we are interested in. The actual conductivity of water in weakly electric fish can vary from about 0.05 S/m (fresh water) to 5 S/m (sea water) depending on the water salinity. It can be seen that this conductivity is moderate among the isolators, metals or other living things.

Only displacement current is considered in pure polarization process like light scattering problems. Underwater electrosense can also use the information of the permittivity, which is the macroscopical indication of the polarizability of objects molecules. Water (H_2O) is the most common high polarizability substance with a relative permittivity of 80 at 20 degrees Celsius, and most solid matter hold relative permittivity of only below 10, such as stone, concrete, glass or wood. Biological experiments support the supposition that weakly electric fish can distinguish the small variance of objects permittivity.

2.2.1 A Dielectric Sphere in a Uniform Field

Solving the partial differential equation in (2.14) needs numerical methods. In some simple cases, closed-form solutions also exist.

As in Fig. 2.1, consider a passive sphere without net charges of conductivity and permittivity σ_s and ϵ_s completely immersed in ambient medium of σ_m and ϵ_m in a uniform electric field $\mathbf{E}_{init} = \bar{\mathbf{E}}_{init} e^{i\omega t}$, represented in a spherical coordinate system. The relation of tangential components of inside sphere electric field $\mathbf{E}_s$ and outside sphere electric field $\mathbf{E}_m$ can be obtained by imaging a rectangular

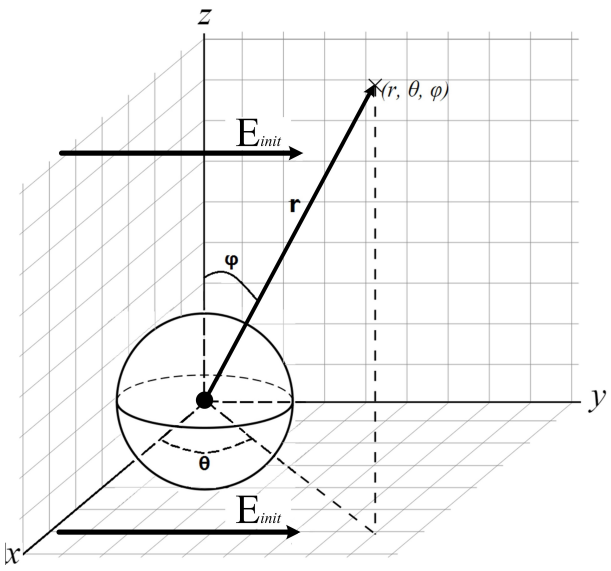

Figure 2.1: *A dielectric sphere in a uniform field*

contour C, partly in sphere and partly in medium. The contour is oriented that its normal is tangent to the surface. Then Stokess theorem [44] can be applied to obtain:

$$\mathbf{n} \times (\mathbf{E}_s - \mathbf{E}_m) = 0. \tag{2.15}$$

In (2.15) $\mathbf{n}$ is the normal vector of the interface. It means that at any point of the interface tangential components of each sides electric field are equal, otherwise $\mathbf{n} \times (\mathbf{E}_s - \mathbf{E}_m)$ will not vanish:

$$E_s^{\tan} = E_m^{\tan}. \tag{2.16}$$

The relation of normal components of electric field and on each side can be obtained in the similar way by imaging a Gaussian pillbox, partly in sphere and partly in medium. Apply divergence theorem to obtain:

$$\epsilon_s E_s^{norm} - \epsilon_m E_m^{norm} = \rho. \tag{2.17}$$

In (2.17) ρ is the net charge density on the interface of the Gaussian pillbox. Taking derivation against time on both sides and referring to charge conservation law we can obtain:

$$\epsilon_s \partial E_s^{norm}/\partial t \ + \sigma_s E_s^{norm} = \epsilon_m \partial E_m^{norm}/\partial t \ + \sigma_m E_m^{norm}. \tag{2.18}$$

The problem of a sphere in a uniform electric field remains to solve Laplace equation (2.14) on both sides of the interface while satisfying boundary conditions (2.16) and (2.18). Due to the azimuthal symmetry of the problem, azimuth angle φ will be irrelevant when writing the Laplace equation in a spherical coordinate, giving rise to a Legendre series solution on both sides. We adopt the analytical scheme using this approach in [44]:

$$\delta u(\mathbf{r}) = k\mathbf{E}_{init}\mathbf{r}(a/r\ )^3, \tag{2.19}$$

$$k = \frac{(\sigma_s + i\omega\epsilon_s) - (\sigma_m + i\omega\epsilon_m)}{(\sigma_s + i\omega\epsilon_s) + 2(\sigma_m + i\omega\epsilon_m)}. \tag{2.20}$$

Eq. (2.19) describes the potential perturbation caused by the sphere of radius a at a point $\mathbf{r}$ originated from the sphere center, and k in (2.20) is a contrast coefficient (also called polarization coefficient) depending on the electrical properties of the sphere and ambient medium. Specifically, in the extreme situations of isolating or perfect conducting objects k hold the limit values of -0.5 and 1 respectively.

It can be replaced by an electric dipole perturbation with the moment $\mathbf{p} = 4\pi\epsilon k a^3 \mathbf{E}_{init}$:

$$\delta u(\mathbf{r}) = \frac{1}{4\pi\epsilon}\frac{\mathbf{p}\cdot\mathbf{r}}{r^3}. \tag{2.21}$$

Then the electric field perturbation due to the sphere is the negative gradient

of the potential perturbation, leading to:

$$\delta\mathbf{E}(\mathbf{r}) = \frac{a^3 k}{r^3}(3(\mathbf{E}_{init} \cdot \hat{\mathbf{r}}) \cdot \hat{\mathbf{r}} - \mathbf{E}_{init}). \tag{2.22}$$

According to (2.17), there will be opposite net charges on each side of the spherical surface. These net charges have two different mechanisms, and the dominant one in underwater electrosense originates from the conductive current flowing between materials with different conductivities. The other comes from the ensemble effect of polarized molecules, i.e., the microscopically activities of permittivity.

2.3 Forward and Inverse Problems

In many engineering or science problems, a system (a robot or any dynamic system) is described using a set of parameters, and a model (very often, mathematical equations) is used to represent relations between these parameters (model parameters). To infer information about such a system, because model parameters may not be measured directly, we can use other observable parameters that have relations with system parameters.

The forward problem is defined as calculating observable parameters from known system parameters, and the inverse problem is to infer system parameters using known observations. The model parameters can completely describe the system. Thus the forward problem is easier to formulate and solve. In another word, the causality or the nature of physical systems guarantee the well-posedness of the forward problem. However, the observable parameters usually do not completely describe the system, and the inverse problem is often ill-posed.

For sensing problems, the collected data is limited, and we always want to

reveal more about the system from the limited data. Hence, sensing is usually an inverse problem and ill-posed.

Manipulating electric field on sensing purpose is a challenging task. It is an inverse problem that the electric field is observed at some boundary points, electroreceptors on the fish skin for example, and then perturbation sources originating from the inhomogeneous objects need to be revealed (see Fig. 2.2).

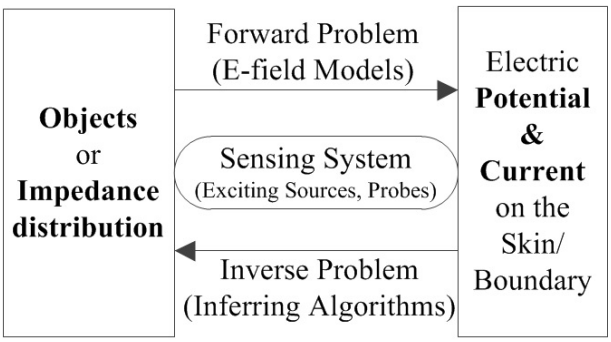

Figure 2.2: *Forward and inverse problem of underwater electrosense*

Solving the inverse problem is based on solving the forward problems, i.e., to predict the observations given the sources. If a forward model is well studied, some iterative inferring techniques like optimal estimators may be developed to dynamically minimize the difference between the model predictions and real observations.

Therefore, a complete solution of the underwater electrosense problem at least includes a forward model and an inversely inferring method. Unlike visible light or X-ray that propagate in line-of-sight, the forward problem of static electric field does not have an easy solution, except in highly simple and symmetric situations such as an infinite plane or a perfect spherical conductor where image method can be applied. Otherwise numerical solvers are necessary under general boundary conditions.

2.4 Framework of Solutions

Because the inverse problem is usually not a determined problem as most forward models, the formulation using a probabilistic way allows for a unified and consistent theory of inverse problems. Some proper apriori information is incorporated to decrease the ill-posedness to tackling an ill-posed problem.

The system described using a vector with M model parameters is defined in a $\mathbb{R}^M$ space called model space, and a vector with D observable parameters is defined in a $\mathbb{R}^D$ called data space. A specified and static system is a point in the model space. A set of observations is a point cloud in the data space, due to the measurement uncertainty.

2.4.1 Probability Basics

A measure over an arbitrary space, for example $\mathscr{M} \subset \mathbb{R}^M$, is that any subset $\mathscr{M}_i$ associates a positive real number $P(\mathscr{M}_i)$ and satisfies following axioms:

(a) $P(\emptyset) = 0$,

(b) If $\mathscr{M}_1, \mathscr{M}_2, ..., \mathscr{M}_n$ are disjoint sets in $\mathscr{M}$, then

$$P(\sum_i \mathscr{M}_i) = \sum_i P(\mathscr{M}_i). \tag{2.23}$$

if $P(\mathscr{M})$ is finite, P is termed as probability. A function $p(\mathbf{m})$ of a vector variable $\mathbf{m} \in \mathbb{R}^M$ that for any $\mathscr{M}_i$:

$$P(\mathscr{M}_i) = \int_{\mathscr{M}_i} p(\mathbf{m}) d\mathbf{m}, \tag{2.24}$$

is called probability density function (pdf), or a probability distribution. It can be normalized by letting $P(\mathscr{M}) = 1$.

For two vectors $\mathbf{m}$ and $\mathbf{d}$ of two arbitrary spaces $\mathscr{M} \subset \mathbb{R}^M$ and $\mathscr{D} \subset \mathbb{R}^D$, a

function is called joint probability density function if for any subset $\mathscr{M}_i$ and $\mathscr{D}_i$:

$$P(\mathscr{M}_i, \mathscr{D}_i) = \int_{\mathscr{M}_i \mathscr{D}_i} p(\mathbf{m}, \mathbf{d}) d\mathbf{m} d\mathbf{d}. \tag{2.25}$$

It can be normalized by letting $P(\mathscr{M}_i, \mathscr{D}_i) = 1$. The marginal probability density function for $\mathbf{m}$ is defined as:

$$p(\mathbf{m}) = \int_{\mathscr{D}} p(\mathbf{m}, \mathbf{d}) d\mathbf{d}. \tag{2.26}$$

The conditional probability density function for $\mathbf{m}$ given $\mathbf{d}$ is defined as:

$$p(\mathbf{m}|\mathbf{d}) = \frac{p(\mathbf{m}, \mathbf{d})}{\int_{\mathscr{M}} p(\mathbf{m}, \mathbf{d}) d\mathbf{m}}. \tag{2.27}$$

From (2.26) and (2.27), the Bayes theorem is deduced:

$$p(\mathbf{m}, \mathbf{d}) = p(\mathbf{m}|\mathbf{d}) p(\mathbf{d}) = p(\mathbf{d}|\mathbf{m}) p(\mathbf{m}). \tag{2.28}$$

2.4.2 Bayesian Formulation

Unlike frequentist probability, the view of Bayesian interpretation assumes the existence of a 'true' state of model parameters, and the possibility is defined as a degree of knowledge (or state of information) about the true state. For example, the degree of knowledge of a system is described by a possibility density over the model space $\mathbb{R}^M$. The extreme case is a determined system whose state $\mathbf{m}$ equals to $\mathbf{m_0}$:

$$p(\mathbf{m}) = \delta(\mathbf{m} - \mathbf{m_0}). \tag{2.29}$$

In (2.29) δ is the Dirac delta function. For general cases, there is a dispersion of the density, for example, Gaussian normal distribution. There are also more

complicated cases that the distribution may be multimodal. The lowest state of knowledge is the state of the non-informative probability density, for a Cartesian and finite space, in which density is uniform:

$$p(\mathbf{m}) = constant. \tag{2.30}$$

From the Bayesian view, solving the inverse problem is to reveal the conditional probability distribution in model space given the probability distribution in data space $\Gamma(\mathbf{m}|\mathbf{d})$. The Bayesian formulation of inverse problem is expression as follows:

$$\Gamma(\mathbf{m}|\mathbf{d}) = \frac{\Theta(\mathbf{d}|\mathbf{m})\Pi_M(\mathbf{m})}{\Pi_D(\mathbf{d})}, \tag{2.31}$$

According to Bayesian formulation (2.31), there are three sources of information for solving inverse problem: forward model $\Theta(\mathbf{d}|\mathbf{m})$, observations $\Pi_D(\mathbf{d})$, and a priori information $\Pi_M(\mathbf{m})$.

In a general Bayesian terminology, $\Gamma(\mathbf{m}|\mathbf{d})$ is the posterior probability, $\Theta(\mathbf{d}|\mathbf{m})$ is the likelihood, $\Pi_M(\mathbf{m})$ is the prior probability ,and $\Pi_D(\mathbf{d})$ is the marginal likelihood or "model evidence".

The forward model is used to predict the values of observations $\mathbf{d}$ given the model parameters $\mathbf{m}$. This prediction strictly should be a probability distribution due to the uncertainty (or errors) of the model. However, the forward problem is often taken as a determined case in (2.29) if we have confidence. But we can endow some uncertainties to the forward model as well, or the forward model can naturally be a probability model.

Measurements reflect the probability distribution $\Pi_D(\mathbf{d})$ over the data space. In Bayesian words, measurements give a certain degree of information about the true values of observable parameters.

Prior $\Pi_M(\mathbf{m})$ is an independent source of information from the forward model and observations. It is a probability distribution defined in the model space. If nothing is known, it will be the case of (2.30). Constraints on acceptable values for the model parameters are common prior information. For example, mass in the real physical system is always positive.

The Bayesian formulation is a general framework for solving inverse problems. In the following chapters, the EIT approach is based on inverse formulation of FEM method. And the sensing algorithms including Kalman filters are also based on this formulation, in which the forward problem is solved by DDA method.

2.5 Conclusion

This chapter first formulated the underwater electrosense problem using electroquasistatic equations. This formulation, though significantly simplified the full wave equations, is still a partial differential equation and numerical methods should be considered. The simplest case of a dielectric sphere surrounded by the medium in a uniform field has a closed-form result.

Second, the sensing problem was stated as an inverse problem. The forward and inverse problems in underwater electrosense were illustrated. As the most inverse problem is ill-posed and not determined, a unified probabilistic approach under a Bayesian view was formulated.

Chapter 3

An Electrical Impedance Tomography Approach

3.1 Introduction

The approach of EIT follows a general framework for solving inverse PDE problems. As formulated in the previous chapter, the forward problem of underwater electrosense is to solve the Laplace equation in an open domain. EIT approach solves the forward problem using finite element method which consists in discretizing the domain into some non-uniform, non-overlapping elements connected via nodes. The finite element method is very versatile with regards to boundary conditions, to the domain geometry and to the heterogeneity of the domain where each element can be assigned a value indicating conductivity. Given the stimulating current and conductivities on meshes, FEM calculates the potential and current field, including the voltage between electrodes which predict real measurements. The inverse problem is to assign a proper conductivity value to each element, which is called reconstruction in EIT, to make the calculations best fit the real measurements. The meaning of 'best fit' can be expressed in an

optimization problem based on the probabilistic formulation.

This chapter first proposed a FEM model for underwater electrosensor. By considering electrodes and boundary conditions, including a far-field virtual boundary, a linear algebra system was deduced to calculate voltages on electrodes. This is a determined forward model of the problem. Second, several solutions of the inverse problem (or sensing problem) were proposed, including linear, non-linear, and dynamic formulations of the inverse problem. The inverse reconstruction can be processed on the same mesh with the forward FEM model, or on a uniform and fixed mesh that are independent of FEM model. Simulations of EIT approach to the underwater electrosense problem were conducted in both cases.

3.2 Forward Problem

3.2.1 Electrodes and Boundary Conditions

From the previous chapter, the underwater electroquasistatic field is formulated as:

$$\nabla \cdot (\sigma + i\omega\epsilon)\nabla u = -\nabla \cdot \mathbf{J}_{f1} = \partial\rho_{f0}/\partial t. \tag{3.1}$$

For the space with no current source or free charges we get Laplace equation:

$$\nabla \cdot (\sigma + i\omega\epsilon)\nabla u = 0. \tag{3.2}$$

The underwater electrosense or EIT problems are inverse problems of partial differential equations using space and time as variables. Environment representation is a discrete and non-overlapping domain. In this case, given the current injections through the electrode boundaries and the conductivities assigned to

each grid, a forward model is derived to predict the voltage measurements on other electrodes.

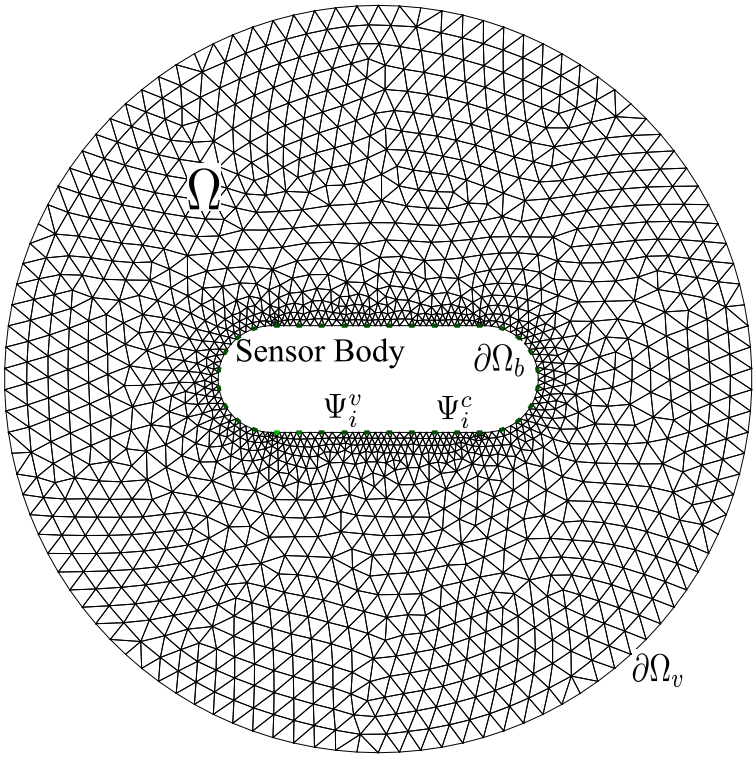

Figure 3.1: *A FEM model of underwater electrosensor.*

An underwater electrosense FEM model is illustrated in Fig. 3.1. An insulated sensor body with boundary $\partial\Omega_b$ was surrounded by conductive water. A virtual boundary $\partial\Omega_v$ is defined in the far field, and due to the far-field assumption, there is no current flowing through the virtual boundary $\partial\Omega_v$. The sensor body and virtual boundaries are combined to be boundary $\partial\Omega$, in which the domain Ω is discretized into non-overlapping triangles.

Electrodes including N electrodes for injecting currents $\{\Psi_1^c, ..., \Psi_N^c\}$ and M electrodes for measuring voltages $\{\Psi_1^v, ..., \Psi_M^v\}$ are belong to boundary $\partial\Omega_b$. The overall current injected from electrode Ψ_i^c is I_i, and the voltage measured on electrode Ψ_i^v is V_i, and I_i^c is the current injected.

Equations formulating the model of Fig. 3.1 using complete electrode model

(CEM) (cite) are listed in (3.3), where Z_i^v and Z_i^c are contact impedance of electrodes, and V_i^v and V_i^c are predicted measured voltage on electrodes.

$$\nabla \cdot \sigma \nabla u = 0, \tag{3.3a}$$

$$u + Z_i^v \sigma \frac{\partial u}{\partial \mathbf{n}} = V_i^v, i = 1, ..., M \tag{3.3b}$$

$$u + Z_i^c \sigma \frac{\partial u}{\partial \mathbf{n}} = V_i^c, i = 1, ..., N \tag{3.3c}$$

$$\int_{\Psi_i^v} \sigma \frac{\partial u}{\partial \mathbf{n}} = 0, i = 1, ..., M \tag{3.3d}$$

$$\int_{\Psi_i^c} \sigma \frac{\partial u}{\partial \mathbf{n}} = I_i^c, i = 1, ..., N \tag{3.3e}$$

$$\sigma \frac{\partial u}{\partial \mathbf{n}} = 0 \quad \text{on} \quad \partial\Omega \setminus \{\{\cup_{i=1}^N \Psi_i^c\} \cup \{\cup_{i=1}^M \Psi_i^v\}\}, \tag{3.3f}$$

$$\sum_{i=1}^{M} V_i^v = 0, \tag{3.3g}$$

$$\sum_{i=1}^{N} I_i^c = 0. \tag{3.3h}$$

The first equation (3.3a) is electroquasistatic field. Other equations from (3.3b) to (3.3h) are all boundary conditions, where (3.3b) and (3.3c) consider contact impedance using CEM, (3.3d) and (3.3e) indicate current flowing through electrodes, (3.3f) express no current flow through sensor body or vitual boundaries except electrodes, and (3.3g) and (3.3h) represent overall current and voltage on electrodes by applying charge conservation law.

3.2.2 Finite Element Formulation

The FE method consists in discretizing the domain into some non-uniform, non-overlapping elements connected via nodes. The dependent variable is approximated within each element by an interpolating function, defined by the values of

the variable at the nodes of the element. The Galerkin principle is then used to turn the original PDE into a set of integral equations for each nodal value. By combining the equations over the domain, the electric potential u at each node can be expressed in matrix notation Au = b.

For a domain discretized as in Fig. 3.1, let the electric potential on nodes to be ϕ_i. Then the electric potential of the whole domain can be expressed by a function $\tilde{u}$ with variables ϕ_i and nodes locations. If each node associates a nodal basis function ζ_i (a polynomial interpolating function) that values one at the node itself and values 0 at other nodes. The function $\tilde{u}$ can be expressed as a linear combination:

$$\tilde{u} = \sum_{i=1}^{W} \phi_i \zeta_i. \tag{3.4}$$

In (3.4), W is the number of all nodes. It should be noticed that the potential field of each element (a triangle) is determined by its nodes due to the non-overlapping of grids and feature of the nodal basis function. However more generally, elements can be quadrilateral, and the tent-like nodal basis function may not vanish at its closest neighbors.

The next step is to solve potentials of nodes, which should satisfy (3.1a) with a residual r:

$$\nabla \cdot \sigma \nabla \tilde{u} = r. \tag{3.5}$$

By composing a weighted average of the residual $\int_\Omega r_i w_i$ over the entire domain Ω that vanishes to zero, we can determine W unknown node potentials. The Galerkin criterion uses the function ζ_i as the weighting function w_i. Further, as the equation (3.1a) holds for anywhere, we can consider the whole domain Ω and a single element E_j:

$$\int_\Omega [\nabla \cdot \sigma \nabla \tilde{u}] \zeta_i = 0, i = 1, ..., W. \tag{3.6}$$

$$\int_{E_j} [\nabla \cdot \sigma \nabla \tilde{u}] \zeta_i^{loc} = 0, j = 1, ..., V, i = 1, ..., C. \tag{3.7}$$

where ζ_i^{loc} is the local nodal basis function with its index (node number) $C = 3$ for a triangular element, and V is the number of elements. Boundary conditions for elements underneath electrodes ψ can be expressed by applying Gauss' theorem to (3.7):

$$\int_{E_j} \sigma \nabla \zeta_i^{loc} \cdot \nabla \tilde{u} - \int_{\Psi} \zeta_i^{loc} \sigma \frac{\partial \tilde{u}}{\partial \mathbf{n}} = 0, j = 1, ..., V, i = 1, ..., C. \tag{3.8}$$

By using boundary conditions (3.3b-e) to the electrode formulation (3.8), the model will have W+M+N unknown variables (potentials on W nodes and M+N electrodes) and equations. Substituting $\tilde{u}$ and arranging equations in a matrix form, following linear system can be deduced:

$$\mathbf{Sp} = \mathbf{c}. \tag{3.9}$$

Where $\mathbf{p}$ is the potential of nodes and electrodes, $\mathbf{S}$ is the system matrix completely determined by conductivity distribution, domain geometry, and the choice of nodal basis function, and $\mathbf{c}$ is the current injected from the specified electrodes. Due to the form of this equation, $\mathbf{S}$ is also called the system admittance matrix. Given the specified grid, the potential $\mathbf{p}$ can be calculated using $g(\boldsymbol{\sigma}) = \mathbf{S}(\boldsymbol{\sigma})^{-1}\mathbf{c}$, where $\boldsymbol{\sigma}$ is the discrete conductivity assigned to each grid.

3.2.3 Ansys Simulation

ANSYS was used to simulate an underwater electrosensor with two electrodes on each side, as in Fig. 3.2. The simulation was conducted in 2-D, where the sensor length is 300 mm and width is 40 mm with a semicircle electrode (diameter 40 mm) on each side. As for conductivity and relative permittivity, water was set

to be 0.05 s/m, and 80, the sensor body and a sphere object were set to be 0 s/m and 2.5. The stimulating voltage between two electrodes was 24 V. Fig. 3.2 illustrated how current flow and potential fields were distorted by an insulating sphere. The current density field in such sensor is extremely not uniform, where the closer to the electrode the stronger the current density is. As a result, the sensor is only sensitive to those objects nearby.

ANSYS is a commercial software in which basic electric field simulation can be conducted. We use ANSYS to fast validate the field morphology of electrosensor. The following NETGEN+EIDORS simulation is a MATLAB based software package which is the main tool used in this work. Using such a tool we can quantitatively study electric field of electrosensor designed with electrodes.

3.3 Optimization Based Inverse Problem

The forward problem solved by FEM is well-posed according to the formulation in the previous section. There is a determined forward model $h(\boldsymbol{\sigma})$ that can calculate predictions of observations $\mathbf{d}$ of the system given the conductivity $\boldsymbol{\sigma}$. However, the simple classical solution of $h(\boldsymbol{\sigma}) - \mathbf{d} = 0$ often does not exist. Practically, the modeling and measurement errors may make the data out of the function range. Mathematically, the inverse problem is often ill-posed in the Hadamard sense [84]. The common approach defining the solution of the inverse problem is the least squares method (LSM).

3.3.1 Linear Inverse Problem

If the forward model is linearisable by Tyler expansion at a specified reference point $\boldsymbol{\sigma}_1$, for $\Delta\boldsymbol{\sigma} = \boldsymbol{\sigma}_2 - \boldsymbol{\sigma}_1$ is small. And he differential inverse can be used to

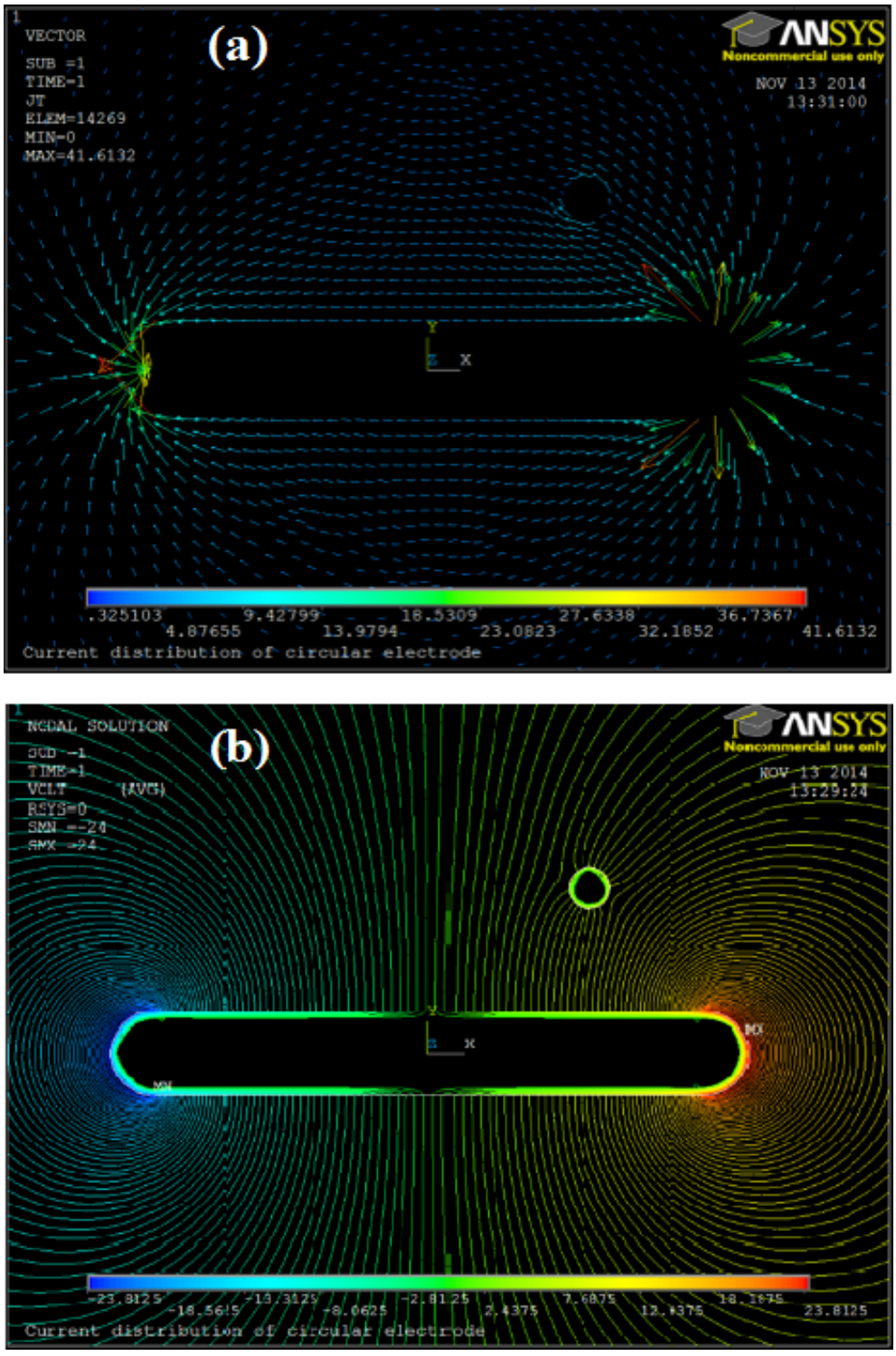

Figure 3.2: *(a) FEM simulation of a pod using ANSYS, indicating a current flow with an intruding insulated sphere. (b) Potential field distribution based on FEM simulation.*

reconstruct a change from that point with a linear formulation:

$$h(\boldsymbol{\Delta\sigma}) = J(\boldsymbol{\sigma}_1)\Delta\boldsymbol{\sigma}, \tag{3.10}$$

$$\Delta\boldsymbol{\sigma}' = \operatorname{argmin} \|J(\boldsymbol{\sigma}_1)\Delta\boldsymbol{\sigma} - \mathbf{d}\|^2 + \alpha L\Delta\boldsymbol{\sigma}. \tag{3.11}$$

The matrix J is calculated as the Jacobian at $\boldsymbol{\sigma}_1$, which is also called sensitive matrix because it relates the perturbation of data and change of conductivity. The regularization item $\alpha L\Delta\boldsymbol{\sigma}$ is used, and α called hyperparameter is a small positive number. The solution of problem (3.11) is:

$$\Delta\boldsymbol{\sigma} = (J^T J + \alpha L^T L)^{-1} J^T \Delta\mathbf{d}. \tag{3.12}$$

Where $(J^T J)^{-1} J^T$ is a pseudo-inverse and the item $\alpha L^T L$ is the regularization. In this case, regularization adds a perturbation to $J_T J$ to reduce the condition number of the matrix and make it less singular. The rationale of using differential inversion is to lessen the effect of measurement errors by taking the difference between two measurements with same system errors.

3.3.2 Non-linear Inverse Problem

The absolute inverse is attempting to reconstruct the real value of conductivity. Following formulation is satisfied:

$$\boldsymbol{\sigma}' = \operatorname{argmin} \|h(\boldsymbol{\sigma}) - \mathbf{d}\|^2 + \alpha F(\boldsymbol{\sigma}). \tag{3.13}$$

Where $F(\boldsymbol{\sigma}) \geq 0$ is the Tikhonov regularization functional that endow a priori to $\boldsymbol{\sigma}$. For example, for l_2 norm regularisation, $F(\boldsymbol{\sigma}) = \|L\boldsymbol{\sigma}\|^2$ or $F(\boldsymbol{\sigma}) = \|L(\boldsymbol{\sigma} - \boldsymbol{\sigma}_0)\|^2$ where $\boldsymbol{\sigma}_0$ is a known prior estimate.

The absolute inverse is a non-linear problem and can be solved by iterative techniques like Newton's method. In each iteration, a linear formulation and solution like (3.12) is calculated to approach the non-linear solution.

3.3.3 Dynamic Formulation

In either linear or non-linear inverse formulations, the system is assumed to not change when acquiring a single set of data $\mathbf{d}$. However, this assumption is not proper when the sensor is moving fast. In dynamic formulation [51], the conductivity changes between different stimulating patterns but remains stable during a single pattern acquisition. The sensing problem is formulated as a state estimation problem, where the conductivity is the state and subject to location and time:

$$\boldsymbol{\sigma}^{t+1} = F^t \boldsymbol{\sigma}^t + \mathbf{w}^t, \tag{3.14}$$

$$\mathbf{d}^t(\boldsymbol{\sigma}^t) - \mathbf{d}^t(\boldsymbol{\sigma}_0^t) = J^t(\boldsymbol{\sigma}_0^t)(\boldsymbol{\sigma}^t - \boldsymbol{\sigma}_0^t) + \boldsymbol{\nu}^t. \tag{3.15}$$

In state evolution model (3.14), where F is the transition matrix that can be deduced from the sensor motion. And $\mathbf{w}$ is a noise process. In observation model (3.15), $\mathbf{d}^t$ is the part of data collected at time t, and J^t is the Jacobian of that part of data. $\boldsymbol{\nu}^t$ is the measurement noise.

3.4 Simulations and Discussions

In this section, we designed an underwater electrosensor and simulated its sensing ability by applying principles of EIT. We adopted NETGEN [71] as a mesh generator and the framework of forward and inverse solvers in EIDORS [2].

3.4.1 A Simple Sensor

A simple electrosensor as shown in Fig. 3.1 was implemented to sense a disk in conductive water. The forward and inverse problems were both simulated in 2-dimension. The virtual boundary was a circle with diameter 2 m, and the sensor was centered in the sensing domain with length 0.6 m and width 0.2 m. The disk was insulated (conductivity 10^{-15} S/m) with a radius of 0.1 m, and the water conductivity was set to be 1 S/m. The stimulating current was 0.01 A. There are overall 36 electrodes distributed evenly along the sensor boundary, including 10 on each straight side and 8 on each semi-circular curve.

The forward calculating model and the inverse sensing model are not necessary to be the same. It is a 'dual model' to avoid so-called 'inverse crime' in simulations if we use a denser forward model and a coarser inverse model [57]. For example as shown in Fig. 3.3, the reconstruction of a fly-by disk was conducted on a fixed grid using GREIT method [1]. In this approach, FEM meshes illustrated in Fig. 3.1 was used for the forward calculation, but the meshes in reconstruction were uniform with a 64×64 grid and kept unchanged.

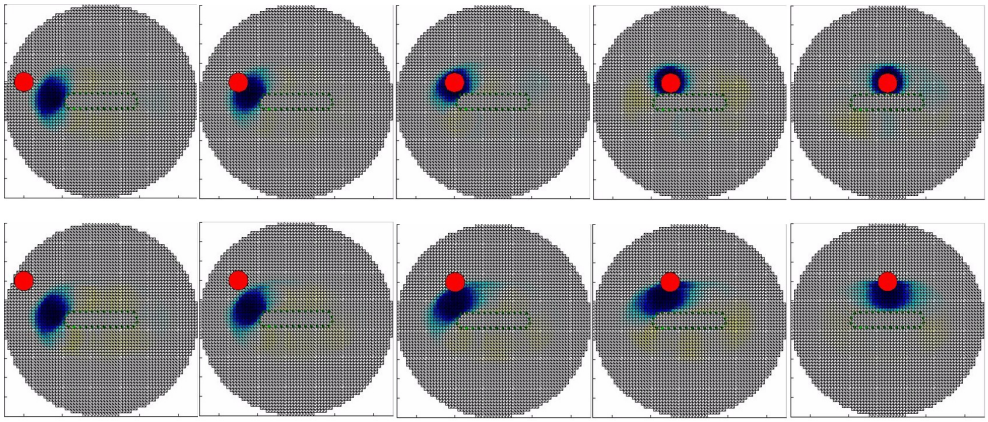

Figure 3.3: *A simple sensor applies the GREIT approach to reconstruct an insulated disk. The red circle indicates the true disk location, and blue color indicates the reconstructed object.*

The reconstructed image is a bitmap where each pixel has a real value rep-

resenting the strength of conductivity. As in Fig. 3.3, the blue color indicates lower conductivity whereas the red represents higher conductivity. As a linear inverse solver, the reconstructed bitmap values are not real conductivity but just the result of the first step of iteration using non-linear solution. However, for sensing purpose, it is the relative strength of conductivity that matters to tell apart objects from the background medium.

The first and second row in Fig. 3.3 show sensing images when the disk has different locations relative to the sensor. For disks near the sensor, the reconstructed images were correctly located and concentrated. Otherwise, the reconstructed images were dispersed and closer to the sensor relative to their real locations. The reconstructed disk position was evaluated by calculating the barycentre of the sensing domain, and the reconstructed artifacts around the sensor were filtered by setting a threshold value for counting pixels.

3.4.2 An Electric-eel

An eel-like sensor was designed to simulate on how the body curvature affects the sensing ability. As the 3-dimensional FEM model of the sensor in Fig. 3.4(a), each section was an insulated cuboid with 3 electrodes attached to the same side, and 10 sections combined the whole sensing body through a linkage joint (overall 30 electrodes). The bending action was simulated by using the same angular between adjacent sections.

The virtual boundary is a cuboid with length 2 m, width 1.5 m, and height 1 m. As in Fig. 3.4, the sensor has 10 cuboid sections (red) with each length 0.06 m, width 0.04 m, and height 0.06 m. The joint (black) length is 0.022 m, and the electrode (green) size is 0.01×0.01 m. The electrodes were specifically meshed using the refinement techniques in [36] while the overall computational burden

was controlled within the ability of a regular desktop. In the forward simulation, the conductive sphere was located at [1, 0.5] m with radius 0.01 m. The forward simulation was conducted using a 3-dimensional FEM model whereas the sensing domain was defined at one side of the sensor and on a 2-dimensional center plane. As in Fig. 3.6 and Fig. 3.7, two types of reconstructing grid were evaluated: the first grid was a projection of the forward model on a plane, and the second was a uniform 64×64 GREIT grid.

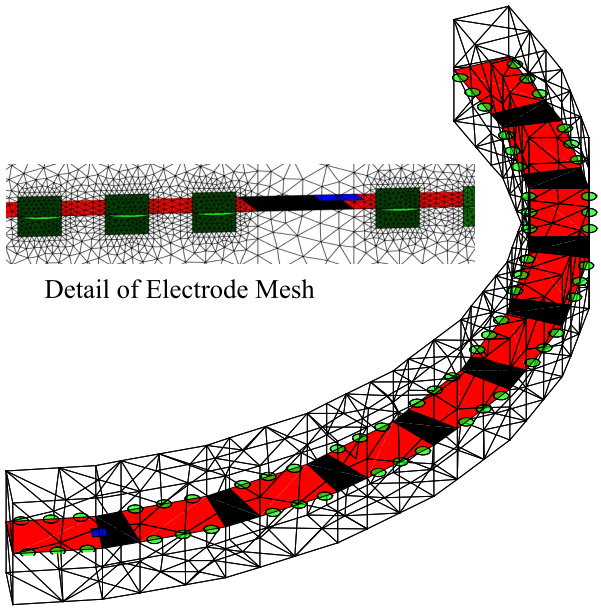

Figure 3.4: *FEM model of an eel-like sensor. A red cuboid represents a section, and a black trapezoid represents a joint whose shape changes with the bending angle between two adjacent sections. The mesh of square electrodes are zoomed in for inspection in detail.*

Fig. 3.5 is the sensibility of the sensing domain when the sensor is straight, and two end electrodes are used for current injection. The bottom of the figure is the boundary of the sensor and electrodes. The color of each grid indicates its sensitivity, which is the change of average perturbation on electrodes when a single unit of conductivity changes as the Jacobian $J(\boldsymbol{\sigma})$ in (3.10). The blue represents the higher sensitive area, and the red represents lower sensitivity as the color bar by the side. According to the sensitivity distribution, the principal sensing

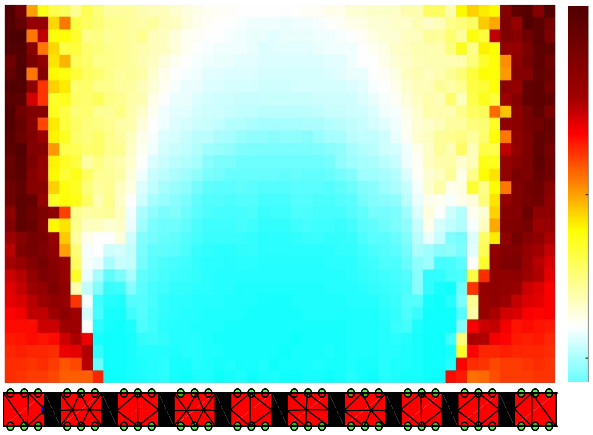

Figure 3.5: *Domain sensibility when the body is straight.*

area is a sector-shaped domain with two narrower and smaller wings beside it. The sensitive range depends on the signal-to-noise rate, which is expressed by the perturbation strength over background noise.

In Fig. 3.6, the sensor curved from 0 to 180 degrees and a sphere (indicated by a sky blue disk in the figure) was fixed in the domain. In each state of curvature, the whole domain was re-meshed. The reconstruction was conducted on the grid projected from the 3-dimensional model in the forward calculation, where a refinement area was defined in front of the sensor. As the reconstruction was conducted in the whole virtual domain, the image intended to disperse to everywhere when the sensor was straight and located far from the object. Initially, the sensor can only identify the direction of the object, but by bending the body to that direction, it can gradually localize the object.

In Fig. 3.7, the GREIT method was used to reconstruct domain with a fixed and uniform grid. In this case, the reconstruction was conducted in fixed meshes, and the only changeable variables were locations of electrodes. The reconstructed area was constrained to a sector-shaped domain in front of the sensor because the far field elements created irrelevant artifacts according to Fig. 3.6. This method reduced the dispersive effect, but when the sensor was straight, the reconstructed

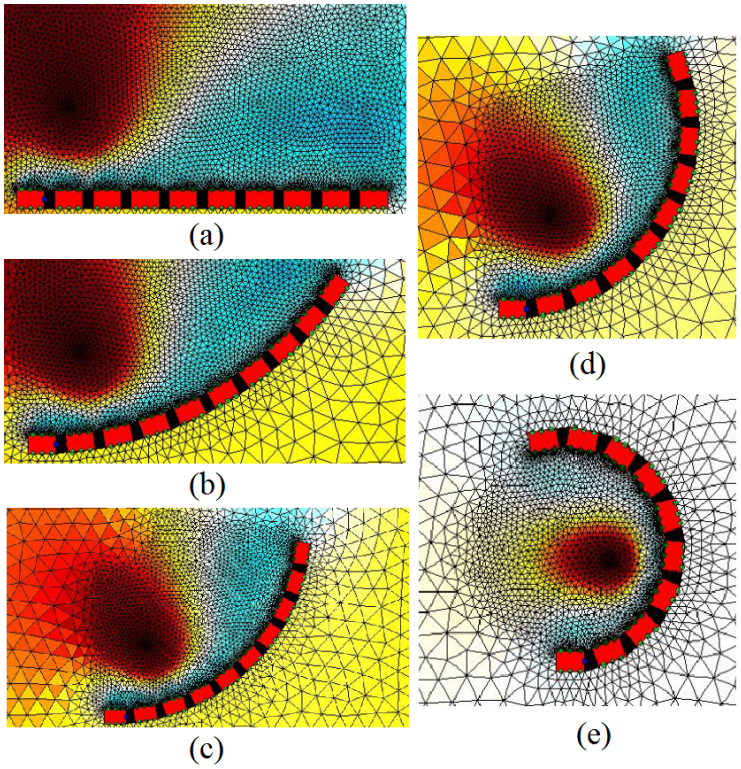

Figure 3.6: *Irregular FEM grids for reconstruction which projected from the 3-dimensional forward model. The true sphere positions are illustrated by sky blue. The whole body curving angles in sub-figures are 10, 80, 110, 170 degrees.*

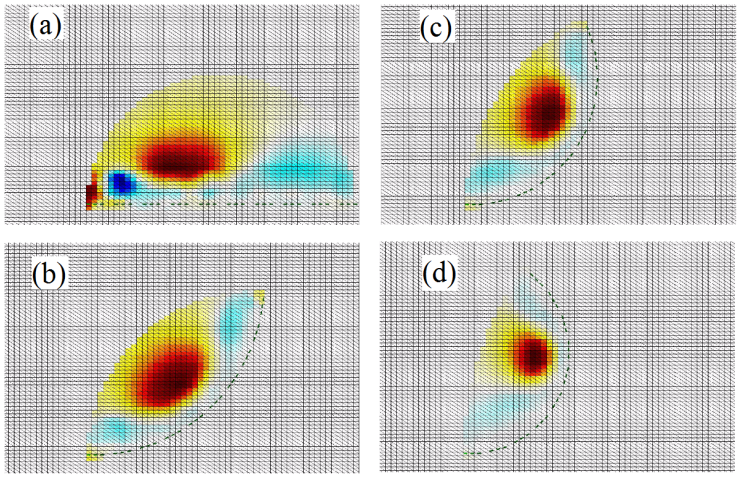

Figure 3.7: *Uniform GREIT grids for reconstruction. The whole body curving angles in sub-figures are 0, 30, 80, 160 degrees.*

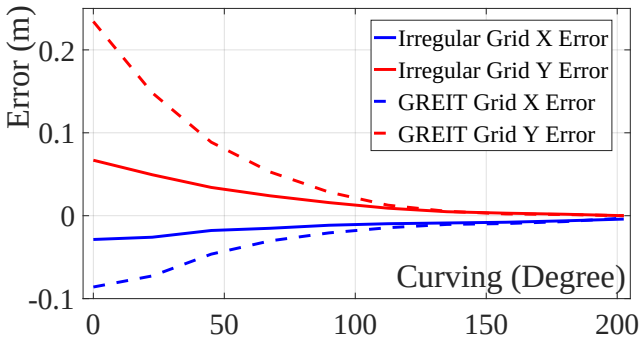

Figure 3.8: *Position errors of reconstructed object using irregular FEM grids and GREIT grids.*

image was still blurred. By curving the sensor, the reconstructed image indicated the more precise location of the object, which was always closer than its real position when the sensor was straight and located far from the object. And at the same time, the blurred effect reduced that the reconstructed image focused to the object.

By comparing results in Fig. 3.6 and Fig. 3.7, the position errors of the reconstructed object were calculated and presented in Fig. 3.8. The calculation combined the centroid method and peak detection, which first filtered irrelevant artifacts and reserved the peaked area then calculated the center of the mass. The filtering process was determined by a parameter θ representing the percentage of image wiped. The result shows a better error performance of the whole domain reconstruction, especially when the curving angle is small. But when the sensor is closer and surrounding the object both methods can accurately sense the target.

The EIT methods to an underwater open-domain electrosensor can roughly detect the direction of the object without curving body and approach to the object. The process of curving and approach is a continuous process that can be integrated into a sensorimotor loop. The whole domain reconstruction can cover a further object but disperse more as well, whereas GREIT reconstruction can constrain the dispersion at the cost of worse localizing errors. In practical

applications, the computational effort should be considered that reconstruction in a larger space is a disadvantage.

3.5 Conclusion

This chapter formulated the underwater electrosense problem using a framework from electrical impedance tomography. A method of decomposing orders of Maxwell's equations was used to deduce the electroquasistatic field. By combing boundaries and electrodes models, finite element method was formulated to solve the forward problem. The open-boundary FEM formulation was an improvement compared to conventional method in a confined area. Inverse problem, or sensing problem, was further formulated using optimization methods. In simulations, two sensors, including a simple cylinder sensor and a bendable eel-like sensor, were designed and evaluated. This work helps us to evaluate the performance of underwater electrosensor using EIT approach.

Chapter 4

A Light Scattering Approach

4.1 Introduction

Rasnow [69] first applied a small sphere perturbation formula (4.1) in a uniform electric field, which can be found in classical electrodynamic literatures [45, 25], to weakly electric fish studies.

$$u(\mathbf{r}) = \mathbf{E}_0 \cdot \mathbf{r}(\frac{a}{r})^3 \frac{(\sigma_1 + j\omega\epsilon_1) - (\sigma_2 + j\omega\epsilon_2)}{(\sigma_1 + j\omega\epsilon_1) + 2(\sigma_2 + j\omega\epsilon_2)}. \tag{4.1}$$

In (4.1), $\mathbf{E}_0$ is the uniform field at the small sphere with radius a, σ_1, ϵ_1 and σ_2, ϵ_2 are electrical properties of ambient medium and the small sphere respectively. Potential perturbation due to the sphere at an observation point $\mathbf{r}$ is $u(\mathbf{r})$. This formula became well-known and was applied in many engineering studies. For sensing in front of a wall or into a tunnel, image method can be applied [45].

The dominant phenomenon in underwater electrosense is the conductive current, but permittivity contrast between objects and background water (displacement current) was proved to be an important factor in identification for weakly electric fish [92]. Thus, the problem is usually simplified to an electroquasistatic

formulation as (4.2), but also take both conductivity and permittivity into consideration [3, 2, 33]. In (4.2), electric field $\mathbf{E}$ is considered in a frequency domain, where σ and ϵ are mass properties distributions, and $\mathbf{J}_s$ is the source current.

$$\nabla(\sigma + j\omega\epsilon)\mathbf{E} = -\nabla \cdot \mathbf{J}_s. \tag{4.2}$$

A scattering formulation for underwater electrosense expanded from theories was mainly developed in light scattering communities. In those problems, [99, 48, 53], an incident electromagnetic field is fired to an object and scattered by it, where theories are established to calculate the resulting field. The incident and scattering model has been extensively used in other sensing techniques such as radar and sonar. When formulating the underwater electrosense into a scattering model, we shoot the current to a sensing region and measure scattering signals like electric potentials or magnetic fields.

Numerical solution of the scattering formulation is based on the discretization of volume integral equations. Such a numerical method was heuristically proposed in [67] before the formal scattering formulation. The basic idea is to replace a continuous object with an ensemble of many small and homogeneous cells (spheres for example), then one can analytically formulate the behavior of the cell under the local homogeneous field. The ensemble effect approaches to the continuous object as the number ofcells going to infinite.

In this chapter, based on a formal formulation of the method of moment (MoM) and discrete dipole approximation (DDA) [99, 48, 53, 52], we proposed rigorous DDA theory of underwater electrosense and corresponding implementation. A sensing application using a simplified underwater robot was presented, and we also made a 1-dimensional sensor in an experiment for validating numerical calculations.

4.2 Scattering Formulation

4.2.1 Problem Statement

Consider the situation as in Fig. 4.1: in a isotropic and homogeneous background medium $\mathcal{O}_b$ with permittivity ϵ_b and conductivity σ_b, several isotropic but not necessarily homogeneous objects (scatterers) $\mathcal{O}_i$ with $\epsilon_i(\mathbf{x})$ and $\sigma_i(\mathbf{x})$, where $i = 1, ..., N$ is the number of objects, are illuminated by an incident electromagnetic field $\mathbf{E}^{inc}(\mathbf{x})$ and $\mathbf{H}^{inc}(\mathbf{x})$ from a source region $\mathcal{O}_s$. The regions of $\mathcal{O}_i$ are bounded but the background medium extends out to infinity. The scattered field $\mathbf{E}^{sca}$ and $\mathbf{H}^{sca}$ need to be determined. The final field is expressed as $\mathbf{E} = \mathbf{E}^{inc} + \mathbf{E}^{sca}$ and $\mathbf{H} = \mathbf{H}^{inc} + \mathbf{H}^{sca}$.

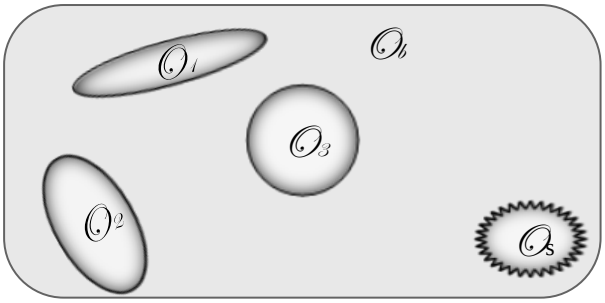

Figure 4.1: *Illustration of the underwater electrosense scattering problem.*

We took the following assumptions in this work. First, assume the magnetic permeability of the whole region to be the same with vacuum permeability μ_0, i.e. $\mathbf{B} = \mu_0\mathbf{H}$ to neglect the magnetic scattering. Second, assume the constitutive relations of the field in isotropic material to be $\mathbf{D} = \epsilon\mathbf{E}$ and conductive current $\mathbf{J_c} = \sigma\mathbf{E}$. Third, assume the incident field is harmonic and with a low frequency that can be represented as $\bar{\mathbf{E}}e^{j\omega t}$, $\bar{\mathbf{H}}e^{j\omega t}$.

4.2.2 Integral Equations

To formulate the scattering form of the underwater electrosense, we first went through with the wave equation to emphasize the electromagnetic scattering nature of such process. Then simplifications and approximations to the specific problem were made accordingly. Also, the significant scattered magnetic field, which is not explicitly given in electroquasistatic formulation (4.2), was determined at the same time.

Consider Maxwell's curl equations [45] using $\mathbf{B} = \mu_0\mathbf{H}$ and $\mathbf{D} = \epsilon\mathbf{E}$ in frequency domain:

$$\nabla \times \mathbf{E} = -j\omega\mu\mathbf{H}, \tag{4.3}$$

$$\nabla \times \mathbf{H} = j\omega\epsilon\mathbf{E} + \mathbf{J}. \tag{4.4}$$

In underwater electrosense, for the space outside the source region (as in Fig. 4.1), $\mathbf{J}$ in (4.4) is the conductive current induced by electric field that $\mathbf{J} = \sigma\mathbf{E}$. Define a complex permittivity to consider the displacement current and conductive current together:

$$\hat{\epsilon} = \epsilon - j\frac{\sigma}{\omega}, \tag{4.5}$$

Then (4.4) can be rewritten as:

$$\nabla \times \mathbf{H} - j\omega\hat{\epsilon}\mathbf{E} = 0. \tag{4.6}$$

For the field in the background medium region $\mathcal{O}_b$:

$$\nabla \times \mathbf{E} + j\omega\mu_0\mathbf{H} = 0, \tag{4.7}$$

$$\nabla \times \mathbf{H} - j\omega\hat{\epsilon}_b\mathbf{E} = 0, \tag{4.8}$$

Similar equations in objects regions $\mathcal{O}_i$ are obtained by replace the the $\hat{\epsilon}_b$ by $\hat{\epsilon}_i$. Combining these equations gets:

$$\nabla \times \mathbf{E} + j\omega\mu_0\mathbf{H} = \mathbf{L}(\mathbf{x}), \tag{4.9}$$

$$\nabla \times \mathbf{H} - j\omega\hat{\epsilon}_b\mathbf{E} = \mathbf{K}(\mathbf{x}), \tag{4.10}$$

For $\mathbf{x} \in \mathcal{O}_b$, magnetic current $\mathbf{L}(\mathbf{x}) = \mathbf{0}$ and electric current $\mathbf{K}(\mathbf{x}) = \mathbf{0}$, and for $\mathbf{x} \in \mathcal{O}_i$, $\mathbf{L}(\mathbf{x}) = \mathbf{0}$ and $\mathbf{K}(\mathbf{x}) = -j\omega(\hat{\epsilon}_b - \hat{\epsilon}_i)\mathbf{E}(\mathbf{x})$.

Using the Gauss's law for magnetic field $\nabla \cdot \mathbf{H} = 0$ and vector identity $\nabla \cdot \nabla \times \mathbf{A} = 0$, define a vector potential $\mathbf{A}$:

$$\mathbf{H} = \nabla \times \mathbf{A}, \tag{4.11}$$

Substitute (4.11) into (4.9) and notice $\mathbf{L}(x) = \mathbf{0}$ everywhere:

$$\nabla \times (\mathbf{E} + j\omega\mu_0\mathbf{A}) = \mathbf{0}, \tag{4.12}$$

Use the vector identity $\nabla \times \nabla u = \mathbf{0}$ to define a scalar potential u:

$$\mathbf{E} + j\omega\mu_0\mathbf{A} = \nabla u. \tag{4.13}$$

Substitute potential definitions (4.13) and (4.11) into (4.10), and apply vector identity $\nabla \times \nabla \times \mathbf{A} = \nabla(\nabla \cdot \mathbf{A}) - \nabla^2\mathbf{A}$:

$$\nabla(\nabla \cdot \mathbf{A}) - \nabla^2\mathbf{A} - k^2\mathbf{A} - j\omega\hat{\epsilon}_b\nabla u = \mathbf{K}, \tag{4.14}$$

where $k^2 = \omega^2\mu_0\hat{\epsilon}_b$. The arbitrary of potential selection allows the specific Lorenz

condition $\nabla \cdot \mathbf{A} = j\omega\hat{\epsilon}_b u$, from which the Helmohltz equations are obtained:

$$(\nabla^2 + k^2)\mathbf{A} = -\mathbf{K}, \tag{4.15}$$

$$(\nabla^2 + k^2)u = \frac{1}{j\omega\hat{\epsilon}_b}\nabla \cdot \mathbf{K}. \tag{4.16}$$

The (4.15) contains three scalar Helmohltz equations. The Green's function or the fundamental solution for solving the scalar Helmohltz equation in 3-dimensional free space is:

$$g(\mathbf{x}, \mathbf{x}') = \frac{e^{-jk|\mathbf{x}-\mathbf{x}'|}}{4\pi|\mathbf{x} - \mathbf{x}'|}, \tag{4.17}$$

The solution of the sourced vector Helmohltz equation is:

$$\mathbf{A}(\mathbf{x}) = \int_{\bigcup \mathcal{O}_i, i=1,\ldots,N} \mathbf{K}(\mathbf{x}')g(\mathbf{x}, \mathbf{x}')d\mathbf{x}', \tag{4.18}$$

And the scalar potential is obtained by Lorenz condition:

$$u = -\frac{1}{j\omega\hat{\epsilon}_b}\int_{\bigcup \mathcal{O}_i, i=1,\ldots,N} \nabla \cdot [\mathbf{K}(\mathbf{x}')g(\mathbf{x}, \mathbf{x}')]d\mathbf{x}'. \tag{4.19}$$

Substituting (4.18) and (4.19) into (4.13) and (4.11) solves the scattered field due to the electric current $\mathbf{K}(\mathbf{x}) = -j\omega(\hat{\epsilon}_b - \hat{\epsilon}_i)\mathbf{E}(\mathbf{x})$ in the object regions $\mathcal{O}_i$ (the union set of object regions is discarded for brevity):

$$\mathbf{E}^{sca}(\mathbf{x}) = -(k^2 + \nabla\nabla\cdot)\int_{\mathcal{O}_i}(1 - \frac{\hat{\epsilon}_i}{\hat{\epsilon}_b})\mathbf{E}(\mathbf{x}')g(\mathbf{x}, \mathbf{x}')d\mathbf{x}', \tag{4.20}$$

$$\mathbf{H}^{sca}(\mathbf{x}) = -\nabla \times \int_{\mathcal{O}_i} j\omega(\hat{\epsilon}_b - \hat{\epsilon}_i)\mathbf{E}(\mathbf{x}')g(\mathbf{x}, \mathbf{x}')d\mathbf{x}'. \tag{4.21}$$

The representation of the electric field in (4.20) has continuous current across

the boundary, i.e. the boundary condition $\epsilon_b \partial \mathbf{E}_b/\partial t + \sigma_b \mathbf{E}_b = \epsilon_i \partial \mathbf{E}_i/\partial t + \sigma_i \mathbf{E}_i$ is satisfied.

The field is scattered from the objects, because only when $\mathbf{x} \in \mathcal{O}_i$ the source item $\mathbf{K}$ of the Helmholtz equation is not zero. In another word, the incident field $\mathbf{E}^{inc}$ is the special solution of the homogeneous Helmholtz equation when $\mathbf{K} = 0$.

Given the field superposition relation $\mathbf{E} = \mathbf{E}^{inc} + \mathbf{E}^{sca}$ and the incident electric field, the scattered electric field or the final electric field are determined by (4.20). The scattered magnetic field is further calculated by (4.21). It is seen that although magnetic permeability of the problem is not considered, the scattered magnetic field is significant due to the strong conductive current.

4.2.3 Further Approximation

After solving the final field, the solution (4.19) can be directly used in underwater electrosense forward problems to predict the potential perturbations and their phase shift at measuring point. Solution (4.21) can also be used if some magnetic field strength measurements are introduced in the problem. These measurements contain the information of geometrical and electrical properties of objects as well.

The solution can be further simplified based on low frequency assumption. When ω approaches zero and then wave number k approaches zero, the approximated Green function $g_0(\mathbf{x}, \mathbf{x}')$ and scatted field $\mathbf{E}_0^{sca}$ can be rewritten:

$$g_0(\mathbf{x}, \mathbf{x}') = \frac{1}{4\pi|\mathbf{x} - \mathbf{x}'|}, \tag{4.22}$$

$$\mathbf{E}_0^{sca}(\mathbf{x}) = -\nabla\nabla \cdot \int_{\mathcal{O}_i} (1 - \frac{\hat{\epsilon}_i}{\hat{\epsilon}_b}) \mathbf{E}(\mathbf{x}') g_0(\mathbf{x}, \mathbf{x}') d\mathbf{x}', \tag{4.23}$$

Further approximation in some cases, only conductive current is considered, i.e.

assume $\epsilon_b = \epsilon_i = \epsilon_0$. The (4.23) can be reduced to:

$$\mathbf{E}_0^{sca}(\mathbf{x}) = -\nabla\nabla \cdot \int_{\mathcal{O}_i} (1 - \frac{\sigma_i}{\sigma_b})\mathbf{E}(\mathbf{x}')g_0(\mathbf{x}, \mathbf{x}')d\mathbf{x}'. \tag{4.24}$$

4.3 Numerical Solutions

The final field formulation $\mathbf{E} = \mathbf{E}^{inc} + \mathbf{E}^{sca}$ belongs to the Fredholm integral equation of the second kind with a singular kernel [9]. To solve the equation numerically, the regions of objects are discretized into non-overlapping subregions. First, using the equation (4.20), the scattering field from one subregion to another is linearly approximated. Second, the scattering influence to a subregion itself is specially evaluated, known as the self-term. This term comes from the singularity nature of the integral formulation using Green's function. Finally, the complete simultaneous algebra equations can be established. MoM is a direct discretization of the equation solving total field, while DDA is developed based on MoM to solve the exciting field.

4.3.1 Method of Moments (MoM)

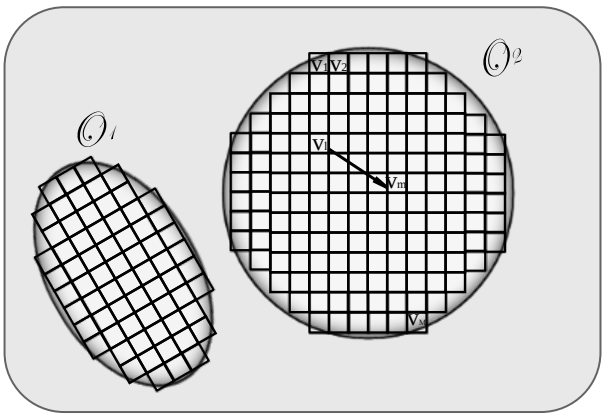

Figure 4.2: *Illustration of the discretization of objects. Arrow from V_l to V_m means the scattered field $\mathbf{E}_{lm}^{sca}$.*

The object region $\mathcal{O}_i$ is divided into M subregions $V_m, m = 1, 2, ..., M$, as Fig. 4.2. Assume each subregion is electrically small (long wavelength approximation) and homogeneous that $\hat{\epsilon}_i(\mathbf{x}) = \hat{\epsilon}(\mathbf{x}_m) = \hat{\epsilon}_m$ for all $\mathbf{x} \in V_m$, where $\mathbf{x}_m$ is a distinguish point inside V_m. Further assume $\mathbf{E}(\mathbf{x}) = \mathbf{E}(\mathbf{x}_m)$ and $\mathbf{H}(\mathbf{x}) = \mathbf{H}(\mathbf{x}_m)$ for all $\mathbf{x} \in V_m$, denoting $\mathbf{E}(\mathbf{x}_m) = \mathbf{E}_m$ and $\mathbf{H}(\mathbf{x}_m) = \mathbf{H}_m$. Denote the subregion volume $v_m = \int\int\int_{V_m} d\mathbf{x}$.

Consider a subregion V_l, in which the electric field is the superposition of the incident field, the scattered field from all other subregions (mutual-term), and scattering influence to itself (self-term).

$$\mathbf{E}_l = \mathbf{E}_l^{inc} + \sum_{m \neq l} \mathbf{E}_{ml}^{sca} + \mathbf{E}_{ll}^{sca}, \tag{4.25}$$

When applying to (4.20) the second term of right hand side is:

$$\sum_{m \neq l} \mathbf{E}_{ml}^{sca} = -\sum_{m \neq l} v_m (1 - \frac{\hat{\epsilon}_m}{\hat{\epsilon}_b})(k^2 + \nabla\nabla\cdot)[\mathbf{E}_m g(\mathbf{x}_l, \mathbf{x}_m)]. \tag{4.26}$$

Applying to all subregions gives rise to M simultaneous vector algebra equations, and such direct discretization of volume integral equation called the method of moment (MoM). The implementation of numerical solutions relies on deciding how to discretize the scatterer and calculate the mutual-term $\mathbf{E}_{ml}^{sca}$ and self-term $\mathbf{E}_{ll}^{sca}$ based on the subregion shape.

Noticing that in (4.20), (4.23), or (4.24), the *gradient divergence* operator $\nabla\nabla\cdot$ is on the $\mathbf{x}$ of integrand. After discretization, each subregion has constant permittivity and conductivity, thus the operator is on $\mathbf{E}_m g(\mathbf{x}_l, \mathbf{x}_m)$, where $\mathbf{E}_m$ is assumed to be a constant vector. Denoting $\mathbf{r} = \mathbf{x} - \mathbf{x}'$, $\hat{\mathbf{r}} = \mathbf{r}/|\mathbf{r}|$, and $r = |\mathbf{r}|$ in

Cartesian coordinate, evaluating with $g_0(\mathbf{r})$ yields:

$$\nabla\nabla\cdot[\mathbf{E}_m g_0(\mathbf{r})] = \frac{1}{4\pi r^3}(3(\mathbf{E}_m\cdot\hat{\mathbf{r}})\hat{\mathbf{r}} - \mathbf{E}_m), \tag{4.27}$$

Denoting $c_m = \mathbf{r}\cdot\mathbf{E}_m$, where $\mathbf{r} = (x_l - x_m, y_l - y_m, z_l - z_m)$ and $\mathbf{E}_m = (E_x^m, E_y^m, E_z^m)$, evaluating with $g(\mathbf{r})$ yields:

$$\begin{aligned}
&(k^2 + \nabla\nabla\cdot)[\mathbf{E}_m g(\mathbf{r})])_x = \\
&\frac{1}{4\pi}\left\{-\frac{jkE_x^m e^{jkr}}{r^2} + \frac{e^{jkr}}{r^3}[k^2 c_m(x_l - x_m) - E_x^m]\right. \\
&\left.+\frac{e^{jkr}}{r^4}ikc_m(x_l - x_m) + \frac{e^{jkr}}{r^5}3c_m(x_l - x_m)\right\} + k^2 E_x^m g(\mathbf{r}), \\
&(k^2 + \nabla\nabla\cdot)[\mathbf{E}_m g(\mathbf{r})])_y = \\
&\frac{1}{4\pi}\left\{-\frac{jkE_y^m e^{jkr}}{r^2} + \frac{e^{jkr}}{r^3}[k^2 c_m(y_l - y_m) - E_y^m]\right. \\
&\left.+\frac{e^{jkr}}{r^4}ikc_m(y_l - y_m) + \frac{e^{jkr}}{r^5}3c_m(y_l - y_m)\right\} + k^2 E_y^m g(\mathbf{r}), \\
&(k^2 + \nabla\nabla\cdot)[\mathbf{E}_m g(\mathbf{r})])_z = \\
&\frac{1}{4\pi}\left\{-\frac{jkE_z^m e^{jkr}}{r^2} + \frac{e^{jkr}}{r^3}[k^2 c_m(z_l - z_m) - E_z^m]\right. \\
&\left.+\frac{e^{jkr}}{r^4}ikc_m(z_l - z_m) + \frac{e^{jkr}}{r^5}3c_m(z_l - z_m)\right\} + k^2 E_z^m g(\mathbf{r}).
\end{aligned} \tag{4.28}$$

In light scattering problems, (4.27) and (4.28) are usually written into a matrix-vector form by introducing the dyadic of Green's function for notation clearness [53]. Denoting a 3×3 dyad $\boldsymbol{R} = \hat{\mathbf{r}}\hat{\mathbf{r}}^T$ (using column vector) and unit dyad $\boldsymbol{I} = diag(3,3)$, operators (dyadic Green's function) can be defined and evaluated as:

$$\boldsymbol{G_0}(\mathbf{r}) := \nabla\nabla\cdot[g_0(\mathbf{r})] = -\frac{1}{4\pi r^3}(\boldsymbol{I} - 3\boldsymbol{R}), \tag{4.29}$$

$$\begin{aligned}\boldsymbol{G}(\mathbf{r}) := (k^2 + \nabla\nabla\cdot)[g(\mathbf{r})]) = \\ [k^2(\boldsymbol{I} - \boldsymbol{R}) + (\frac{jkr-1}{r^2})(\boldsymbol{I} - 3\boldsymbol{R})]g(\mathbf{r}),\end{aligned} \tag{4.30}$$

Then (4.27) and (4.28) can be compactly represented as $\boldsymbol{G_0}(\mathbf{r})\mathbf{E}_m$ and $\boldsymbol{G}(\mathbf{r})\mathbf{E}_m$.

4.3.2 The Self-Term

The integrand contains a singularity point at $|\mathbf{x} - \mathbf{x}'| = 0$, which raises the difficulty of integration. When discretizing the formulation, the problem is how to evaluate the self-term $\mathbf{E}_{ll}^{sca}$.

This problem was first solved for $k = 0$ case by Kellogg [50] with a rigorous treatment using potential theory, and further solved for $k \neq 0$ by Fikioris [32] with a similar procedure. Wang [94] offered a consistent view on tackling singularities applying either distribution theory or classical potential theory.

We following the treatment in [53], for a electrically small subregion V_m enclosed by surface S_m, self-term can be calculated as:

$$\mathbf{E}_{mm}^{sca} = (1 - \frac{\hat{\epsilon}_m}{\hat{\epsilon}_b})(\boldsymbol{M} - \boldsymbol{L})\mathbf{E}_m, \tag{4.31}$$

Dyadic operators $\boldsymbol{M}$ and $\boldsymbol{L}$ are:

$$\begin{aligned}\boldsymbol{M} &= \int_{V_m} [\boldsymbol{G}(\mathbf{x} - \mathbf{x_0}) - \boldsymbol{G_0}(\mathbf{x} - \mathbf{x_0})]d\mathbf{x}, \\ \boldsymbol{L} &= \int_{S_m} \frac{\mathbf{n}(\mathbf{x} - \mathbf{x_0})^T}{4\pi|\mathbf{x} - \mathbf{x}_0|^3} d\mathbf{x}.\end{aligned} \tag{4.32}$$

Where $\mathbf{n}$ is the unit normal to the surface and $\mathbf{x}_0$ is a distinguished point inside V_m. Both $\boldsymbol{M}$ and $\boldsymbol{L}$ can be calculated numerically for arbitrary shapes or analytically for regular shapes. As low frequency approximation and the size of V_m going to zero, $\boldsymbol{M}$ approaches to zero. However $\boldsymbol{L}$ only depends on the shape

of V_m. For example, for a regular cubical or spherical subregion with $\mathbf{x}_0$ at the centre, $\boldsymbol{L} = \frac{1}{3}\boldsymbol{I}$ can be obtained [52].

4.3.3 Discrete Dipole Approximation (DDA)

MoM calculates the total field $\mathbf{E}$, while another method named discrete dipole approximation (DDA) offers a different approach. In DDA, the unknown field that need to be solved is formulated as exciting field $\mathbf{E}^{exc}$. The exciting field of a subregion is defined to be the sum of incident field and scattering field from all other subregions; from (4.25) following is defined:

$$\mathbf{E}_l^{exc} := \mathbf{E}_l^{inc} + \sum_{m \neq l} \mathbf{E}_{ml}^{sca} = \mathbf{E}_l - \mathbf{E}_{ll}^{sca}, \tag{4.33}$$

Using (4.31) and (4.33) and setting $\boldsymbol{M} = 0$ and $\boldsymbol{L} = \frac{1}{3}\boldsymbol{I}$ we get:

$$\mathbf{E}_l = [\boldsymbol{I} + (1 - \frac{\hat{\epsilon}_l}{\hat{\epsilon}_b})\boldsymbol{L}]^{-1}\mathbf{E}_l^{exc} = \frac{3\hat{\epsilon}_b}{2\hat{\epsilon}_b + \hat{\epsilon}_l}\mathbf{E}_l^{exc}, \tag{4.34}$$

Then the scattering field from a subregion to another $\mathbf{E}_{ml}^{sca}$ in (4.26) can be re-expressed due to the exciting field $\mathbf{E}_m^{exc}$:

$$\mathbf{E}_{ml}^{sca} = 3v_m \frac{\hat{\epsilon}_m - \hat{\epsilon}_b}{\hat{\epsilon}_m + 2\hat{\epsilon}_b}(k^2 + \nabla\nabla\cdot)[\mathbf{E}_m^{exc} g(\mathbf{x}_l, \mathbf{x}_m)], \tag{4.35}$$

Or in a dyadic Green's function form:

$$\mathbf{E}_{ml}^{sca} = 3v_m \frac{\hat{\epsilon}_m - \hat{\epsilon}_b}{\hat{\epsilon}_m + 2\hat{\epsilon}_b}\boldsymbol{G}(\mathbf{x}_m, \mathbf{x}_l)\mathbf{E}_m^{exc}, \tag{4.36}$$

Substituting (4.36) back to (4.33), the exciting field of DDA formulation can be solved by M simultaneous vector algebra equations.

The reason of naming discrete dipole approximation is because of a local

current density:

$$\mathbf{K}_l = -j\omega(\hat{\epsilon}_b - \hat{\epsilon}_l)\mathbf{E}_l = 3j\omega\hat{\epsilon}_b \frac{\hat{\epsilon}_l - \hat{\epsilon}_b}{\hat{\epsilon}_l + 2\hat{\epsilon}_b}\mathbf{E}_l^{exc}, \tag{4.37}$$

This local current density in subregion with size v_l gives a dipole moment $\mathbf{p}_l$. For example, assume a spherical subregion with radius a:

$$\mathbf{p}_l = \frac{j}{\omega} v_l \mathbf{K}_l = -4\pi a^3 \hat{\epsilon}_b \frac{\hat{\epsilon}_l - \hat{\epsilon}_b}{\hat{\epsilon}_l + 2\hat{\epsilon}_b}\mathbf{E}_l^{exc}. \tag{4.38}$$

Remarks: First, (4.37) relates the macro current to micro-local current that can be taken as a generalized Clausius–Mossotti relation. Second, the assumption of spherical subregion shape in (4.38) gives a well-known result (4.1) in underwater electrosense problems, which is the perturbation of a small sphere in uniform electric field.

4.3.4 Implementation Issues

Numerical stability

Theoretically, both MoM (4.25) and DDA formulation (4.33) can be applied, but in practice of underwater electrosense, DDA is always chosen because of the numerical instability of MoM. The scattering coefficient in (4.26) is $1 - \frac{\hat{\epsilon}_i}{\hat{\epsilon}_b}$, and in complex permittivity $\hat{\epsilon} = \epsilon - j\frac{\sigma}{\omega}$ the conductivity can be zero (insulator) or infinite large (perfect conductor), while the permittivity is a finite number. Thus the range of scattering coefficient is $(-\infty, 0)$ that gives a large conditional number of algebra equations, leading to numerical instability. In another view, MoM solves the total field, but for a conductor, the inside total electric field is nearly zero.

DDA formulation solves the exciting field. The scattering coefficient $\frac{\hat{\epsilon}_l - \hat{\epsilon}_b}{\hat{\epsilon}_l + 2\hat{\epsilon}_b}$

in (4.36) is constrained in $(-\frac{1}{2}, 1)$ when the conductivity ranges from zero to infinite. There are several approximated equations that can be used. The strictest equation should be (4.20), while in underwater electrosense field frequency ranges from $1-100\ kHz$ and using approximation equation (4.23) is accepted. And DDA method using (4.36) and (4.33) should choose corresponding Green's functions.

Discretization Errors

In DDA method of underwater electrosense, the item $\boldsymbol{M}$ in (4.31) can always be neglected due to two reasons: the low frequency enables $\boldsymbol{G}$ approaches to $\boldsymbol{G}_0$; the subregion volume approaches to zero. As for discretization, regular subregion shapes, either spherical or cubical, have same $\boldsymbol{L}$ and scattering equation (4.36). The different volume effect decreases when it approaches zero. However, the object boundary can not be exactly matched by discretized subregions. This error decrease as well when granularity approaches to infinite. In practice, the region near the object boundary can enjoy a better granularity to suppress this shape error.

4.4 Implementation and Validation

We adopt the open source FEM solver [2] with complete electrode model (CEM) to compare the numerical results with DDA. Because the perturbation is relatively small, it is required to refine the FEM meshes to convergence to get standard and accurate results. As suggested in [35] that a serious full dimensional FEM model should contain a million elements with special refinement on electrodes.

4.4.1 DDA Implementation

To make the formulation explicit, we use (4.36) and (4.29) to build algebra equations. In this situation, only conductivity is considered. Assume objects are approximated by a cluster of N identical spheres, which are located at positions of $S_i = (x_i, y_i, z_i), i = 1...N$, and α is the sphere radius, and k is the scattering coefficient $\frac{\hat{\sigma}_l - \hat{\sigma}_b}{\hat{\sigma}_l + 2\hat{\sigma}_b}$.

Set $\mathbf{d}_{ji} = \left(d_{ji}^x, d_{ji}^y, d_{ji}^z\right)$ to be the distance vector from j to i, and normalized vector is $\hat{\mathbf{d}}_{ji} = \left(\hat{d}_{ji}^x, \hat{d}_{ji}^y, \hat{d}_{ji}^z\right)$. According to (4.33), the equilibrium of N-spheres cluster can be expressed as:

$$\begin{bmatrix} \mathbf{I}_3 & -\mathbf{A}_{12} & .. & -\mathbf{A}_{1N} \\ -\mathbf{A}_{21} & \mathbf{I}_3 & .. & -\mathbf{A}_{2N} \\ : & : & . & : \\ -\mathbf{A}_{N1} & -\mathbf{A}_{N2} & .. & \mathbf{I}_3 \end{bmatrix} \begin{bmatrix} \mathbf{E}_1^{exc} \\ \mathbf{E}_2^{exc} \\ : \\ \mathbf{E}_N^{exc} \end{bmatrix} = \begin{bmatrix} \mathbf{E}_1^{inc} \\ \mathbf{E}_2^{inc} \\ : \\ \mathbf{E}_N^{inc} \end{bmatrix}, \tag{4.39}$$

$$\mathbf{A}_{ji} = \frac{a^3 k}{|\mathbf{d}_{ji}|^3} \begin{bmatrix} 3\hat{d}_{ji}^x \hat{d}_{ji}^x - 1 & 3\hat{d}_{ji}^x \hat{d}_{ji}^y & 3\hat{d}_{ji}^x \hat{d}_{ji}^z \\ 3\hat{d}_{ji}^y \hat{d}_{ji}^x & 3\hat{d}_{ji}^y \hat{d}_{ji}^y - 1 & 3\hat{d}_{ji}^y \hat{d}_{ji}^z \\ 3\hat{d}_{ji}^z \hat{d}_{ji}^x & 3\hat{d}_{ji}^z \hat{d}_{ji}^y & 3\hat{d}_{ji}^z \hat{d}_{ji}^z - 1 \end{bmatrix}. \tag{4.40}$$

This is a $\mathrm{A}\mathbf{x} = \mathbf{b}$ form a linear system with a dense and symmetric coefficient matrix, which can be directly solved for small values of N and iteratively solved to for large N.

4.4.2 Numerical Setup

In this implementation, two parallel-plate electrodes are used to create an incident uniform electric field in a tank between them, see Fig. 4.3. Additional 25 electrodes are placed in different positions to measure corresponding potentials,

and they are created to be small compared to the exciting electrodes and object to the minimum their influence. All the electrode impedance is set to be insignificant. In this FEM model, the ground node the as zero potential references is defined to be the center node of one edge of the tank.

Two cases of axis-aligned objects are studied. The size of the uniform tank is set to be 1 $m \times 1\ m \times 1\ m$, and the cuboid is 0.2 $m \times 0.2\ m \times 0.2\ m$, while dimensions of the ellipsoid are 0.4 $m \times 0.3\ m \times 0.2\ m$. The background medium conductivity is 1, and the object conductivity is 10. There is a 0.1 A current flowing from the right emitting electrode to the left. Probes array are organized in a 0.5 $m \times 0.5\ m$ planar square and 0.1 m from the left emitting electrode, whose actual size is set to be 1 mm.

The conventional measuring method is adopted that difference of potentials between the probes are taken, and the first probe to be the common reference. The perturbation is defined to be the signal with invading objects subtracting the signal without objects in FEM, which is the same situation of real measurement. In DDA model the perturbation is calculated directly through (4.13), and the incident uniform electric field is calculated using (4.41), where S is the emitting electrode area.

$$E_x = \frac{I}{\sigma_m S}, E_y = 0, E_z = 0. \tag{4.41}$$

To compare the signals from FEM and DDA, Average relative error (RE) and overall root mean square error (RMSE) are calculated according to (4.42) and (4.43). In $p(i,j)$ is the signal of $i-th$ probe at $j-th$ position, and n and m is the probes number and positions number.

$$RE = \frac{1}{m}\sqrt{\sum_{j=1}^{m}(\sum_{i=1}^{n}\left(p_F(i,j) - p_D(i,j)\right)^2 / \sum_{i=1}^{n} p_F(i,j)^2)}, \tag{4.42}$$

$$RMSE = \sqrt{(\sum_{j=1}^{m}\sum_{i=1}^{n}(p_F(i,j) - p_D(i,j))^2)/mn}. \tag{4.43}$$

4.4.3 Case of Cuboid and Ellipsoid

Numerical results using FEM model and DDA model (Fig. 4.3) are compared in Fig. 4.4, Fig. 4.5 and Fig. 4.6. In DDA model, 172 spheres constitute the cuboid and 294 spheres constitute the ellipsoid. In FEM models the perturbation signals come from the object appearance signals subtracting non-object signals, while in DDA approach the perturbations are directly calculated using (4.1) after solving the linear system (4.33).

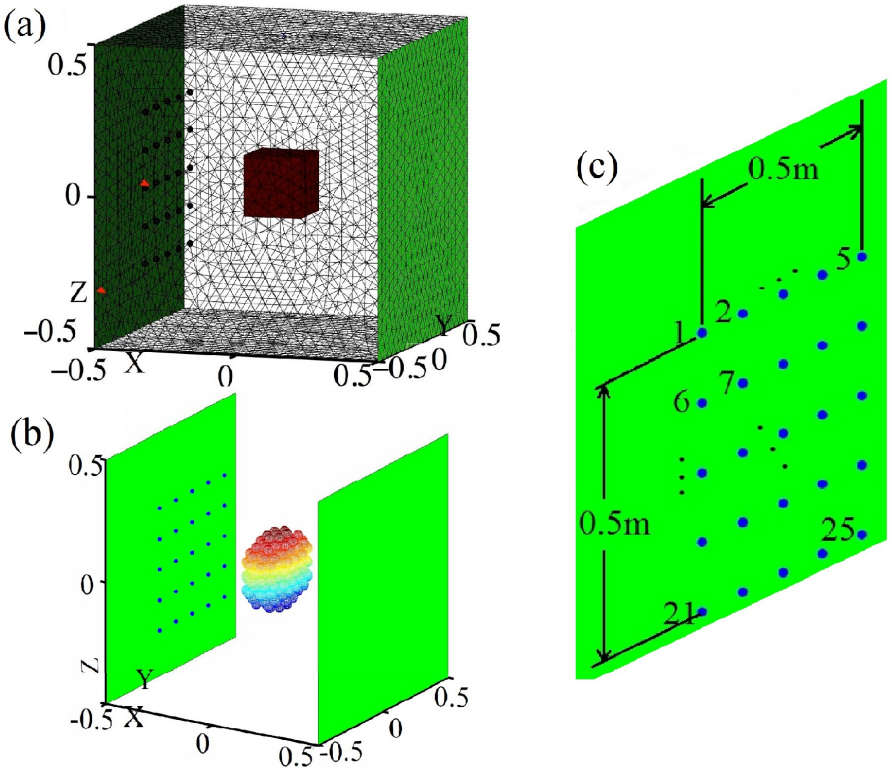

Figure 4.3: *FEM model (left) and DDA model (right) of ellipsoid and cube in parallel-plate electrodes.*

To validate the object perturbations at different positions and sizes, they are first moved along the $x-$axis and then $y-$axis from $-0.2\ m$ to $0.2\ m$, and then

the cuboidal side length varied from 0.03 m to 0.3 m at the tank centre. Overall RSME for cuboid is 9.64×10^{-4} in Fig. 4.4 and 9.73×10^{-4} in Fig. 4.5, and average RE is 7.10% in Fig. 4.4 and 10.46% in Fig. 4.5. Overall RSME for ellipsoid is 1.10×10^{-3} in Fig. 4.4 and 9.16×10^{-4} in Fig. 4.5, and average RE is 9.62% in Fig. 4.4 and 13.05% in Fig. 4.5.

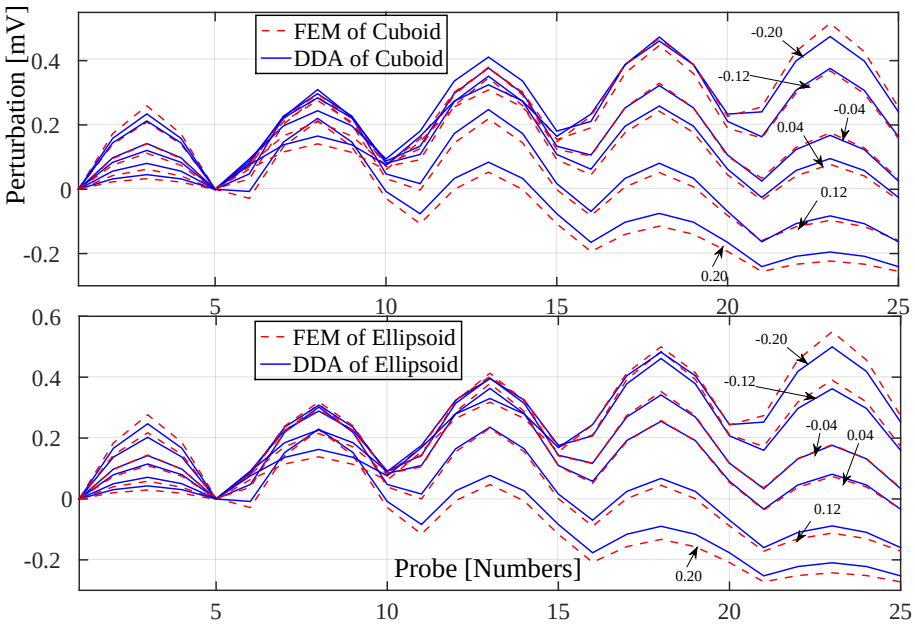

Figure 4.4: *Cuboid and ellipsoid perturbation moving along $y-$axis at evenly distributed positions from -0.2 m to 0.2 m at a step of 0.08 m resp. in FEM and DDA models. Signals are mutiplied by 100 in figures.*

As seen in Fig. 4.6 that perturbations of the varying cuboid using DDA model are well consistent with FEM model in a tenfold range, with overall RSME 1.50×10^{-3} and average RE 11.82%. It is also noticed that when the object is relatively small, for example, the first graph of Fig. 4.6 with the object size less than 5% of the problem scale, FEM results is not as stable as DDA because of the numerical round-off errors.

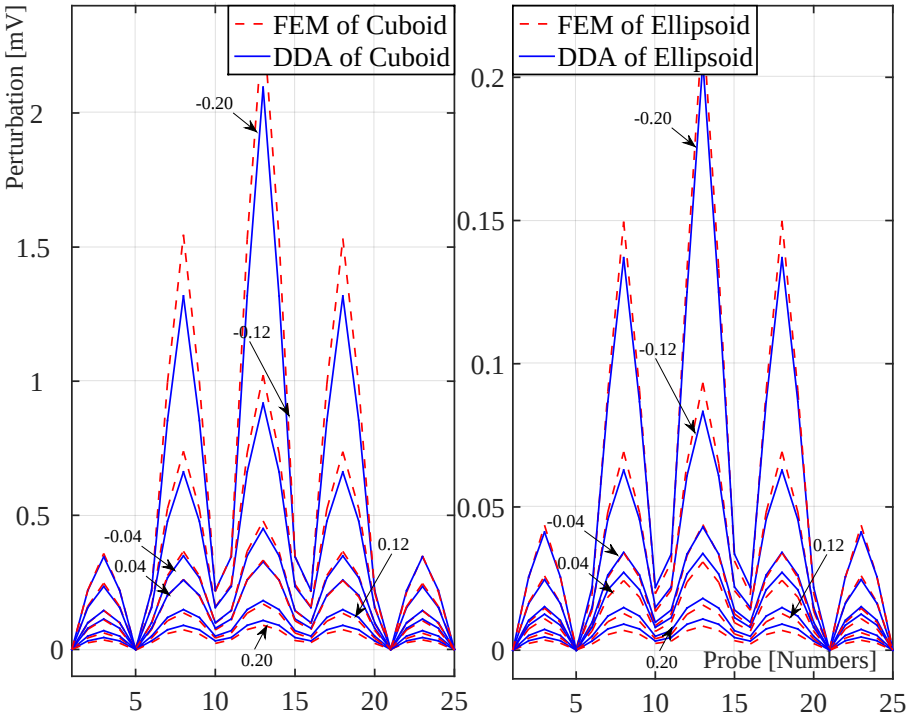

Figure 4.5: *Cuboid and ellipsoid perturbation moving along $x-$axis at evenly distributed positions from -0.2 m to 0.2 m at a step of 0.08 m resp. in FEM and DDA models. Signals are mutiplied by 100 in figures.*

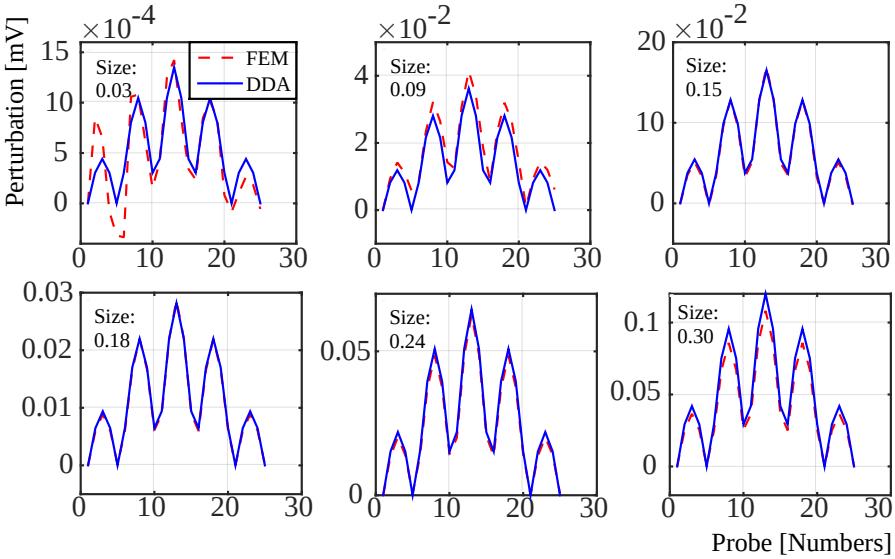

Figure 4.6: *Cuboid perturbation by varying its size. From left to right and up to down, figures represent evenly distributed side length resp. from 0.03 m to 0.3 m at a step of 0.06 m. Signals are mutiplied by 100 in figures.*

4.4.4 Comparison and Discussion

Table 4.1 gives typical facts of computing time of our implementation. Programs ran on a common desktop with Intel i5 CPU 3.4GHz and Matlab 2014. Numerical simulation shows high consistency between DDA and FEM models (around 10% relative difference), while DDA approach cost less than 1% computational effort than FEM method.

Table 4.1: *Comparison on computing time of implementation*

		Cuboid	Ellipsoid
FEM (EIDORS Solver)	Element Quantity	399316	406732
	Computing Time (s)	21.64	22.68
DDA (Matlab Division Solver)	Sphere Quantity	172	294
	Computing Time (s)	0.16	0.19
	Time Fraction of FEM	0.74%	0.84%
Average Relative Difference		9.79%	11.34%

The discrepancy comes from following reasons. First, in the DDA model, we applied a uniform incident field, whereas in FEM model the incident field cannot be perfectly uniform. The field created by parallel-plate electrodes will be slightly distorted by the object inside it. The reason of distortion is due to the re-distribution of charges on the plates. This problem will be eased if we use point electrodes in electrosensor design. The numerical instability appears when the object is small in FEM model, as displayed in the first figure of Fig. 4.6. Second, in addition to discretization error, we noticed that peak signals have larger differences, which can come from the shape approximation that sharp edges of cuboid and ellipsoid are blurred by spheres [99].

DDA approach is flexible in representing objects and more computationally

efficient than the universal approaches such as FEM for underwater electrosense. DDA has several advantages than FEM in underwater electrosense. First, the scattering formulation only discretizes the object regions, while in FEM the whole domain needs to be discretized, which is overkill. Second, FEM theoretically can only deal with the close-region problem without the specifically designed infinite-far element. Third, in active sensing, it is proper to define a controlled transmitting energy, such as the modulated radar or sonar transmitting waves. Defining an incident electric field avoids tackling complex boundary conditions of the source region, which should be controlled and modulated.

The computational complexity of directly solving linear system (4.39) by LU decomposition is $O(n^3)$, where $n = 3N$, N is the number of constituting spheres. If the size and shape of object do not vary, the decomposition $\mathbf{A} = \mathbf{LU}$ is fixed and only the incident field $\mathbf{b}$ changes. In such case, the computational complexity by forward and back substitution is $O(n^2)$. For dynamic applications where objects move continuously, the iterative method that generally converges in $m \ll n$ steps can also be applied, and each iterative computation time is $O(n^2)$. Our implementation of a 1688 dipoles system typically shows a convergence to 10^{-9} order at around 50 steps using Biconjugate Gradient (BG) or Quasi-Minimal Residual(QMR) methods. Further, by taking the advantage of the regular structure of the dipole cluster, techniques like FFT (Fast Fourier Transform) can be utilized to accelerate the matrix-vector multiplication in iterative methods to $O(n \log n)$, which has proved to be effective in light scattering problems [99]. The hierarchy techniques like FMM (Fast Multipole Method) [34] are also promising to make the matrix-vector multiplication in such specific problems faster.

4.5 Application

4.5.1 General Inverse Problem

In forward problem, the sensing domain is discretized into M pieces of parameters vector $\mathbf{m}$. Data $\mathbf{d}$ are observed at several points of amount N. The DDA solver use parameters $\mathbf{m}$ to establish system matrix $\boldsymbol{A}_{M\times M}$, which maps the excited field to the incident field. Observation matrix $\boldsymbol{B}_{N\times M}$ maps the excited field to the data $\mathbf{d}$.

$$\boldsymbol{A}(\mathbf{m})\mathbf{E}^{exc} = \mathbf{E}^{inc}, \tag{4.44}$$

$$\boldsymbol{B}(\mathbf{m})\mathbf{E}^{exc} = \mathbf{d}, \tag{4.45}$$

According to (4.36) and (4.33):

$$\boldsymbol{A}(\mathbf{m}) = \boldsymbol{H}_A diag(\mathbf{m}) + \boldsymbol{I}, \tag{4.46}$$

$$\boldsymbol{B}(\mathbf{m}) = \boldsymbol{H}_B diag(\mathbf{m}), \tag{4.47}$$

$$\boldsymbol{H}_A = \begin{bmatrix} \mathbf{0}_3 & -\boldsymbol{G}_{12} & .. & -\boldsymbol{G}_{1M} \\ -\boldsymbol{G}_{21} & \mathbf{0}_3 & .. & -\boldsymbol{G}_{2M} \\ : & : & . & : \\ -\boldsymbol{G}_{M1} & -\boldsymbol{G}_{M2} & .. & \mathbf{0}_3 \end{bmatrix}, \tag{4.48}$$

$$\boldsymbol{H}_B = \begin{bmatrix} \boldsymbol{G}_{1d_1} & \boldsymbol{G}_{1d_2} & .. & \boldsymbol{G}_{1d_N} \\ \boldsymbol{G}_{2d_1} & \boldsymbol{G}_{2d_2} & .. & \boldsymbol{G}_{2d_N} \\ : & : & . & : \\ \boldsymbol{G}_{M1} & \boldsymbol{G}_{M2} & .. & \boldsymbol{G}_{Md_N} \end{bmatrix}, \tag{4.49}$$

Where items of parameters vector $\mathbf{m}$ are $m_i = 3v_i\frac{\hat{\epsilon}_i - \hat{\epsilon}_b}{\hat{\epsilon}_i + 2\hat{\epsilon}_b}$, items of $\boldsymbol{H}_A$ and $\boldsymbol{H}_B$ are dyadic Green's functions defined by (4.29) or (4.30).

The forward problem is to calculate $\mathbf{d}$, given $\boldsymbol{H}_A$, $\boldsymbol{H}_B$, $\mathbf{m}$ and $\mathbf{E}^{inc}$. This is well-posed as $\boldsymbol{A}$ is invertible, so $\mathbf{d} = \boldsymbol{B}(\mathbf{m})\boldsymbol{A}^{-1}(\mathbf{m})\mathbf{E}^{inc}$.

The inverse problem is to find an optimal $\mathbf{m}^*$, given $\boldsymbol{H}_A$, $\boldsymbol{H}_B$, $\mathbf{d}$ and $\mathbf{E}^{inc}$, to minimize the cost function for a given metric μ in Hilbert space:

$$\Phi(\mathbf{m}^*) = \left\| \boldsymbol{B}(\mathbf{m}^*)\boldsymbol{A}^{-1}(\mathbf{m}^*)\mathbf{E}^{inc} - \mathbf{d} \right\|_\mu . \tag{4.50}$$

This is a nonlinear, high-dimensionality optimization problem. Many techniques, such as the method of steepest descent, conjugate gradient method and Newton method, can be applied [100]. The inverse problem of EIT is based on a similar formulation in (4.50). To enable optimization techniques, a Frechet derivative matrix of $\mathbf{f}(\mathbf{m})$ needs to be calculated, which is called sensitive or Jacobian matrix in EIT [2].

One of the difficulties of inverse problem is the solution instability that partially comes from the huge parameter space (high dimensionality). Regularization is able to introduce constrains to parameters, or in a probabilistic view it introduces a priori to the problem. For example, Tikhonov regularization technique introduces a priori model $\mathbf{m}_{apr}$ and a hyperparameter α [2, 100] to the cost function:

$$\Phi(\mathbf{m}^*) = \left\| \mathbf{f}(\mathbf{m}^*) - \mathbf{d} \right\|_\mu + \alpha \left\| \mathbf{m}^* - \mathbf{m}_{apr} \right\|_\mu , \tag{4.51}$$

Where $\mathbf{f}(\mathbf{m}^*) = \boldsymbol{B}(\mathbf{m}^*)\boldsymbol{A}^{-1}(\mathbf{m}^*)\mathbf{E}^{inc}$. Intuitively the priori model limits the solution not far from it in some metric sense, and the hyperparameter indicates how strong the constraint is.

4.5.2 A Simplified Robot with Electrosense

The underwater electrosense is an inverse problem: given the incident field and the observations at some finite points of the final field, we need to infer the information about scatterers properties. A simplified underwater robot equipped with electrosense was extensively designed to test the DDA approach on detecting invading objects within robot's sensing range and estimating their features. Two spherical conductors acted as current emitting electrodes, as Fig. 4.7(a), and along the center line of emitting electrodes was a group of evenly distributed probing electrodes for potential measurements.

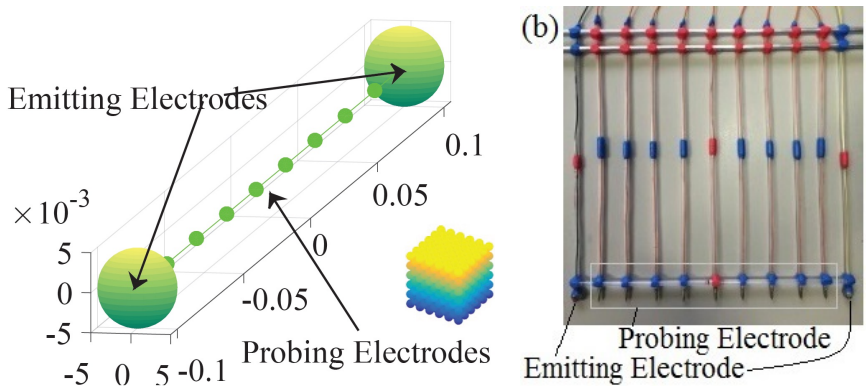

Figure 4.7: *(a) The simplified robot model with electrosense for sensing a cube. (b) A 1-dimensional sensor. Frame was made by very slender plastical pipes, and electrodes used stainless steal. The handmade sensor had 11 electrodes locating at [-8.6 -7.1 -5.5 -3.6 -1.7 0 2.0 3.8 5.7 7.4 8.8] cm along the axis.*

The incident electric field can be determined and controlled by injecting current from emitting point electrodes. Assume the emitting electrode to be a perfect conductor, i.e. electric field is zero inside, taking a Gaussian volume encircling the electrode surface and excluding the feeding wire: as $Q = \epsilon_m \int_s \mathbf{E} ds = \epsilon_m \int_s \frac{\mathbf{J}}{\sigma_m} ds$, thus we have $Q = \frac{I\epsilon_m}{\sigma_m}$. It means whole net charges on the emitting electrode is determined if the overall current is given. This can be used to calculate the incident electric field at any point in the sensing space. When the emitting elec-

trodes are designed small or the distance from the object is large, the field can be calculated as:

$$\mathbf{E} = \frac{Q}{4\pi\varepsilon_m}\frac{\mathbf{r}}{r^3} = \frac{I}{4\pi\sigma_m}\frac{\mathbf{r}}{r^3}. \tag{4.52}$$

If the object is very close to the emitting electrode, making the size of electrode significant, the equation (4.52) may be inaccurate. In a microscopical view, although the whole charge always stays the same, the new distribution of charges will change the near field. From this point of view, a smaller emitting electrode is better.

Fig. 4.8 shows the perturbation signals between adjacent probing electrodes amplified by 100 in DDA model and FEM model, and the probes number is 30, and the emitting current is 0.1 A using the simplified configuration. The robot is under the fly-by from -0.1 m to 0.1 m of a conductive cube from one emitting electrode to the other, axis-aligned and 0.05 m far from the robot center axis. Cube size is 0.04 $m \times 0.04$ $m \times 0.04$ m and its conductivity is 10.

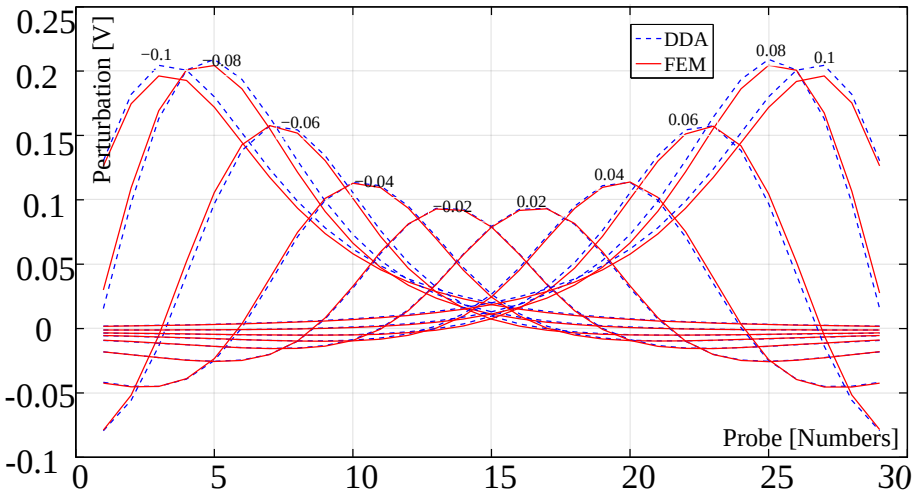

Figure 4.8: *Perturbation signals comparison under a cube fly-by from* -0.1 m *to* 0.1 m *in robotic electrosense configuration*

4.5.3 Experiment

We further made a 1-dimensional sensor, as in Fig. 4.7(b), according to the design of the simplified robot to validate the results from DDA approach. Emitting electrodes are two balls of diameter 4 mm and 9 smaller nail-like probing electrodes are arranged in the line between them. All electrodes used stainless steel to reduce electrochemical corrosion. The sensor frame was made by slender plastic pipes.

For current injection and signal acquisition, we used commercially available CompactRIO plus modules of voltage meter (NI 9265) and current source (NI 9205) from National Instruments. These modules are fully configurable in Labview and can be seamlessly interfaced to Matlab through build-in script node. The output range of current source is ± 20 mA with a maximum load of 600 Ω. When operating at the finest scale ± 200 mV of the potential meter, the absolute accuracy is 150 μV, and the sensitivity is 4 μV.

To reject noise and reduce chemical reaction between electrodes and water, the current was modulated into a square wave at 1kHz. Receiving signals on probing electrodes were synchronously demodulated into in-phase and quadrature components. Before the demodulation, a high-pass filter was utilized to remove the underwater DC field, and the synchronous demodulation itself acted as a super narrow band pass filter that rejects all AC noise.

The sensor was held in a tank with salty waters (salt added tap water), as Fig. 4.9(a), and the conductivity of the water was not determined. As a calibration process, by injecting 20 mA current through emitting electrodes, we first measured the potentials of probing electrodes when no objects exist. Then simulations with same sensor model and injecting current were conducted with different conductivity. We could find the best match of probe potentials between

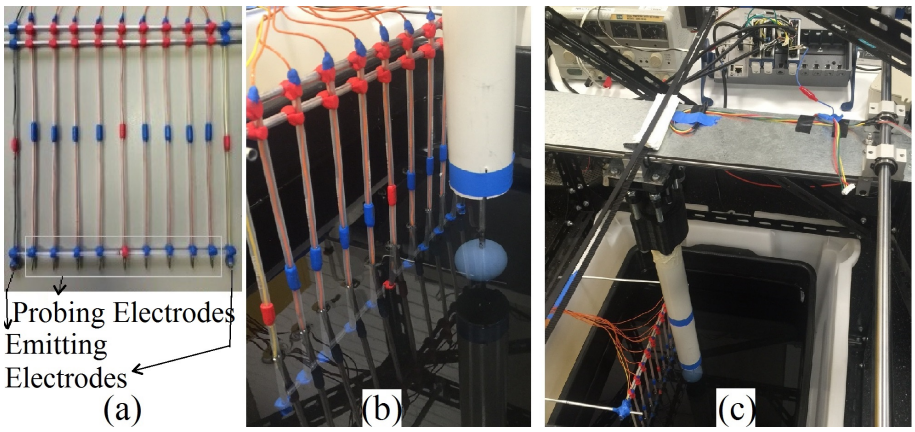

Figure 4.9: *(a) Sensor tested in a tank with salty water. (b) Testing platform overview. Electrodes were connected to the NI instruments.*

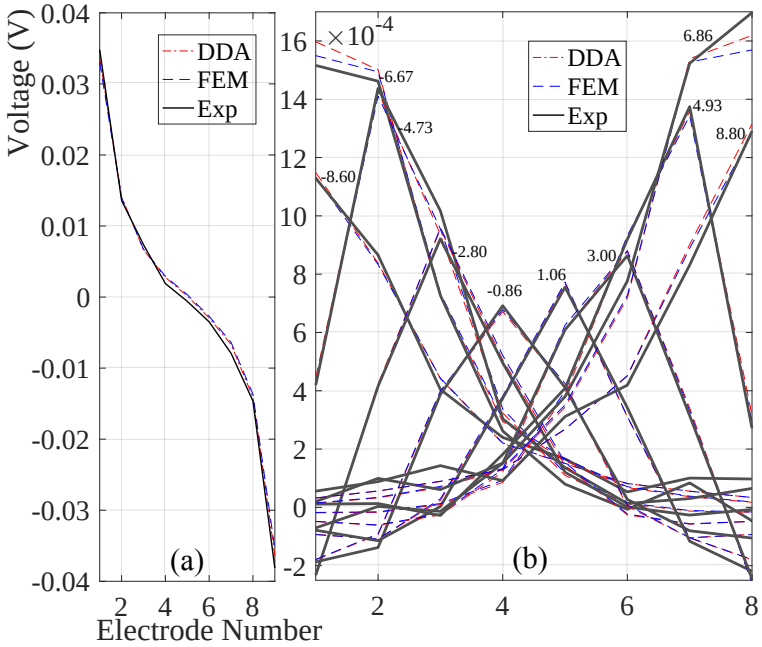

Figure 4.10: *(a) Potential matched between DDA, FEM and experimental data through parameter adjustment. (b) Potential perturbations comparison under specific potentials matching.*

experiment and simulation in the least square sense. Because the incident electric field is uniquely determined by the potential field, the match of potentials leads to the match of the perturbation signals which can be calculated by DDA approach.

Due to the tank effect, the signal was stronger than the simulation. Insulated tank walls can be modeled as mirrors of the source. For example, if the tank is 1 meter-wide and the sensor is 10 centimeter-long centered in the tank, two tank walls increase the perturbation by approximately 2% for the object is at a body-length away. This effect was partially compensated by the calibration. When the object was closing the emitting electrode, the discrepancy between experimental signal and simulation increased, because we used a relatively large emitting electrode to reduce surface current density (less electrochemical corrosion), which was actually not a point electrode in the near field.

In this experiment, the simulating conductivity that found was 0.285 s/m, and the corresponding potential match is shown in Fig. 4.10(a). An insulating sphere (diameter 4.2 cm) was moved from one emitting electrode to the other along the parallel line of the sensor at distance of 5 cm, as in Fig. 4.9(b), and corresponding perturbation comparison between experiment, DDA and FEM were shown in Fig. 4.10(b). From the experiment, we confirmed the effectiveness of numerical calculations.

4.6 Conclusion

We provided a scattering formulation, which was expanded from light scattering theories, for underwater electrosense. Corresponding numerical solutions including MoM and DDA were formulated and implemented, and we explained that only DDA method was suitable. Compared to other formulations, scattering model

has several advantages in active sensing problems by controlling the transmitting signals. These works laid a solid foundation for developing more sophisticated underwater electrosensors.

This chapter provides a novel approach targets on reducing the computational burden of the forward problem by introducing the method of discrete dipole approximation (DDA). It is found to perform more than 100 times faster than FEM in previous chapter with only a 10% relative difference in underwater electrosense problems. Based on the fast DDA solution of the forward problem, two types of sensing algorithms to tackle the inverse problem in following chapters, unscented Kalman filters (UKF) and neural networks (NN), can be designed to localize and identify an object.

Chapter 5

Sensor Design and Sensing Algorithms

5.1 Introduction

The idea of electrical impedance tomography is the whole domain reconstruction. This approach comes across with many problems like environment representation, unaffordable computational burden, and the large-dimension problem of the inverse problem. In this chapter, we tackle an easier problem using a stronger constraint: given a single object in the water, how to use the electrosensor to infer its shape, size, and location.

We formulate the shape identification as a classification problem, in which many specified shapes are potential options, and after a procedure, the closest one shall be recognized. After shape identification, the object can be parameterized by its boundary dimensions, orientations, and locations.

We introduced 1-D and 2-D sensor design using I-U mode. A known current was injected through small electrodes and deduced potentials were measured by an array of electrodes. DDA approach can be applied to I-U mode sensors.

First, given the parameterized object and DDA solution of the forward problem, unscented Kalman filter was used to estimate its size and location using both 1-D and 2-D sensor. Second, a simple back-propagation neural network was proved to be useful to directly map the measurements to the state space after proper training.

Enlarging the number of electrodes of the 2-D sensor made the conception of electrical image meaningful, and statistic learning method like convolutional neural network (CNN), which is widely used in digital image recognition, could be applied for object identification.

5.2 Sensor Design

5.2.1 1-D and 2-D Sensor

The simplest way of building an electrosensor is all electrodes aligned in a line, which is a 1-D sensor widely used in previous studies. As in Fig. 5.1, N probing electrodes are all set between two emitting electrodes, which means to measure the inner field perturbations (electrical voltages). This design was tested and validated in the previous chapter.

We can also design the underwater electrosensor morphology in an intuitive way, which was a membrane emulating the electric fish skin. As an analogy between 'retina vision' and 'electroreceptor vision', the electric organ acts like a lightning source that illumines the near-range space. Just like the projection on the retina, the electrical image on the fish skin can be interpreted as a transform from a 3-dimensional space to a 2-dimensional surface, but with a complex projecting law.

The sensor consists of emitting electrodes to establish the electric field and

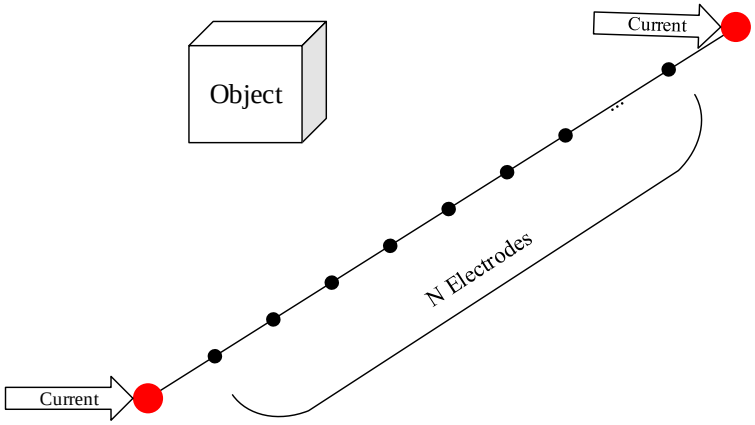

Figure 5.1: *Sensor design with coordinate frame. Black dots are probing electrodes measuring potentials and red dots are emitting electrodes conducting currents.*

probing electrodes to sense the perturbations. I-U mode is adopted, where a controlled current is injected into the water by point emitting electrodes, and corresponding measurements are potentials taken from probing electrodes. The I-U mode enables the application of fast DDA method in the forward problem. It also offers a higher sensibility compared to U-I or U-U mode.

Probes are arranged into a two-dimensional array on the surface, where corresponding potentials build up an electrical image. Emitters are set into pairs that each pair conducts a channel of controlled current. As Fig. 5.2, the $N \times N$ dot matrix represents the probing electrodes, and M pairs of opposite dots represent emitting electrodes (current channels). In practical application, the sensor can be two-side that probes and emitters are exposed to both sides of the water, and also can be one-side that electrodes are only set on a single side of the surface.

5.2.2 DDA Approach

Applying DDA approach to the forward problem, a known incident electric field is presupposed. Objects are discretized into small particles (dipoles) and the final field is calculated from the interaction between dipoles and the incident field.

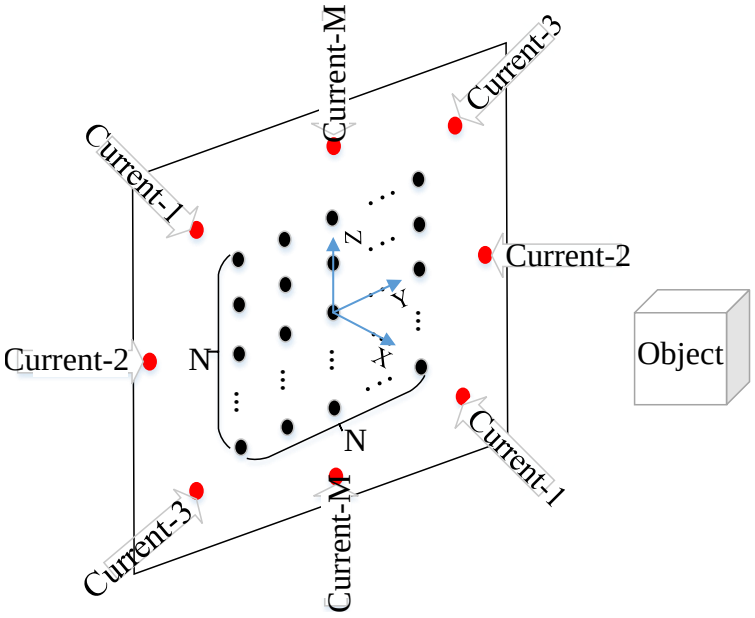

Figure 5.2: *Sensor design with coordinate frame. Black dots are probing electrodes measuring potentials and red dots are emitting electrodes conducting currents.*

The incident electric field can be determined and controlled by injecting current from emitting point electrodes. Assume the emitting electrode to be a perfect conductor, i.e. electric field is zero inside, taking a Gaussian volume encircling the electrode surface and excluding the feeding wire: as $Q = \epsilon_m \int_s \mathbf{E} ds = \epsilon_m \int_s \frac{\mathbf{J}}{\sigma_m} ds$, thus we have $Q = \frac{I\epsilon_m}{\sigma_m}$. It means whole net charges on the emitting electrode is determined if the overall current is given. This can be used to calculate the incident electric field at any point in the sensing space. When the emitting electrodes are designed small or the distance from the object is large, the field can be calculated as:

$$\mathbf{E} = \frac{Q}{4\pi\varepsilon_m}\frac{\mathbf{r}}{r^3} = \frac{I}{4\pi\sigma_m}\frac{\mathbf{r}}{r^3}. \tag{5.1}$$

If the object is very close to the emitting electrode, making the size of electrode significant, the equation (5.1) may be inaccurate. In a microscopical view, although the whole charge always stays the same, the new distribution of charges will change the near field. From this point of view, the smaller emitting electrode

is better.

The calculated signals using DDA approach are potential perturbations $\delta\mathbf{U}$ of objects, while direct measurements are potentials $\mathbf{U}_s$, therefore we need to establish a base signal $\mathbf{U}_b$ when no objects present that $\delta\mathbf{U} = \mathbf{U}_s - \mathbf{U}_b$. As a reference electrode (potential zero) is needed in voltage measurement, a $N \times N$ probing matrix will generate $N^2 - 1$ measurements.

5.2.3 Sensibility

By injecting controlled current, the system can self-adjust the output power. In other words, the output power is proportional to the resistance of the environment. This feature increases the sensibility compared to the U-I mode [72]. For example, in the situation of the sensor facing to an insulating wall (a large object), as Fig. 5.3(a), for the central probing electrode its base signal is determined by two real emitting electrodes, while its perturbation signal is determined by two imagery emitting electrodes with same charges.

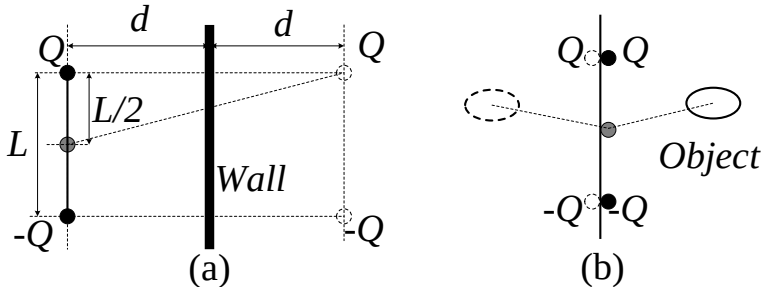

Figure 5.3: *(a) Schematic diagram for sensibility calculation. (b) Sensing model for one-side design.*

The relative signal perturbation is:

$$\frac{\delta\mathbf{U}}{\mathbf{U}_s} = \frac{L/2}{L/2 + \sqrt{(L/2)^2 + (2d)^2}} \tag{5.2}$$

where L is the largest length of the sensor and d is the distance to the wall.

Defining $d = L$ we get $\frac{\delta \mathbf{U}}{\mathbf{U}_s} = \frac{1}{1+\sqrt{17}} \approx 19.5\%$. This reletive perturbation is much larger than U-I mode in [72], where to achieve a body-length sensing to a wall the sensitivity need to be 0.2%.

To further increase the SNR, one-sided design can be used due to the image principle, as Fig. 5.3(b). First, the field strength is doubled compared to the two-side case using (5.1) with the same amount of current. Second, perturbations from objects are doubled as well. As a result, its signal is four times of two-side sensor or pure-electrode sensor as tested in [81].

5.3 Unscented Kalman Filter for Localization

Kalman filters are step-by-step signal matching approaches to state estimation problems that can tackle measurement or system evolution uncertainties. If the shape of an object is identified, it can be parameterized by its position and dimensions. These parameters compose the state space of the Kalman filter. The unscented Kalman filter is chosen because it needs no analytical relationship between the state and the observation [74]. Thus we can use numerical methods for observation prediction.

State space representation (5.3) includes a system evolution model and an observation model, where $\mathbf{x}$ is the system state representing the geometry parameters; f is the relative moving pattern of the sensor; $\mathbf{u}$ is the input; h is the mapping from state $\mathbf{x}$ to observation $\mathbf{y}$; $\mathbf{v}$ and $\mathbf{n}$ are the system noises with white Gaussian of covariance $Q = E[\mathbf{v}_k \mathbf{v}_k^{\mathrm{T}}]$ and $R = E[\mathbf{n}_k \mathbf{n}_k^{\mathrm{T}}]$.

$$\begin{aligned} \mathbf{x}_k &= f\left(\mathbf{x}_{k-1}, \mathbf{u}_{k-1}\right) + \mathbf{v}_{k-1}, \ \mathbf{v}_k \sim (0, Q_k) \\ \mathbf{y}_k &= h\left(\mathbf{x}_k\right) + \mathbf{n}_k, \ \mathbf{n}_k \sim (0, R_k) \end{aligned} \tag{5.3}$$

A constrained unscented Kalman filter (CUKF) was designed. $\hat{\mathbf{x}}_0$ and $\mathbf{P}_0$ are

initial state and covariance that can be obtained from coarse estimation of neural network; χ_k is called sigma points that spread from state and covariance, and they are used for time updating and calculating Kalman gain $\mathbf{K}_k$.

Initialize:

$$\begin{aligned} \hat{\mathbf{x}}_0 &= E[\mathbf{x}_0] \\ \mathbf{P}_0 &= E[(\mathbf{x}_0 - \hat{\mathbf{x}}_0)(\mathbf{x}_0 - \hat{\mathbf{x}}_0)^T] \end{aligned} \tag{5.4}$$

Calculate the sigma points: $\chi_{k-1} = [\hat{\mathbf{x}}_{k-1} \quad \hat{\mathbf{x}}_{k-1} \pm \sqrt{(M+\lambda)\mathbf{P}_{k-1}}]$

Time update:

$$\begin{aligned} \chi^-{}_{k|k-1} &= f\left(\chi_{k-1}, \mathbf{u}_{k-1}\right) \\ \hat{\mathbf{x}}_k^- &= \sum_{i=0}^{2M} W_i^{(m)} \chi_{i,k|k-1}^- \\ \mathbf{P}_k^- &= \sum_{i=0}^{2M} W_i^{(c)} [\chi_{i,k|k-1}^- - \hat{\mathbf{x}}_k^-][\chi_{i,k|k-1}^- - \hat{\mathbf{x}}_k^-]^T \end{aligned} \tag{5.5}$$

Calculate the sigma points and measurement prediction:

$$\begin{aligned} \chi_{k-1} &= [\hat{\mathbf{x}}_{k-1} \quad \hat{\mathbf{x}}_{k-1} \pm \sqrt{(M+\lambda)\mathbf{P}_{k-1}}] \\ \mathbf{Y}_{k|k-1} &= h(\chi^-{}_k) \\ \hat{\mathbf{y}}_k^- &= \sum_{i=0}^{2M} W_i^{(m)} \mathbf{y}_{i,k|k-1}^- \end{aligned} \tag{5.6}$$

Calculate the Kalman Gain:

$$\begin{aligned} \mathbf{P}_{yy} &= \sum_{i=0}^{2M} W_i^{(c)} [\mathbf{Y}_{i,k|k-1}^- - \hat{\mathbf{y}}_k^-][\mathbf{Y}_{i,k|k-1}^- - \hat{\mathbf{y}}_k^-]^T \\ \mathbf{P}_{xy} &= \sum_{i=0}^{2M} W_i^{(c)} [\chi_{i,k|k-1}^- - \hat{\mathbf{x}}_k^-][\mathbf{Y}_{i,k|k-1}^- - \hat{\mathbf{y}}_k^-]^T \\ \mathbf{K}_k &= \mathbf{P}_{xy}(\mathbf{P}_{yy})^{-1} \end{aligned} \tag{5.7}$$

Observation update:

$$\begin{aligned}
\mathbf{r}_k &= \tilde{\mathbf{y}}_k - \hat{\mathbf{y}}_k^- \\
\hat{\mathbf{x}}_k &= \hat{\mathbf{x}}_k^- + \mathbf{K}_k \mathbf{r}_k \\
\mathbf{P}_k &= \mathbf{P}^-{}_k - \mathbf{K}_k \mathbf{P}_{yy} \mathbf{K}^T{}_k
\end{aligned} \tag{5.8}$$

If:

$$\mathbf{D}\hat{\mathbf{x}}_k < \mathbf{d} \tag{5.9}$$

Only consider active row:

$$\mathbf{D}_{act}\hat{\mathbf{x}}_{k,act} = \mathbf{d}_{act} \tag{5.10}$$

Solution to the linear equality constrain problem:

$$\begin{aligned}
&\mathbf{K}'{}_k = \mathbf{K}_k - \mathbf{D}^T{}_{act}(\mathbf{D}_{act}\mathbf{D}^T{}_{act})^{-1} \\
&(\mathbf{D}_{act}\hat{\mathbf{x}}_{k,act} - \mathbf{d}_{act})(\mathbf{r}^T{}_k \mathbf{P}^{-1}{}_{yy}\mathbf{r}_k)^{-1}\mathbf{r}^T{}_k \mathbf{P}^{-1}{}_{yy}
\end{aligned} \tag{5.11}$$

Fixed measurement update:

$$\begin{aligned}
\hat{\mathbf{x}}_k^{'} &= \hat{\mathbf{x}}_k^- + \mathbf{K}'{}_k \mathbf{r}_k \\
\mathbf{P}'{}_k &= \mathbf{P}^-{}_k - \mathbf{K}'{}_k \mathbf{P}_{yy} \mathbf{K}'^T{}_k
\end{aligned} \tag{5.12}$$

One of the practical problems applying unscented Kalman filter is that the state may exceed the reasonable range, for example, the distance to the object or the object size may be less than zero or exceed the largest range in the problem. In such case, state constraints should be considered. We fixed the Kalman Gain using Active Set Method or Gain Projection [75].

Algorithm step 7 is the state constraints check, where $\mathbf{D}\hat{\mathbf{x}}_k = \mathbf{d}$ is the expression of critical state. When such a critical state is broken, rows of active states

(broken states) $\mathbf{D}_{act}\hat{\mathbf{x}}_{k,act} = \mathbf{d}_{act}$ will be used to fix the Kalman gain $\mathbf{K}'_k$. Parameters in the algorithm are chosen according to formulas in (5.13) and can also refer to paper [47].

$$\begin{aligned}
&\lambda = \alpha^2(M+\kappa) - M \\
&W_0^{(m)} = \lambda/(M+\lambda) \\
&W_0^{(c)} = \lambda/(M+\lambda) + (1-\alpha^2+\beta) \\
&W_i^{(m)} = W_i^{(c)} = \lambda/\{2(M+\lambda)\}, i = 1, ..., 2M
\end{aligned} \tag{5.13}$$

5.3.1 Simulations with CUKF

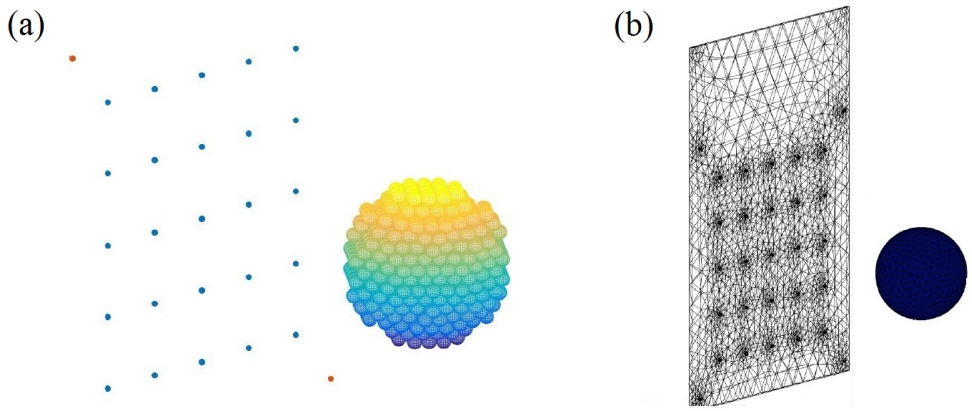

Figure 5.4: *(a) DDA model of a 5-by-5 planar sensor with a sphere. (b) FEM model of a 5-by-5 planar sensor with a sphere.*

As the first example, Fig. 5.5(a) illustrates an example of simulating CUKF to estimate positions of an insulating sphere given its radius using a 2-D planar sensor. The measurements were generated from FEM model, while DDA model was used as the forward model in CUKF, as seen in Fig. 5.4. It can be seen that the constraints cause the states to be truncated at 0.03 m on $x-$axis and -0.06 m on $y-$axis. Because of the discrepancy between the DDA and FEM results, the estimated positions have steady-state errors of 0.13 cm and 0.08 cm on x and y. Fig. 5.5(b) gives more details on how CUKF estimates the state step-by-step

to approach an optimal signal matching. This inverse inferring process further demonstrates the consistency between FEM and DDA models.

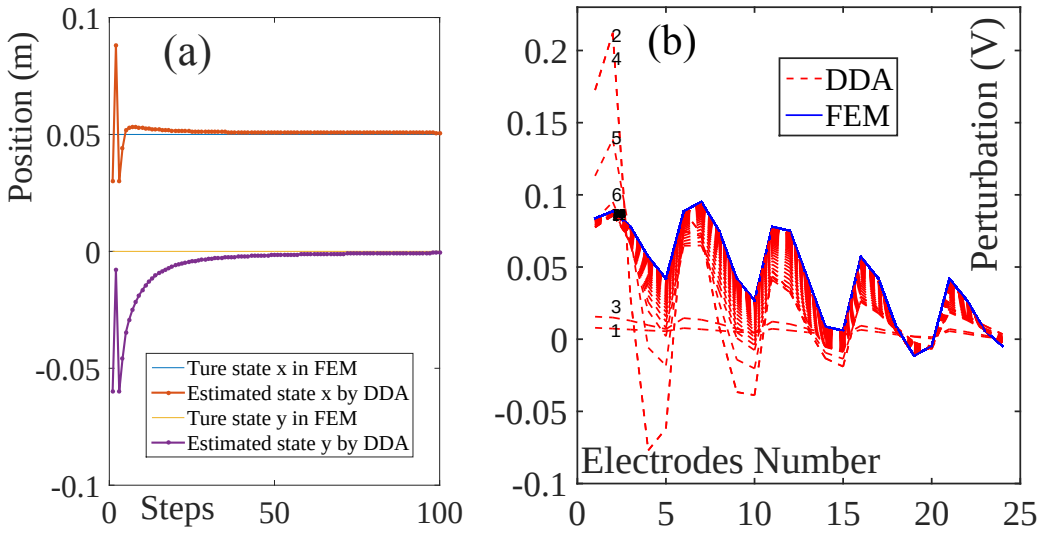

Figure 5.5: *(a) CUKF on position estimation. $x-$axis is the distance to the sensor, and $y-$axis is the direction parallel to sensor plane. (b) Details of step-by-step signal matching using CUKF. Real line is the perturbation signal generated by FEM model, while dashed line is signal generated by DDA model of each estimating step. Step numbers of initial several steps are labelled. Simulation used injected current 2 mA and insulated sphere radius 0.0275 m and signal amplified by 100.*

As the second example, the axis-aligned 1-D robot was at the origin, and a cube with side length 0.04 m was fixed at $(x, y, z) = (0.05, 0.05, 0)$. Solution by UKF was a static optimization problem to minimize the signal difference between the measurements and model predictions. Initializing the state at a random point within the sensing range, the localization and identification process is illustrated in Fig. 5.6(a). The measurement signals were mixed with zero mean Gaussian noise of SNR = 30. In the second simulation, a cube with side length 0.03 m was moved from $(-0.05, 0.05, 0)$ to $(0.05, 0.05, 0)$ with a fixed velocity. This motion was corrupted with 2% noise, and the measurement signals were mixed with zero mean Gaussian noise of SNR = 30. The tracking and identification process by

CUKF is illustrated in Fig. 5.6(b).

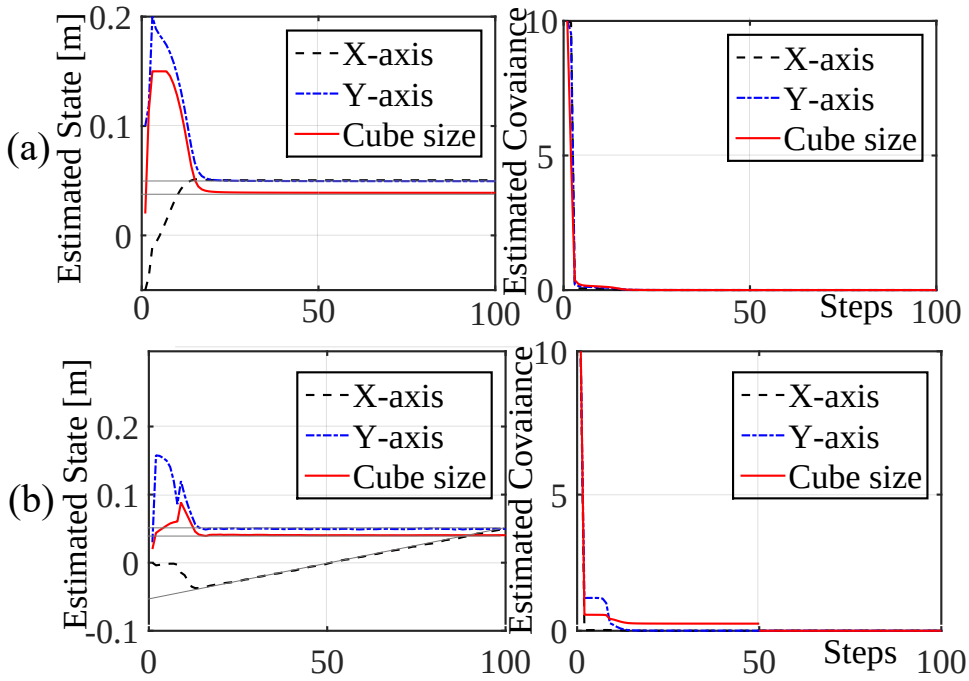

Figure 5.6: *(a) CUKF searches for a static cube and estimate its size by a simplified robot model with electrosense. (b) CUKF tracks the fly-by and estimate the size of a cube by a simplified robot model with electrosense.*

Simulation of both cases estimates the correct states with convergence in about 20 steps, demonstrating the effectiveness of UKF with constraints in underwater active electrosense problems. This further validates the consistency of DDA and FEM approach on the forward problem calculations.

5.4 Back-Propagation Neural Network for Localization

Given the shape of the object, a traditional BPNN can be used for regressing its position and size. A small probing matrix (5×5 pixels, 6×6 cm) was used to infer the position and size of a sphere. Training spheres were randomly sampled and simulated using DDA for 2000 times (within the predefined sensing area: $x \in$

[3,12] cm, $y \in$ [-6,6] cm, $z \in$ [-6,6] cm and sphere diameter $d \in$ [1,6] cm).

Fig. 5.7 illustrates the sensing ability using a four-layer BPNN ([20 16 12 8]) with 25 inputs and 4 outputs. Each electrode generates a potential through the DDA simulation, and 25 electrodes form the whole input space. Whereas three positions and the size of the sphere form the out output space.

The second coordinate axis attached to figure is the one used by the sensor in Fig. 5.2. Figures in the left column are error distributions of x, y, r using simulating signals without noise (y and z are symmetric with same features). Error distributions are almost uniform within the whole sensing area, with average error 0.3835, 0.4077, and 0.2973 cm of x, y and r respectively.

Figures in the right column are error distributions using inputs with 1% white Gaussian noise, with average error 0.9853, 1.2933, and 0.3461 cm of x, y and r respectively. It can be seen that the localizing performance is not uniform, where far-field sensing is more easily affected by the noise because signals decrease quickly with the increasing range. However, the size mapping r is more immunized from noise, even in the far field.

5.5 Convolutional Neural Network for Identification

5.5.1 Electrical Images

Electrical images composed of perturbation signals can be generated by DDA simulation. Assuming a uniform electric field normal to the plane, images in Fig. 5.8 were generated using a large probing matrix (100×100 pixels). A spherical object has simplest electrical images because its full symmetry makes it independent from the orientation. Using the coordinate frame in Fig. 5.2, Fig.

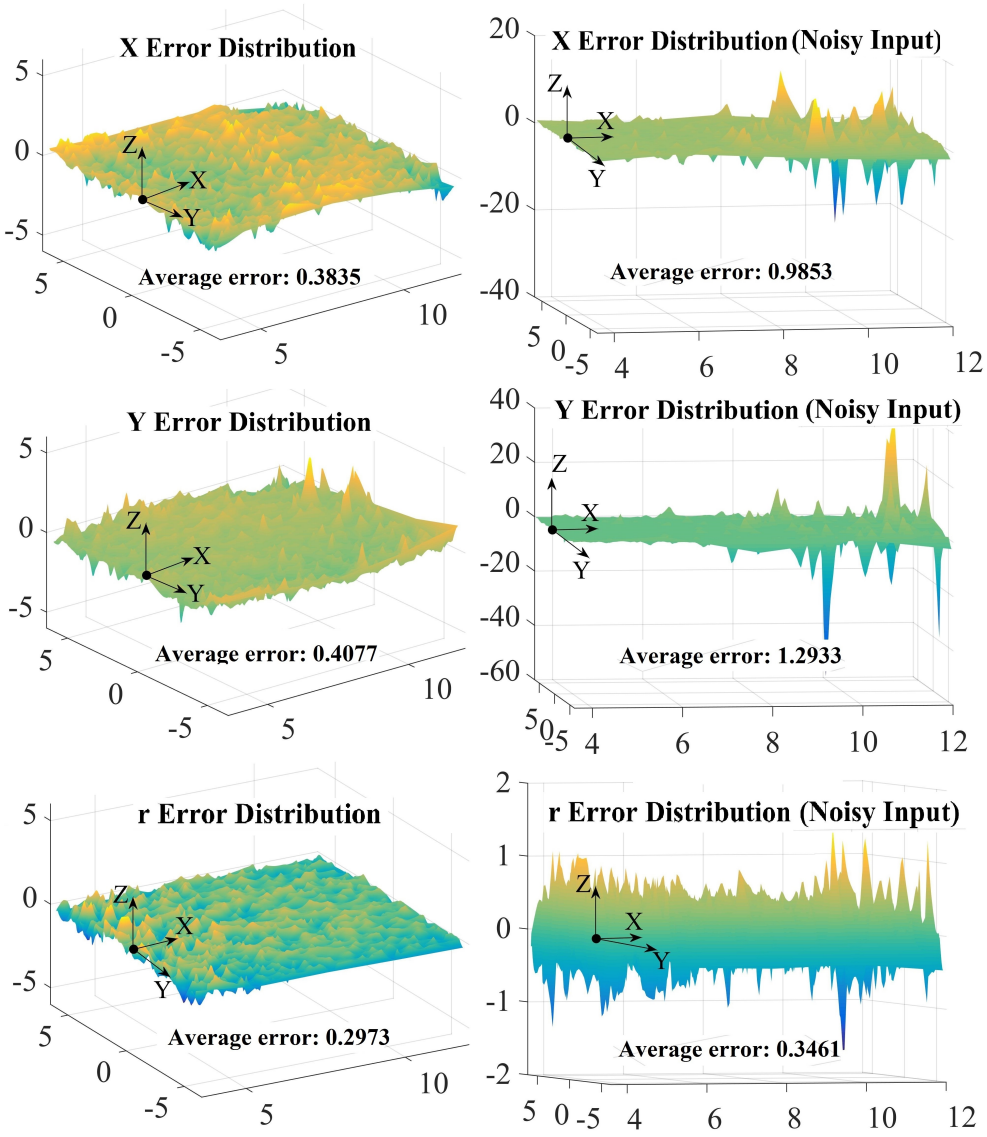

Figure 5.7: *Error distributions on x, y, r of a four-layer BPNN ([20 16 12 8]) with none-noisy and noisy simulating inputs. Unit is centimeter.*

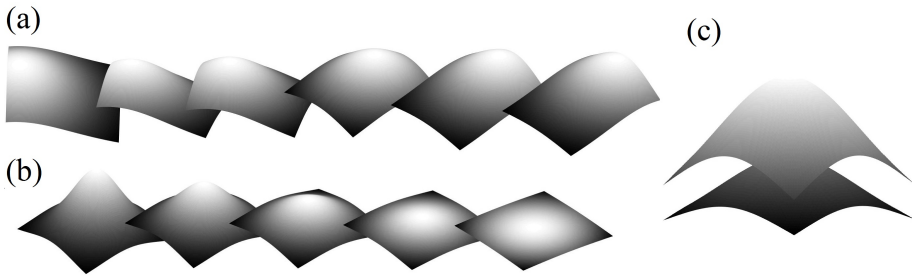

Figure 5.8: *(a) Image of a flying-by insulating sphere on a plane sensor. (b) Image of a leaving sphere on a plane sensor. (c) Signal comparison between the cube and sphere with same volume and position. The upper figure is the cube perturbation, which is stronger than the bottom sphere one.*

5.8(a) shows the perturbations on the electrical image evolve when the sphere moves along the y axis. In Fig. 5.8(b), the imaging region becomes flat and blurred when the spherical object moves away along the x axis.

Simulating signals from a sphere and a cube with same volume and position are compared in Fig. 5.8(c). As discussed in [81, 13, 15], electrical images are determined by both geometric and electric properties. Under the large conductivity contrast, volume, position and aspect ratio prove to be the most significant geometric factors. One of the intriguing questions about the ability of electrosense is to distinguish objects with similar volumes but different edges [15]. It can be seen that electric images from objects with varied edges (cube and sphere) are quite similar, which indicates a high sensitivity requirement of the sensor for such object identification problem.

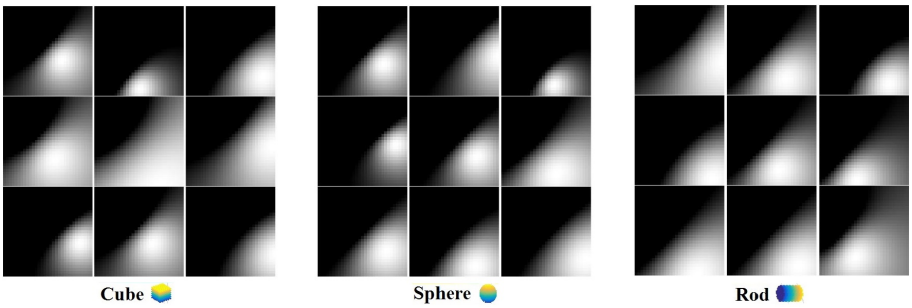

Figure 5.9: *Typical electrical images of cube, sphere, and rod. Signals were linearly mapped to [-1 1] that in image 1 is the lightest and -1 is the darkest.*

5.5.2 CNN for Identification

Traditional BPNN simply using stacked fully connected layers do not perform well on shape identification mainly because it lacks utilizing 2D spatial relations between pixels of an image. Convolutional neural network (CNN) modifies the BPNN with additional convolution layers which are proved to be essential in conventional digital image recognition. We applied this technique on electrical image identification of underwater electrosense by using a modern deep learning framework MatConvNet [85].

We used a probe matrix 6×6 cm as the coordinate in Fig. 5.2. Three categories of electrical images of sphere, cube, and rod were generated by DDA simulations with random positions, orientations, and sizes. Each shape had 2000 samples for training (80%) and testing (20%). Objects were put within the predefined sensing area: $x \in$ [3,6] cm, $y \in$ [-3,3] cm, $z \in$ [-3,3] cm and minimum enclosed sphere diameter $d \in$ [1,5] cm.

We first used a dense image with 28×28 pixels. Fig. 5.9 showing 9 typical electrical images of each group. In this simulation, a pair of point emitting electrodes at opposite corner of the sensor was used. Hence the field in front of the sensor was not as uniform as in Fig. 5.8, which made the electrical images (Fig. 5.9) more confusing for us. However, by training a convolutional neural network we found these images are distinguishable.

The network was composed of an image input layer, three convolutional layers, two fully connected layers (the latter one was used for classification output), as Fig. 5.10. Other layers included rectified linear units and pooling for subsampling. Before input layer, signals in each image were linearly mapped to [-1 1]. A fully connected layer with 256 nodes and 0.5 dropout rate were set before the output layer [82], and batch normalization technique was further applied to reduce over-

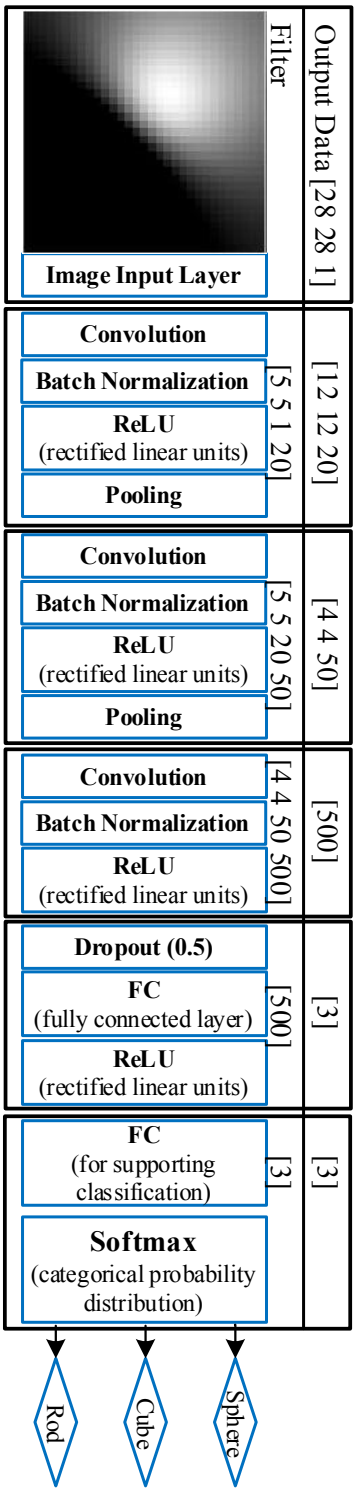

Figure 5.10: *Net structure of convolutional neural network for electrical image identification. Layers are organized into blocks, in which the filter size and output data size are illustrated.*

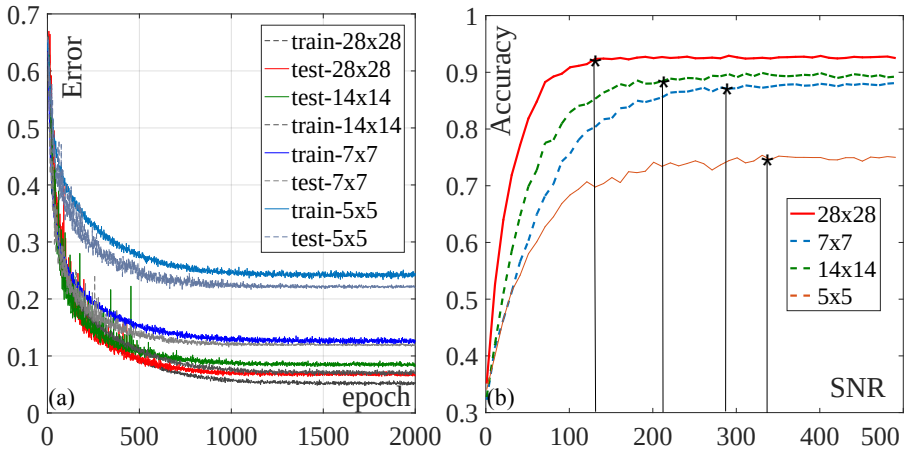

Figure 5.11: *(a) Training and testing convergence of accuracy using CNN with different image densities. (b) Training and testing accuracy with respect to different noise levels with* 28×28 *image.*

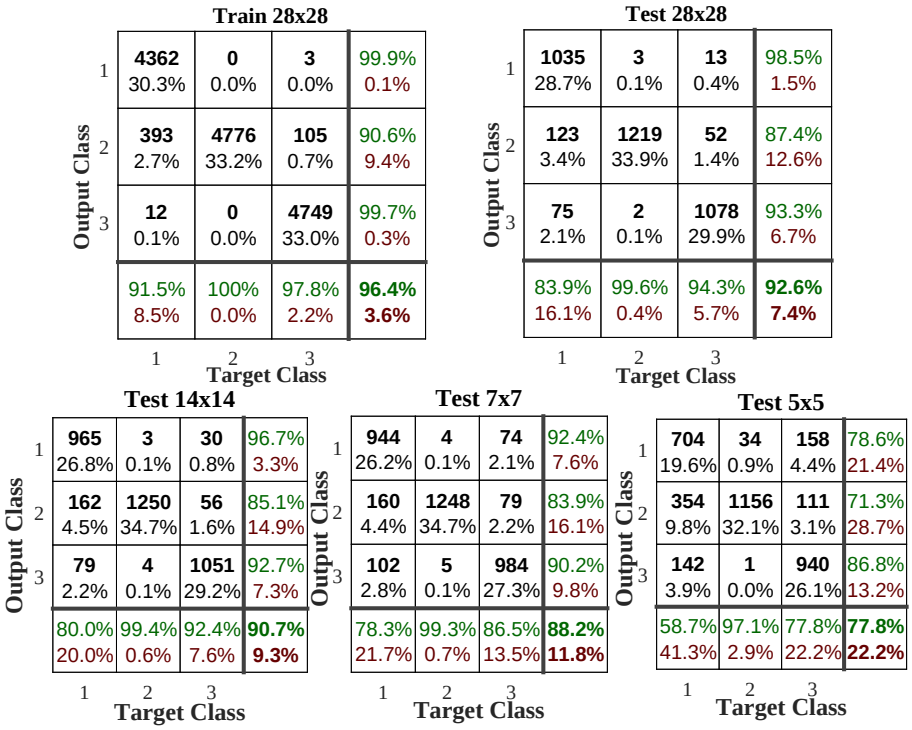

Figure 5.12: *Training and Testing confusion table of identification using CNN with different electrical image densities. Number representation: 1-Cube, 2-Sphere, 3-Rod.*

fitting and accelerate training process [43].

The network was trained using stochastic gradient descent and a logarithmic descending learning rate starting from 0.01. Each mini training batch had 128 samples, and maximum epoch is 2000. In actual training, data was augmented by flipping images up and down, right and left. The training convergence of batch error is illustrated in Fig. 5.11(a) (train-28 and test-28). We also trained a BPNN (stacked fully connected layers) with three fully connected layers of 128, 64, and 32 nodes respectively. The final testing accuracy for CNN was up to 92.6% while BPNN can only achieve an accuracy around 70%.

We further down-sampled the electrical images to 14×14 and 7×7, representing a coarser probing matrix, to investigate their identifying abilities with same training and testing data set. We used similar network structures: for 14×14 images, the net was composed of three convolutional layers and a fully connected layer; for 7×7 images, two convolutional layers and a fully connected layer were used without pooling. The training convergence of batch error is illustrated in Fig. 5.11(a) (train-14, test-14 train-7 and test-7). The overall accuracy using coarser probe matrix degraded to 90.7% and 88.2% respectively.

To evaluate the noise tolerance of object identification using CNN. It is reasonable to add noisy samples in training set to enforce the network learning noisy features, but the noise should not be too strong to submerge main features. We added specified noise (SNR = 500) to the training set and tested the network using a sample set with different noise levels, as Fig. 5.11(b). It can be seen that denser probe matrix is more immunized from noise. To achieve an ideal identification rate, probe matrix 28×28 requires a minimum SNR around 120, while 14×14 and 7×7 need higher SNR, 210 and 290 respectively.

Fig. 5.12 is the confusion table without injecting noise, where results were evaluated by removing the dropout layer. For images with 28×28 pixels, the dis-

crepancy between the classification performance on training dataset (96.4%) and testing dataset (92.6%) indicated over-fitting still existing. Interestingly, spheres were the easiest to be identified, and only 0.4% spheres were incorrectly recognized to be other shapes. There were 16.1% misclassified cubes, in which most of them were recognized as spheres. This result again validated the conclusion in [15] that sphere and cube have the same aspect ratio and similar projection shapes, as in Fig. 5.8(c), therefore to distinguish them using edge information is more difficult. Actually, some small and far-field cubes lost their shape edge information and acted as spheres. Rod has a long aspect ratio that is easier to be identified, and only 5.7% rods were misclassified.

Instead of saying spheres are easier to be identified, it is better to say they have least distinguishable features, no edge or long aspect ratio. Objects are identified by features, and if they lose feature information on sensing images due to the small size or far range, they will be classified into a sphere. This can be validated from identification using images with 14×14 and 7×7 pixels, misclassification rate dramatically increased for cubes and rods, while for spheres it kept stable, 0.4% to 0.5% and 0.6%. Coarser probe matrix loses more information on object features.

5.6 Conclusion

This chapter describes the sensor design and corresponding sensing algorithms. For both 1-D and 2-D sensor case, unscented Kalman filters can be used to estimate the size and location given the object shape. On sensing algorithms of underwater electrosense using proposed 2-D design, we have following conclusions: (1) Object projection on a sensing plane (electrical image) can be used for shape identification by training a deep convolutional neural network. Its identifying

ability is determined by the accuracy and density of signals (pixels). Some geometry features such as aspect ratio are easy to distinguish, while some others such as edge difference are more difficult. (2) Given the object shape to be a sphere, we can train a neural network for position and size estimation. The size estimation is more immunized from the system noise than other properties. (3) On object localization, the neural network has the advantage over unscented Kalman filter which requires forward calculation for each sigma point in each iteration. However, this computational burden can be overcome by parallel computing.

Chapter 6

Prototypes and Experiments

6.1 Introduction

Theoretical studies in previous chapters demonstrate principles and algorithms of underwater electrosense. Applying these techniques on real underwater robots depends on further implementations and experimental tests. This chapter explored active underwater electrosense in the laboratory environment. Three basic points shall be considered before building prototypes. First, the underwater electric field is complexed by environmental conditions. Due to the power line effect, a 50 Hz noise (Australian standard) is easily coupled to the electronics. There is also a near-ground static field as a result of atmosphere activities. Thus a simple static field implementation is not plausible as well. The active sensing system should run between 1 KHz to 100 KHz to achieve a best adaptive performance. Second, the electrodes data acquisition demand a fast, stable, accurate, and multi-input measurement system. These system requirements and indicators usually conflict with each other that we need a higher level trade-off based on overall system design. Third, experimental study of the sensor in the laboratory is still far from robotic applications. In most robotic computing and electronics system, the

hardware resources are limited, but the performance and reliability still cannot be sacrificed.

6.2 A 5×5 Planar Sensor

6.2.1 Prototypes and Electronics

The 5×5 Sensor consists of emitting electrodes to establish the electric field by injecting current and probing electrodes to sense the potential perturbations. According to the DDA theory of underwater electrosense, each small emitting electrode with controlled injecting current can be seen as a point source with controlled electric charges. Thus the incident field is completely determined and controlled. The electric potential is taken between a pair of probing electrodes, rather than between the electrode and system earth, to suppress common mode noises.

To make the electric field more uniform, we can arrange the number of the pairs of the emitting electrodes and their locations. A quadrate sensing plate is designed, and each corner has a spherical emitting electrode fastened. More probing electrodes tell more information about the environmental variation, but it is hard to increase the amount because of the prototype electronics limitation (more wires and circuits). Here we design a 5×5 probing matrix, which will generate a 5×5 pixels electrical image representing the sensing region projection on such plane.

Fig. 6.1 shows the model and prototype of the electrosensor, and the functional diagram is shown in Fig. 6.4. The whole size of the probing matrix is $6cm \times 6cm$. In simulating the model using DDA approach, we only consider pure electrodes, neglecting the electrode carrier or sensor base itself. However the ac-

tual prototype is made from PCB board and wires and connectors, even though we have hollowed out several parts to reduce the effect (left one in Fig. 6.1). For applications that the body, sensor or sensor carrier (such as a robotic fish) cannot be neglected, we can use a successive reflection method [20] to model the interaction between the objects and the sensor body itself, which can be applied in DDA approach as well.

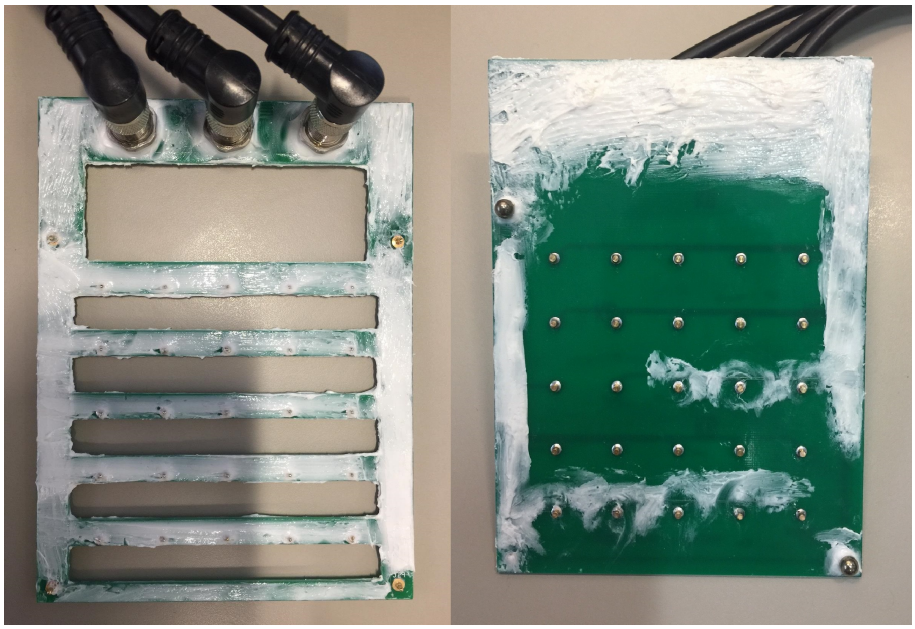

Figure 6.1: *Prototypes of membrane sensor. Left figure is a two-side sensor whose electrodes are exposed to water on both side, reacting to objects from each side symmetrically. Right figure is a one-side sensor whose electrodes are insulated from water on the other side. White material is silicon sealant for protecting connectors and via holes on PCB board.*

Another design is only to sense one side of the membrane (right one in Fig. 6.1), which means the electric field will not propagate to the other side. The probing electrodes are also set on one side only. Theoretically, this requires the membrane to be insulated and infinitely large, and in that case, we can simply utilize the image method to obtain the consequence that the field strength will be doubled compared to the original design. While in practical application, the field will inevitably leak to the other side. As a result, the field strength on sensing

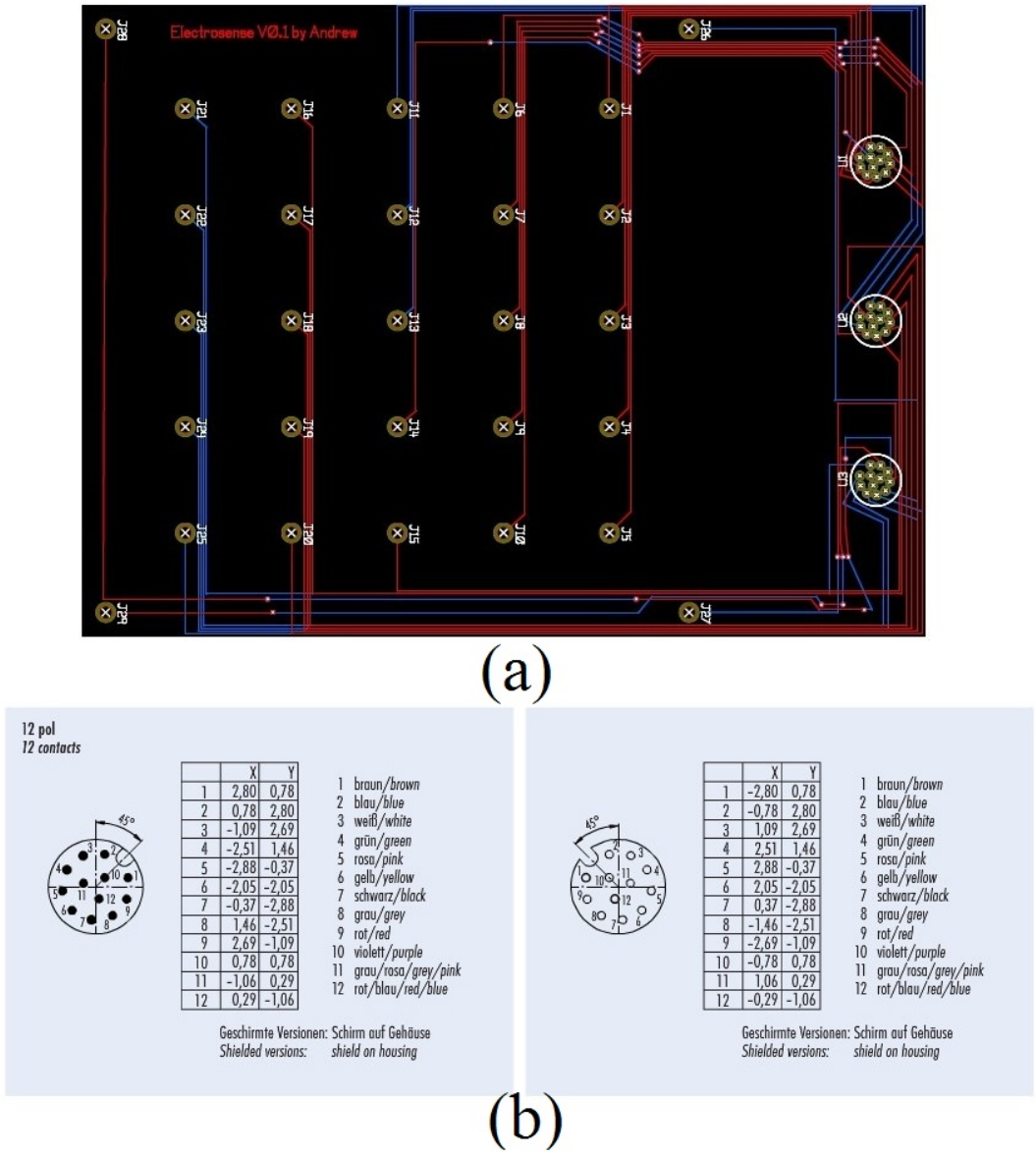

Figure 6.2: *(a)Top (red line) and bottom (blue line) view of the pcb board design of the* 5×5 *sensor. (b) Connector pin instructions.*

side will be less than twice of the original design. The real fish skin is nearly a surface of a long and narrow ellipsoid, which is apparently a single side sensor.

A PCB board design is illustrated in Fig. 6.2(a). The 25 electrodes are directly lead to three connectors as pin showed in Fig. 6.2(b). These connected are further wired to a current source and a multi-input voltage meter.

As the prototype showed in Fig. 6.3, a three degree-of-freedom platform is in-house designed and manufactured for translating and rotating the sensor. Each freedom is driven by a step motor controlled with Arduino and motor driver board, which offers a serial port interface to Matlab on PC. We use commercial stimulating and measuring modules from National Instruments. These modules are fully configurable in Labview and can be seamlessly interfaced to Matlab through build-in script node. The output range of current source is $\pm 20mA$ with a maximum load of 600Ω. While operating at the finest scale $\pm 200mV$ of the potential meter, the absolute accuracy is $157\mu V$ and the sensitivity is $4\mu V$.

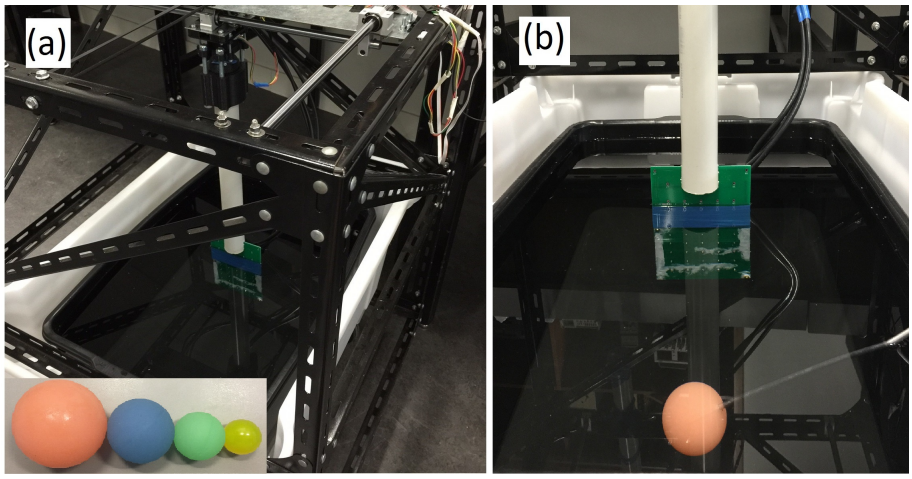

Figure 6.3: *(a) Tank and motion platform with three degrees of freedom, with experimental rubber spheres of different sizes. (b) Sensor action in the water, with stimulating and measuring electronics from Nation Instruments.*

The overview of the signal processing is illustrated in Fig. 6.4. For simplicity, only a pair of diagonal emitting electrodes is used to inject a current signal

from stimulating source. To reject noise and reduce chemical reaction between electrodes and water, the current is modulated into a square wave at 1kHz. For this processing system, the signal is mostly digitally processed by software except for the high-speed sampling hardware. The square wave is easily generated by the program, and receiving signals on probing electrodes are synchronously demodulated into in-phase and quadrature components. Before the demodulation, a high pass filter is utilized to removing the DC part, and the synchronous demodulation itself acts as a super narrow band pass filter which will reject all AC components of the noise. After the demodulation, a low pass filter is set to get the final attenuation value.

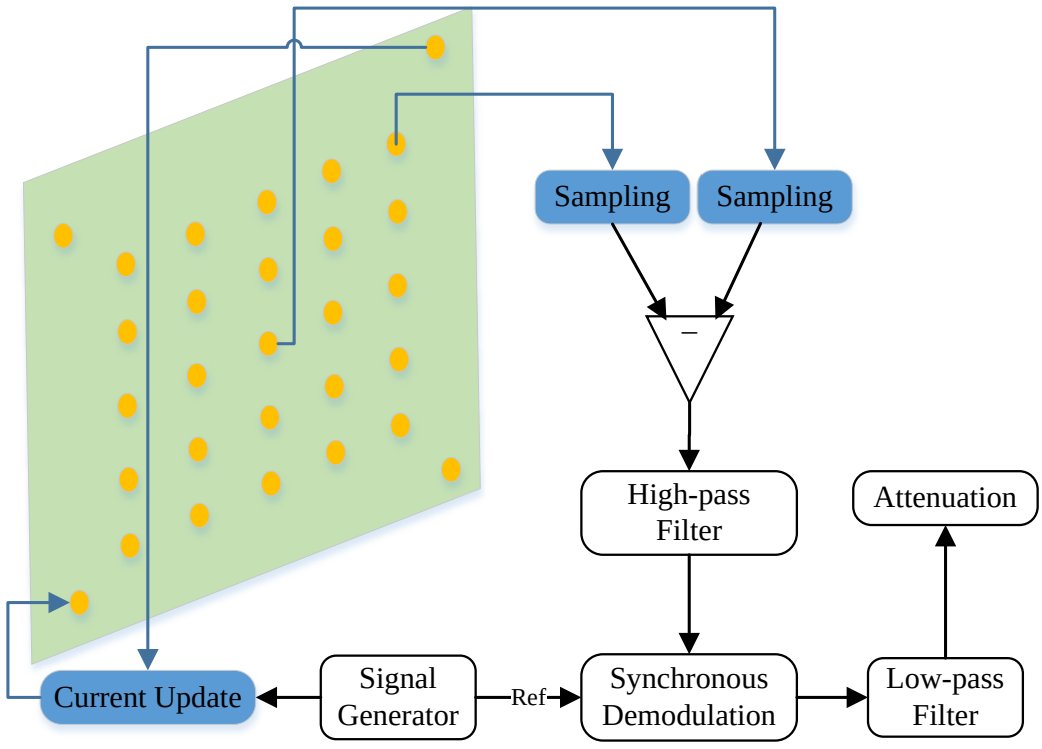

Figure 6.4: *Signal processing flowchart. The hardware works including sampling and signal update are illustrated in blue blocks, while other procedures are digitally conducted in software.*

In addition to the resistant assumption of the theory, for real application, we need to consider the reactants of the water, the cables and the environment

like the tank. Also, there will be contact impedance between the electrode and the water. Further, the water impedance will change with the temperature and is hard to precisely determined without special instruments. And the geometry and electrical properties of the actual prototype will be slightly different from the simulating model. These practical influences will lead to signal mismatch between numerical simulation and experiments.

The strategy on solving these problems is by adjusting the simulation parameters to match the electric field when no object appears. Because the electric field is uniquely determined by the potential distribution, if the simulating potentials on probing electrodes are matched to the experimental ones, then the electric field is believed to be matched. Consequently, perturbation signals of the object, which are used in the sensing algorithms, are believed to be consistent.

More specifically, two parameters including the injecting current and the water conductivity are referred. The experimental and simulating current are set to be the same, but the water conductivity is a variable in the simulation. After the experimental potentials are collected, we run a series of simulations to search for the best value of the simulating water conductivity, which will minimize the mean square error between experimental and simulating potentials. After that, the perturbation signals are also matched, and we can use these parameters in sensing algorithms.

6.2.2 Empirical Results

In the experiment of object sensing, we simply combine the data-driven neural network and signal-matching unscented Kalman filter in order. The first algorithm is used for coarse detection while the second one is used for further precise localization integrated with the sensor motion. Four insulated rubber spheres

with radius 5.5 cm, 4.2 cm, 3.2 cm and 2.5 cm are used. The task is to detect the sphere and determine its size and position.

By running the signal matching process parameters of the simulation are chosen, with injecting current 2 mA and water conductivity 0.218 s/m. Fig. 6.5 shows the comparison of the matched simulating and experimental potentials and according to perturbation signals under the same electric field. The reference electrode of the sensor that potential equals to zero is illustrated in Fig. 6.5. The precise signal matching between experiment and simulation is crucial for the algorithms proposed here because it will ensure the success of sensing experiment.

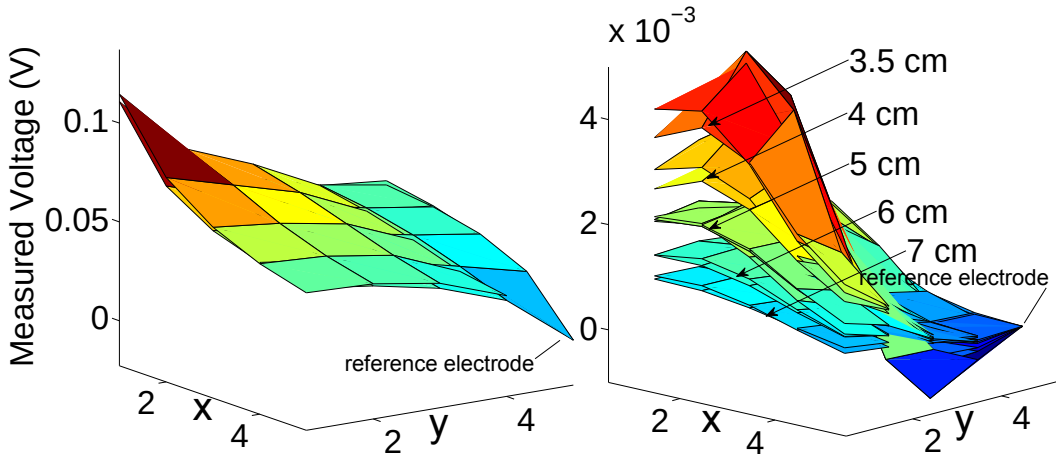

Figure 6.5: *(a) Potentials of simulation and experiment. (b) Potential perturbations comparison under specific potentials matching, with different distances from the sphere centre to sensor plane along the midperpendicular line.*

A 4-layer neural network [20 16 12 8] is trained to map the perturbations to object properties directly. To evaluate the performance of this algorithm, we test the experimental results along the midperpendicular (x-axis) and parallel direction (y-axis) of the sensor at several positions (Fig. 6.6). The aforementioned simulation performance, which is the best expectation in the experiment when the perturbations are exactly same with simulating ones, is around 5 mm. While the average empirical performance is around 10 mm base on the testing points.

The results are more coherent and consistent along the y-axis because the underwater electrosense is near-range effective, and we can see that errors become significant when the object is going further. However, due to manufacturing flaws, errors distribution along the y-axis were not symmetric. This is mainly because the 25th electrodes were incorrectly connected to the nearby emitting electrode. This problem was fixed in the next edition of electrosensor with 256 electrodes (16×16).

After the neural network detection, the mapped sphere radius and positions are used as the initial guess in unscented Kalman filter. This will inversely match the simulating signal to the collected experimental signal by searching for the best state. As an example, Fig. 6.7 illustrates the process of decreasing the localization error by applying constrained unscented Kalman filter at the position of 5 *cm*. In this case, there is no sensor motion to introduce other uncertainties. But for the current prototype this process is only ensured when the object is very close to the sensor. Otherwise, the noise will submerge the precision as the perturbation signal reduces quickly.

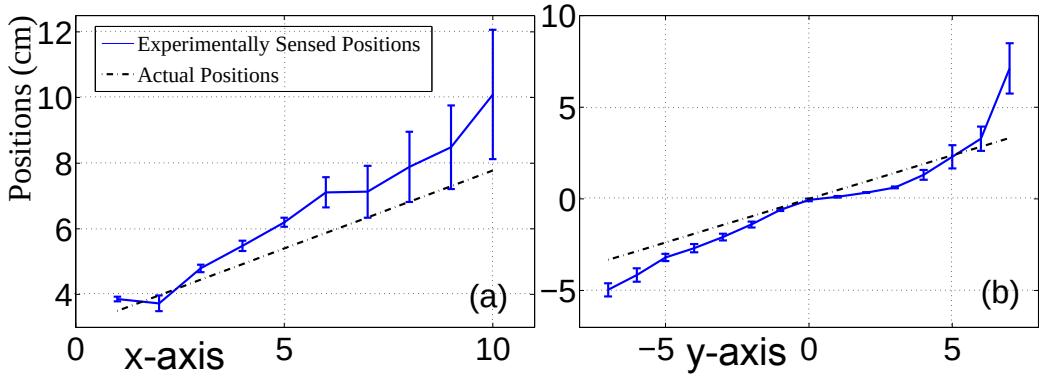

Figure 6.6: *(a) Actual and sensed positions comparison along the midperpendicular direction (x-axis) using a rubber sphere with radius* 5.5 *cm. (b) Actual and sensed positions along the parallel direction (y-axis) using the same sphere at a distance of* 5 *cm.*

Both algorithms introduce some assumptions about the object to be sensed,

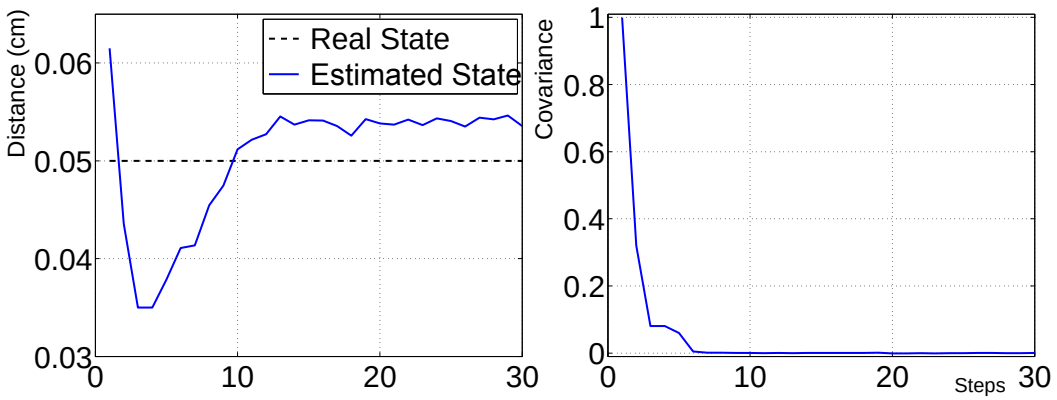

Figure 6.7: *Further precise distance recognition using constrained unscented Kalman filter when the object is within the close near-range.*

which is different from the whole-domain imaging methods used in EIT. This indeed adds constraints to the problem and make the precise detection and localization possible by only using a limited number of probes. The one-step neural network can introduce some systematic errors that we can notice from the Fig. 7, where the mapping results tend to overate the distance to the sensor on x-axis and underestimate the distance to the center on y-axis. However, the method of step-by-step Kalman filter can ease this systematic error and search for the best state of signal matching, and the residual errors only come from the data acquisition chain or manufacturing defects of the prototype.

6.3 A 16×16 Planar Sensor

6.3.1 Prototypes and Electronics

We further made a 16×16 electrosensor prototype to capture electrical images underwater in a tank. The neural network inherited parameters that were obtained from simulation data set as initialization, and it was further trained using experimental data. This section first explained the considerations in building prototype, choosing electronics, and acquiring data. Then the procedure of col-

lecting electrical images of three kinds of insulating objects - sphere, rod, and cube - was presented in detail.

The designed electronics works in following way. The signal generator creates 10 kHz voltage signal, which is converted to a bi-directional current with the same waveform using Howland current pump. The current excites the water through emitting electrode and establishes a controlled underwater electric field. Probing electrodes were connected to an instrumental amplifier through multiplexers, and incident voltages between probing electrodes and a reference (specific one of the probing electrodes) need to be measured. The voltage signal from signal generator acts as a reference in a lock-in demodulator for acquiring in-phase and quadrature portions of the incident voltages.

Electrosense signal is modulated to sinusoid wave with frequencies between 1 kHz to 100 kHz because dc or low-frequency signal is highly contaminated by power line networks. Another reason as studied in [72] is due to the neutral impedance of water at these frequencies. The waveform could also be square [15], but as a square wave was combined by sinusoid waves with increasing orders, the corresponding water impedance is different. In this work, we modulated the signal with the sinusoid wave around 10 kHz.

It is possible to acquire the incident voltage in its original sinusoidal form using a fast and accurate analog-to-digital converter (ADC). Then all the filtering and demodulation can be solved in software. However, as the amplitude of the signal is relevant, the sampling frequency should be high. According to the formula on maximum amplitude error e_{max} and sampling frequency N times of the signal [37]:

$$e_{max} = 1 - cos(\frac{\pi}{N}), \tag{6.1}$$

There is an about 120 ppm error when $N = 200$, i.e., the sampling frequency is 2 MHz when the signal is 10 kHz. Fast ADC with high resolution makes the direct digitalization of original sinusoidal signal non-economical. An alternative method is organizing an analog chain for signal processing. By using an analog lock-in amplifier, the AC signal is converted to DC corresponding to its amplitude. The electronics overview is illustrated in Fig. 6.8. Due to the strong drift of analog multipliers, they actually cannot be used in lock-in amplifiers. Instead, IC AD630 uses a reference signal to control a switch of the signal, whose effect is the multiplication of the sinusoidal signal and a square wave. Because a band-pass filter was applied before the demodulation, effects of higher-order components of the square wave could be eliminated. Thus we can get the desired lock-in amplifier.

A digital-to-analog converter (16 bits DAC) was used to offset the DC output from lock-in amplifier and low-pass filter, as the perturbation was far smaller than the base signal. The 24 bits ADC could sample at maximum 30 kSPS. The design was implemented using separated modules and interconnections of coaxial cables as illustrated in Fig. 6.9(a).

The sensor was manufactured using a single piece of PCB board, as in Fig. 6.9(b). The 16×16 probing electrodes constituted a $9cmcm$ matrix. Each 16-to-1 multiplexer was connected to a column of the matrix, and an extra multiplexer finally routed outputs of 16 ones to the electronics using shield cables. The MCU sent digital controlling signals to the multiplexer, and the Howland current pump supplied current to two emitting electrodes, through Dupont wires. The PCB board designs on both sides are showed in Fig. 6.10.

The electrodes were made by soldering tin balls to bonding pads on PCB board. The entire sensor was protected by waterproof paint (clear epoxy resin). It is important to use relatively large probing electrodes when measuring voltage

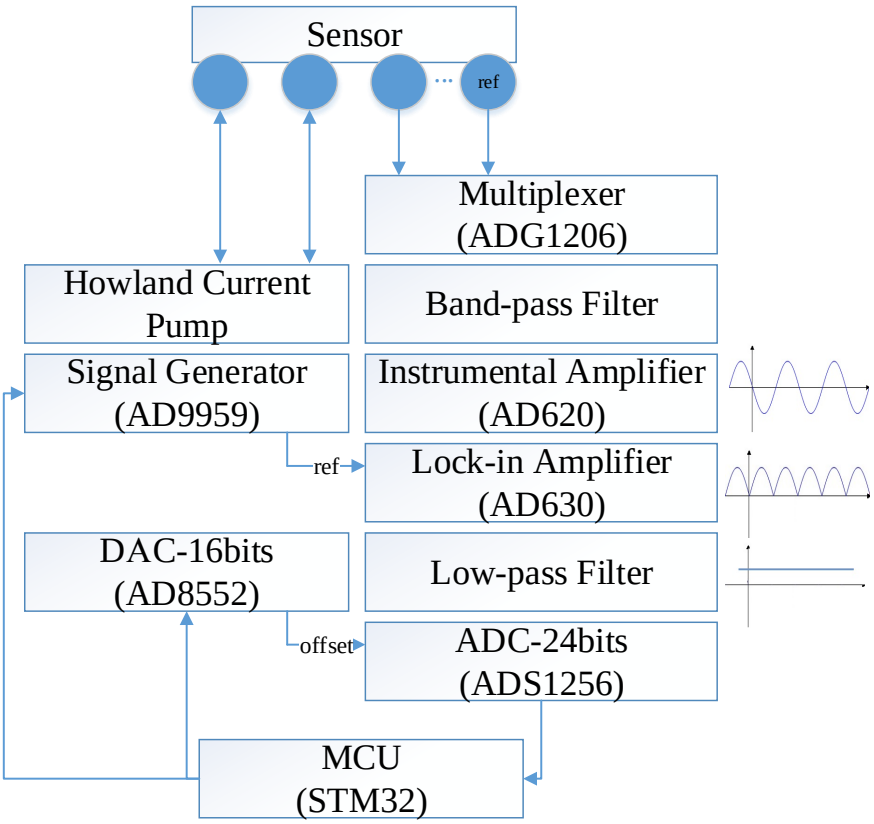

Figure 6.8: *Overview of electronics. The functional block contains the main IC name used in the circuit. Solid blue circles represent electrodes, in which two left ones indicate emitting electrodes and two right ones are probing electrodes corresponding to current injection and voltage measurement. Processing of sinusoid signals with noise are shown beside instrumental amplifier, lock-in amplifier and low-pass filter.*

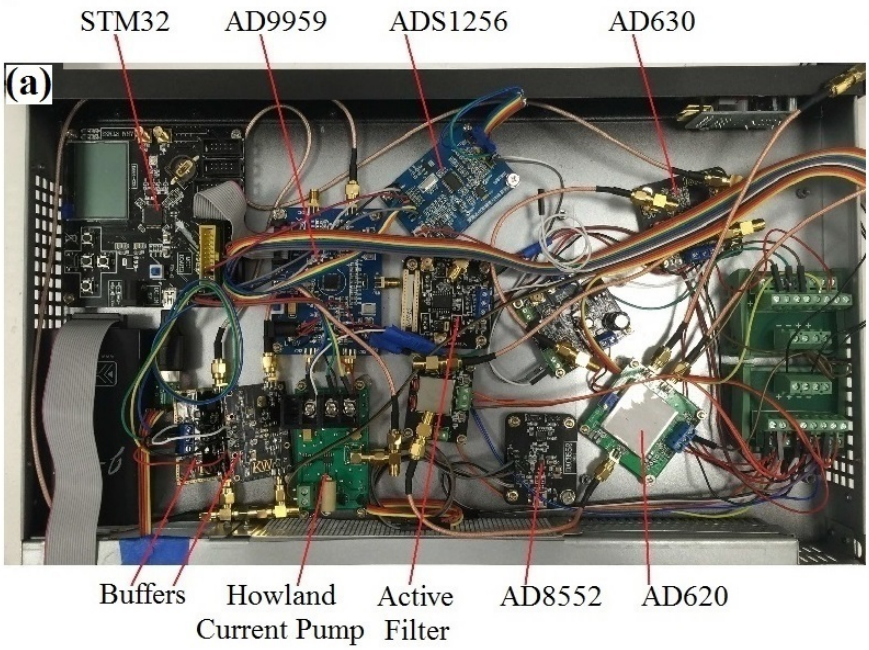

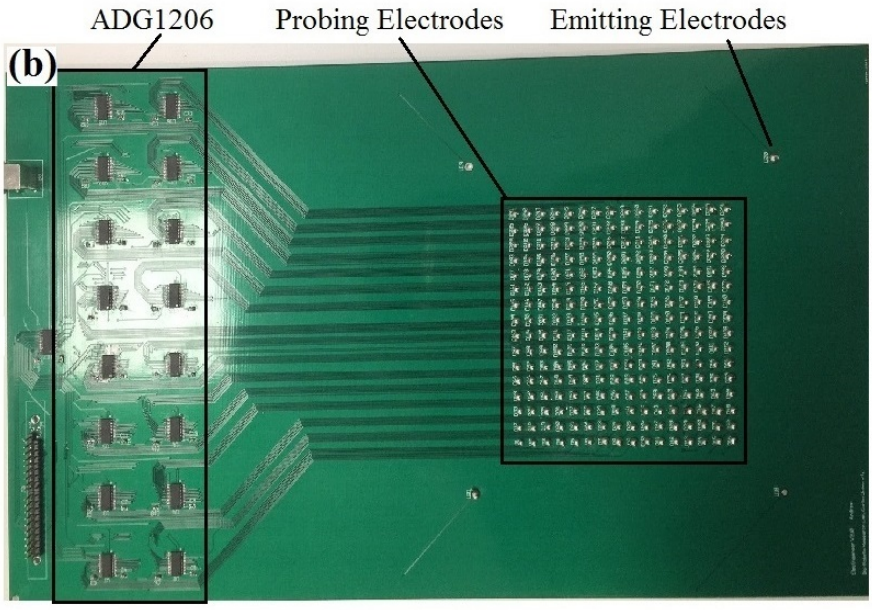

Figure 6.9: *(a) Electronics prototype was a combination of analog modules. Analog signals were transmitted between them using coaxial cables with SMA connectors (gold). Main functional ICs of each module are listed. (b) The sensor prototype was made from PCB board with a two-layer multiplexer that maps* 16×16 *electrodes to a single output port.*

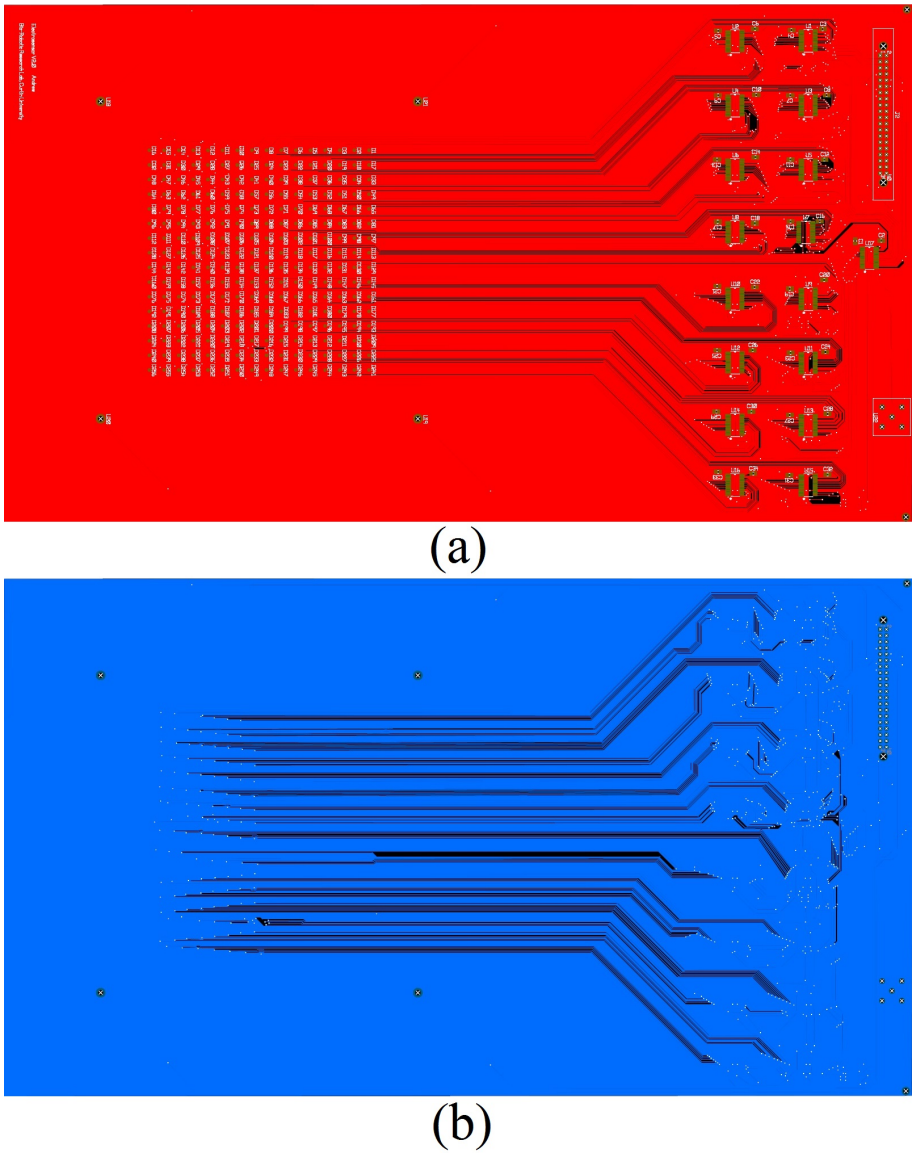

Figure 6.10: *(a) Top view of the pcb board design of* 16×16 *sensor. (b) Bottom view of the pcb board design of* 16×16 *sensor.*

underwater because small air bubbles or impurities attached to the electrodes will significantly affect the results if using small electrodes. In this prototype, the diameter of electrodes is approximately 5 mm.

The image was captured in a scanning manner by multiplexing 256 electrodes to the processing electronics. One disadvantage of using lock-in demodulation in a multiplexing manner is the settling time of the low-pass filter. When connecting the channel from one electrode to another, the ADC can only start sampling after a rise time. For a simple first-order RC low-pass filter, the rise time from 10% to 90% is about $2.2RC$ or $0.35/F_c$. As in Fig. 6.11, the rise time of a low-pass filter with cutoff frequency 7 Hz is about 50 ms. The lower cutoff frequency, the longer rise time. The trade-off in this prototype was using a higher cutoff frequency, sampling the output of the analog low-pass filter and conducting a digital low-pass filter (average) by software. When used a 1 kHz cutoff frequency (rise time 0.35 ms) and used the same sampling time (0.35 ms) on each electrode, we could capture maximum five images per second.

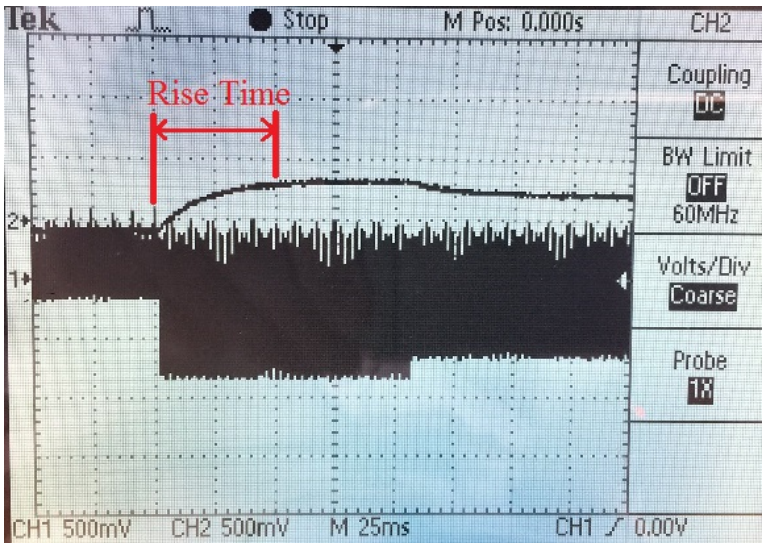

Figure 6.11: *Rise time of the low-pass filter. Channel 2 is the output of synchronous demodulator, and channel 1 is the output of following low-pass filter.*

6.3.2 Empirical Results

The moving platform with two degrees of translational freedom and a degree of rotational freedom, as in Fig. 6.12, drove the object in a plane. The automated data collecting program first drove the object to a random location and orientation in front of the sensing plate; then it controlled electronics to take an electrical image of the object.

Three insulating objects were also specified, including a sphere of radius 1.5 cm, a cylinder of radius 1 cm and height 3 cm and a cube of edge 2 cm. These objects were driven randomly within a confined space of [-4, 4] cm on the y-axis, [0, 6] cm on the x-axis, and the orientation [0, 360] degrees. Thus the gathering of the experimental data set was not the same with the simulation. In the simulation data set, the size and six degrees of freedom of the object were changed simultaneously, whereas in the experiment only three degrees of freedom were changed. Electrical images were taken at two manually specified level planes to expand the data set at a different depth (z-axis), and 3469 images for each object at each depth were collected.

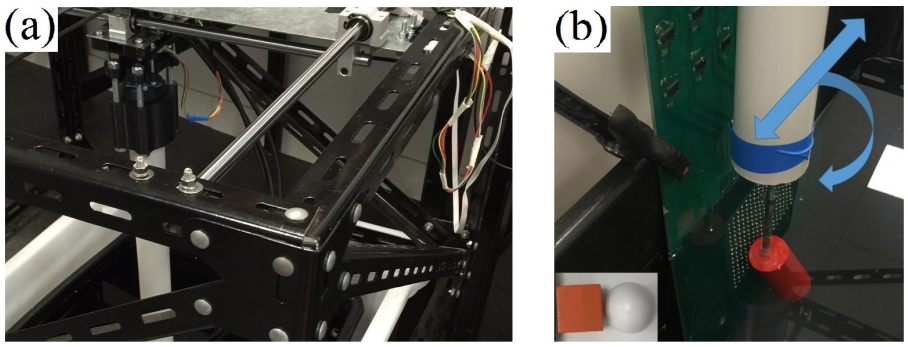

Figure 6.12: *(a) Three degrees of freedom moving platform for driving the object. (b) Take electrical images of the object in different positions and orientations.*

Training neural network for experimental data shared a similar structure for simulation data as seen in Fig. 5.10. It has an image input layer, three convolutional layers with 3×3 filters, and a fully-connected layer with 0.5 dropout rate.

The training convergence of batch error is shown in Fig. 11(a). The network training was convergent at fifth epoch, which was dramatically faster than training simulation data. Moreover, the final testing accuracy of object recognition was up to 95.0% while in simulation this value was 92.6%.

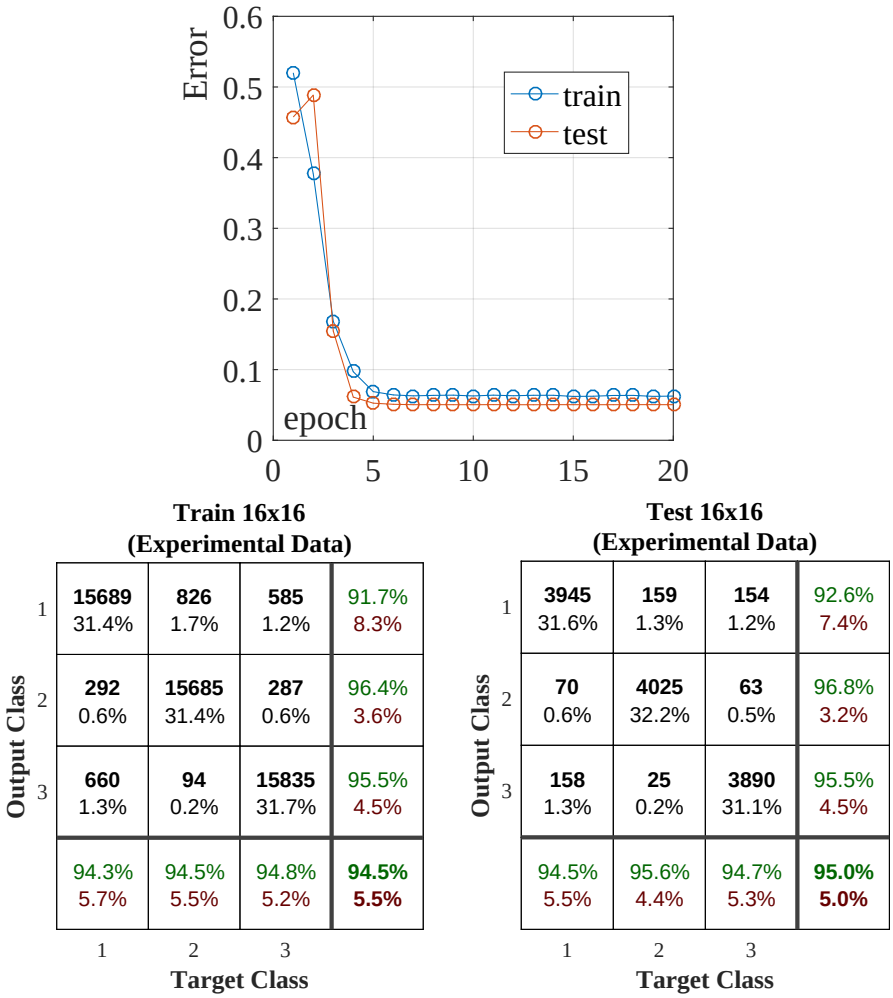

Figure 6.13: *Training convergence and confusion table of empirical identification. 1-sphere, 2-cylinder, 3-cube.*

The training and testing confusion table were illustrated in Fig. 6.13. In the test, 95.6% cylinder images, 95.1% sphere images, and 95.7% cube images were correctly classified. Compared to simulation in which objects have different sizes, the error rate on classifying other objects to the sphere was significantly decreased.

The sensor can distinguish the perturbation images created by a specified cube, a sphere or a cylinder. The experiment demonstrated the potential of object identification with real underwater electrosensor.

A simple back-propagation neural network was further trained to directly map the perturbation of the insulated sphere (radius = 1 cm) to its locations. The training data was collected at the center depth plane of the sensor (z = 0) within the range [-4.5 4.5] cm on the y-axis and [2, 10] cm on the x-axis.

To evaluate the performance of this method, we tested the experimental results along the midperpendicular (x-axis) and parallel direction (y-axis) of the sensor at several positions (Fig. 6.14). The testing points in the figure were collected within a range [-4 4] cm on the y-axis and [3, 8] cm on the x-axis. The aforementioned simulation performance, which was the best expectation in the experiment, is around 4 mm. The average empirical performance is around 5 mm base on the testing points, and this result was much better than a previous prototype [95].

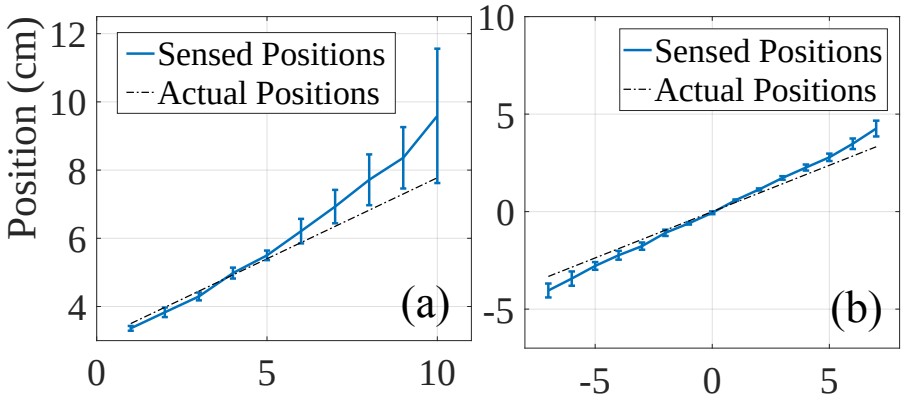

Figure 6.14: *(a) Actual and sensed positions comparison along the midperpendicular direction (x-axis) using a rubber sphere with radius* 5.5 *cm. (b) Actual and sensed positions along the parallel direction (y-axis) using the same sphere at a distance of* 5 *cm.*

6.4 Discussion

One of the difficulties on manufacturing high-performance underwater electrosensor lays in designing sensitive and stable electronics. As discussed in previous sections, the field perturbation bears information of object's location and shape. First, the perturbation is quite small relative to the base signal (generally 1% to 10%). To achieve a good resolution of perturbation, for example, 1% resolution, the overall sensitivity of electronics should be controlled within 100 ppm (parts per million). Second, signals on the probing matrix have a large dynamic range because the perturbation reduces linearly with the square of the distance.

Improving the data acquisition speed and stability is the key to the successful design of electrosense electronics. First, making the image capture faster enables a better record of perturbations of moving object. This is crucial to the robotic application. Inspired by the event-based camera, we are building similar electronics that only record the change of the electrode voltage (differential circuit). This technique can sense the object moving faster.

Second, data acquisition stability is more important than absolute accuracy of voltage measurements. As feed-in images of neural network were normalized to [-1 1], it is the measurement consistency of all electrodes that matters. We found small electrodes (less than 1 mm) were subject to significant noises by small bubbles and impurities. The analog signal chain also has an inevitable and variable drift during the measurement. However, as the entire image needs to be centered and normalized before feed into the neural network, the electronic drift does not affect if the drift changes slowly or the sensor captures fast.

6.5 Conclusion

This chapter presents electrosensors that can operate in a full 3-dimensional mode. Algorithms on the object localization were designed and tested based on numerical methods of electric field forward simulation. We combined the statistic learning method by training a multi-layer neural network and a probabilistic approach by applying a constrained unscented Kalman filter (CUKF). This exploits the merits of fast estimation and precise signal marching process. To tackle object identification using underwater electrosense, we further proposed a planar electrosensor with dense electrodes, and an analog signal processing chain was designed and implemented to acquire electrical images of an underwater object. The convolutional neural network was trained first with simulation data to identify sphere, cube, and cylinder. Results demonstrated the sensor ability of identification changed with electrodes density and data accuracy. Our empirical studies showed that the real sensor was able to identify the specified sphere, cube, and cylinder.

Chapter 7

Conclusion and Future Works

7.1 Recap and Conclusion

The thesis first reviewed the important literature of the biological and artificial electrosense in detail. Four basic principles of biological sensing system were concluded to be energy saving, material saving, specificity, and redundancy and parallelization. The study of engineering underwater electrosense has two related aspects, theoretical and empirical studies. Several technologies manipulating electric field for sensing purpose were introduced for inspiration and comparison. After an in-depth review of the related technologies, the sensing problem was modeled using the theory of electric-quasistatic field and was classified as a forward problem and inverse problem. The environment electrical property (impedance distribution) is the system parameter along with the sensor boundary and exciting source, and the measurements taken on the sensor boundary are system observations. To predict the system observations from the parameters is a forward problem, which should be physically well-posed, but to infer the parameters of the model from observations is an ill-posed inverse problem. The solution of the inverse problem was formulated using a probabilistic way, which allows for

a unified and consistent theory.

The first approach proposed to use techniques from electrical impedance tomography (EIT) for sensing modeling. The EIT uses finite element method (FEM) as a forward model for calculating observations and representing the environment. Given the stimulating current and conductivities on meshes, FEM calculates the potential and current field, including the voltage between electrodes which predict real measurements. In sensing problems, linear and nonlinear inverse methods were formulated. The inverse problem is to assign a proper conductivity value to each element, which is called reconstruction in EIT, to make the calculations best fit the real measurements. The meaning of 'best fit' can be expressed in an optimization problem based on the probabilistic formulation. An eel-like electrosensor was further designed and simulated using proposed techniques. This work explored the feasibility of EIT methods for electrosensor.

Another approach targets on reducing the computational burden of the forward problem by introducing the method of discrete dipole approximation (DDA). Techniques in light scattering problems were for the first time expanded to active underwater electrosense. Numerical solutions of the volume integral equation were formulated, including a method of moment and discrete dipole approximation (DDA). We found that only DDA was suitable for conductive mediums and the connection between DDA, and a well-known sphere perturbation formula was further established. DDA was found to perform more than 100 times faster than FEM with only a 10% relative difference in underwater electrosense problems.A DDA-based unscented Kalman filter was proposed for inferring object size and location, and a one-dimensional sensor was made for further experimental validation.

The sensor design and the sensing algorithms applied in electrosense are tightly related. It has been a challenge in identifying objects with similar vol-

umes but different edges. We built a planar sensor that was motivated by the analogy between retina vision and electroreceptor vision. Just like the vision on a retina, the electrical image on the planar sensor can be interpreted as a projection from a 3D space to a 2D surface, but with a more complicated projecting law. Based on the planar sensor design, we first demonstrated the usage of the back-propagation neural network (BPNN) and unscented Kalman filter (UKF) on localizing an object. Further a convolutional neural network (CNN), which is widely used in digital image recognition, was for the first time applied for object identification in underwater electrosense. In the simulation, the overall success rate using CNN on identifying arbitrary spheres, cubes, and rods is 92.6% by a 28×28 electrode array.

We built two editions of planar underwater electrosensor to test and validate the design and algorithms, including a 5×5 sensor with electronics from National Instrument and a 16×16 sensor driven by a self-made analog signal chain. Experimental results of the first sensor showed that the detection and localization of our prototype were quick and accurate, with the error of around 10 mm using one-step neural network mapping and about 5 mm in close-range using Kalman filter. In the second experimental test, the prototype with 16×16 electrode array achieved an overall success rate of 95.0% on identifying the specified cube, sphere and rod.

7.2 Limitations and Future Works

Through investigations in this thesis, we found a vast potential of applying underwater electrosense to practical robots. The sensing algorithms of electrosense stand firmly based on electric-quasistatic field and probabilistic view of the inverse problem. In addition to the intuitive method transplanted from EIT community,

we also found a new DDA method for the forward problem calculation. Sensing algorithms including unscented Kalman filters and convolutional neural networks proved effective in the inverse problems. However, the goal of successfully applying artificial electrosense to practical underwater robots requires further studies. Future work within the horizon of author includes two aspects.

There are some limitations of this research in term of theoretical assumptions, algorithms and hardware implementation issues to be addressed, and based on them we propose possible directions of future works.

There are several assumptions of the theoretical study of underwater electrosense. First, the conductivity contrast between the invaded object and ambient water is the main parameter we considered. However, the theory of FEM and DDA can take full impedance into account, which demands multiple frequency implementations of hardware. Second, the DDA approach only considers incident field generated by electrodes using image method. Whereas in more general cases, the sensor itself has special shapes and the incident field need to be recalculated.

In term of sensing algorithms, we need to consider multiple objects identification and localization problems. The EIT approach can theoretically deal with multiple objects identification problem because the whole domain can be reconstructed. However, due to the natural dispersive feature of EIT method, the localization precision may be low. The electrical image of two objects is twisted projections with each other, which does not obey the simple superposition law. More sophisticated sensing algorithms shall be studied.

Current hardware implementation is a combination of separated electronic units, which are sometimes bulk and redundant. In future studies, a compact and efficient electronic system is demanded. The electronic system requires accurate and simultaneous data acquisition from several channels. Current prototype design has a great bulk that is not suitable for implementation in underwater

robots, which usually have limited space and computing resources. Future works should consider designing the electronics using system-on-chip implementations like AD5933 or ADUCM350. These integrated devices may significantly shrink the sensor dimension and enable practical robotic applications.

Appendix A

List of Publications Arisen From This PhD Study

A.1 Journal Papers

Wang, Ke, Khac Duc Do, and Lei Cui. "Underwater Active Electrosense: A Scattering Formulation and its Application." *IEEE Transactions on Robotics* 33, no. 5 (2017): 1233-1241.

Wang, Ke, Khac Duc Do, and Lei Cui. "Identifying and Localizing Underwater Objects with Planar Active Electrosensor." *IEEE/ASME Transactions on Mechatronics*. (submitted)

A.2 Conference Papers

Wang, Ke, Khac Duc Do, and Lei Cui. "An Underwater Electrosensor for Identifying Objects of Similar Volume and Aspect Ratio Using Convolutional Neural Network." *Intelligent Robots and Systems (IROS), 2017 IEEE/RSJ International*

Conference on.

Wang, Ke, Lei Cui, and Khac Duc Do. "An underwater electrosensory membrane bio-inspired by weakly electric fish." *Intelligent Robots and Systems (IROS), 2016 IEEE/RSJ International Conference on*, pp. 4951-4956. IEEE, 2016.

Wang, Ke, Lei Cui, and Khac Duc Do. "A discrete dipole approximation approach to underwater active electrosense problems." *Intelligent Robots and Systems (IROS), 2016 IEEE/RSJ International Conference on*, pp. 1305-1312. IEEE, 2016. (**Best Paper Finalist**)

Bibliography

[1] Adler, A., J. H. Arnold, R. Bayford, A. Borsic, B. Brown, P. Dixon, T. J. Faes, I. Frerichs, H. Gagnon, Y. Gärber, et al. (2009). Greit: a unified approach to 2d linear eit reconstruction of lung images. *Physiological measurement 30*(6), S35.

[2] Adler, A. and W. R. Lionheart (2006). Uses and abuses of eidors: an extensible software base for eit. *Physiological measurement 27*(5), S25.

[3] Ammari, H., T. Boulier, and J. Garnier (2013). Modeling active electrolocation in weakly electric fish. *SIAM Journal on Imaging Sciences 6*(1), 285–321.

[4] Ammari, H., J. Garnier, W. Jing, H. Kang, M. Lim, K. Solna, and H. Wang (2013). *Mathematical and statistical methods for multistatic imaging*, Volume 2098. Springer.

[5] Ammari, H. and H. Kang (2003). Properties of the generalized polarization tensors. *Multiscale Modeling & Simulation 1*(2), 335–348.

[6] Ammari, H. and H. Kang (2004). *Reconstruction of small inhomogeneities from boundary measurements*. Springer.

[7] Assad, C. (1997). Electric field maps and boundary element simulations of electrolocation in weakly electric fish.

[8] Assad, C., B. Rasnow, and P. K. Stoddard (1999). Electric organ discharges and electric images during electrolocation. *Journal of Experimental Biology 202*(10), 1185–1193.

[9] Atkinson, K. E. (1997). *The numerical solution of integral equations of the second kind*, Volume 4. Cambridge university press.

[10] Baffet, G., F. Boyer, and P. B. Gossiaux (2009). Biomimetic localization using the electrolocation sense of the electric fish. In *Robotics and Biomimetics, 2008. ROBIO 2008. IEEE International Conference on*, pp. 659–664. IEEE.

[11] Bagshaw, A. P., A. D. Liston, R. H. Bayford, A. Tizzard, A. P. Gibson, A. T. Tidswell, M. K. Sparkes, H. Dehghani, C. D. Binnie, and D. S. Holder (2003). Electrical impedance tomography of human brain function using reconstruction algorithms based on the finite element method. *NeuroImage 20*(2), 752–764.

[12] Bai, Y., I. D. Neveln, M. Peshkin, and M. A. MacIver (2016). Enhanced detection performance in electrosense through capacitive sensing. *Bioinspiration & Biomimetics 11*(5), 055001.

[13] Bai, Y., J. Snyder, Y. Silverman, M. Peshkin, and M. A. MacIver. Sensing capacitance of underwater objects in bio-inspired electrosense. In *Intelligent Robots and Systems (IROS), 2012 IEEE/RSJ International Conference on*, pp. 1467–1472. IEEE.

[14] Bai, Y., J. Snyder, Y. Silverman, M. Peshkin, and M. A. MacIver (2012). Sensing capacitance of underwater objects in bio-inspired electrosense. In *Intelligent Robots and Systems (IROS), 2012 IEEE/RSJ International Conference on*, pp. 1467–1472. IEEE.

[15] Bai, Y., J. B. Snyder, M. Peshkin, and M. A. MacIver (2015). Finding and

identifying simple objects underwater with active electrosense. *The International Journal of Robotics Research 34*(10), 1255–1277.

[16] Barber, D. and B. Brown (1984). Applied potential tomography. *Journal of Physics E: Scientific Instruments 17*(9), 723.

[17] Bell, C., H. Zakon, and T. Finger (1989). Mormyromast electroreceptor organs and their afferent fibers in mormyrid fish: I. morphology. *Journal of Comparative Neurology 286*(3), 391–407.

[18] Borsic, A. (2002). *Regularisation methods for imaging from electrical measurements*. Ph. D. thesis, Oxford Brookes University.

[19] Boyer, F., P. B. Gossiaux, B. Jawad, V. Lebastard, and M. Porez (2012a). Model for a sensor inspired by electric fish. *IEEE transactions on robotics 28*(2), 492–505.

[20] Boyer, F., P. B. Gossiaux, B. Jawad, V. Lebastard, and M. Porez (2012b). Model for a sensor inspired by electric fish. *Robotics, IEEE Transactions on 28*(2), 492–505.

[21] Boyer, F. and V. Lebastard (2012). Exploration of objects by an underwater robot with electric sense. *Biomimetic and Biohybrid Systems*, 50–61.

[22] Boyer, F., V. Lebastard, C. Chevallereau, S. Mintchev, and C. Stefanini (2015). Underwater navigation based on passive electric sense: New perspectives for underwater docking. *The International Journal of Robotics Research 34*(9), 1228–1250.

[23] Boyer, F., V. Lebastard, C. Chevallereau, and N. Servagent (2013). Underwater reflex navigation in confined environment based on electric sense. *Robotics, IEEE Transactions on 29*(4), 945–956.

[24] Cherepenin, V., A. Karpov, A. Korjenevsky, V. Kornienko, Y. Kultiasov, A. Mazaletskaya, and D. Mazourov (2001). Preliminary static eit images of the thorax in health and disease. *Physiological measurement 23*(1), 33.

[25] Chew, W. C. (1995). *Waves and fields in inhomogeneous media*, Volume 522. IEEE press New York.

[26] Coombs, S. (2001). Smart skins: information processing by lateral line flow sensors. *Autonomous Robots 11*(3), 255–261.

[27] Dimble, K. D., J. M. Faddy, and J. S. Humbert (2014a). Electrolocation-based underwater obstacle avoidance using wide-field integration methods. *Bioinspiration & biomimetics 9*(1), 016012.

[28] Dimble, K. D., J. M. Faddy, and J. S. Humbert (2014b). Electrolocation-based underwater obstacle avoidance using wide-field integration methods. *Bioinspiration & biomimetics 9*(1), 016012.

[29] Dines, K. and R. J. Lytle (1981). Analysis of electrical conductivity imaging. *Geophysics 46*(7), 1025–1036.

[30] Emde, G. and T. Ringer (1992). Electrolocation of capacitive objects in four species of pulse-type weakly electric fish i. discrimination performance. *Ethology 91*(4), 326–338.

[31] Fano, R., L. Chu, and R. Adler (1968). *Electromagnetic Fields, Energy, and Forces*. Mit Press.

[32] Fikioris, J. G. (1965). Electromagnetic field inside a current-carrying region. *Journal of Mathematical Physics 6*(11), 1617–1620.

[33] Fuchs, M., R. Drenckhahn, H.-A. Wischmann, and M. Wagner (1998). An improved boundary element method for realistic volume-conductor modeling. *Biomedical Engineering, IEEE Transactions on 45*(8), 980–997.

[34] Greengard, L. and V. Rokhlin (1997). A new version of the fast multipole method for the laplace equation in three dimensions. *Acta numerica 6*, 229–269.

[35] Grychtol, B. and A. Adler. Fem electrode refinement for electrical impedance tomography. In *Engineering in Medicine and Biology Society (EMBC), 2013 35th Annual International Conference of the IEEE*, pp. 6429–6432. IEEE.

[36] Grychtol, B. and A. Adler (2013). Fem electrode refinement for electrical impedance tomography. In *Engineering in Medicine and Biology Society (EMBC), 2013 35th Annual International Conference of the IEEE*, pp. 6429–6432. IEEE.

[37] Harris, C. M. and A. G. Piersol (2002). *Harris' shock and vibration handbook, chapter 13*, Volume 5. McGraw-Hill New York.

[38] Hartinger, A. E., R. Guardo, and H. Gagnon (2012). Eit system and reconstruction algorithm adapted for skin cancer imaging. In *Information Science, Signal Processing and their Applications (ISSPA), 2012 11th International Conference on*, pp. 798–803. IEEE.

[39] Holder, D. S. (2004). *Electrical impedance tomography: methods, history and applications*. CRC Press.

[40] Hollmann, M., J. Engelmann, and G. von der Emde (2008). Distribution, density and morphology of electroreceptor organs in mormyrid weakly electric

fish: anatomical investigations of a receptor mosaic. *Journal of Zoology 276*(2), 149–158.

[41] Hopkins, C. (2009). Electrical perception and communication. *Encyclopedia of neuroscience 3*, 813–831.

[42] Illig, D. W., L. K. Rumbaugh, M. K. Banavar, W. D. Jemison, A. Giffin, and K. H. Knuth (2016). Blind signal separation for underwater lidar applications. In *AIP Conference Proceedings*, Volume 1757, pp. 060003. AIP Publishing.

[43] Ioffe, S. and C. Szegedy (2015). Batch normalization: Accelerating deep network training by reducing internal covariate shift. *arXiv preprint arXiv:1502.03167*.

[44] Jackson, J. D. (1975). *Electrodynamics*. Wiley Online Library.

[45] Jackson, J. D. (1999). *Classical electrodynamics*. Wiley.

[46] Jawad, B., P. B. Gossiaux, F. Boyer, V. Lebastard, F. Gomez, N. Servagent, S. Bouvier, A. Girin, and M. Porez (2010). Sensor model for the navigation of underwater vehicles by the electric sense. In *Robotics and Biomimetics (ROBIO), 2010 IEEE International Conference on*, pp. 879–884. IEEE.

[47] Julier, S. J. and J. K. Uhlmann (2004). Unscented filtering and nonlinear estimation. *Proceedings of the IEEE 92*(3), 401–422.

[48] Kahnert, F. M. (2003). Numerical methods in electromagnetic scattering theory. *Journal of Quantitative Spectroscopy and Radiative Transfer 79*, 775–824.

[49] Kao, T.-J., D. Isaacson, J. Newell, and G. Saulnier (2006). A 3d reconstruction algorithm for eit using a handheld probe for breast cancer detection. *Physiological measurement 27*(5), S1.

[50] Kellogg, O. *Foundations of Potential Theory, 1953*. Dover Publications.

[51] Khambampati, A. K., A. Rashid, U. Z. Ijaz, S. Kim, M. Soleimani, and K. Y. Kim (2009). Unscented kalman filter approach to tracking a moving interfacial boundary in sedimentation processes using three-dimensional electrical impedance tomography. *Philosophical Transactions of the Royal Society of London A: Mathematical, Physical and Engineering Sciences 367*(1900), 3095–3120.

[52] Lakhtakia, A. (1992a). General theory of the purcell-pennypacker scattering approach and its extension to bianisotropic scatterers. *The Astrophysical Journal 394*, 494–499.

[53] Lakhtakia, A. (1992b). Strong and weak forms of the method of moments and the coupled dipole method for scattering of time-harmonic electromagnetic fields. *International Journal of Modern Physics C 3*(03), 583–603.

[54] Lanneau, S., F. Boyer, V. Lebastard, and S. Bazeille (2017). Model based estimation of ellipsoidal object using artificial electric sense. *The International Journal of Robotics Research*, 0278364917709942.

[55] Lebastard, V., C. Chevallereau, A. Amrouche, B. Jawad, A. Girin, F. Boyer, and P. B. Gossiaux. Underwater robot navigation around a sphere using electrolocation sense and kalman filter. In *Intelligent Robots and Systems (IROS), 2010 IEEE/RSJ International Conference on*, pp. 4225–4230. IEEE.

[56] Lebastard, V., C. Chevallereau, A. Amrouche, B. Jawad, A. Girin, F. Boyer, and P. B. Gossiaux (2010). Underwater robot navigation around a sphere using electrolocation sense and kalman filter. In *Intelligent Robots and Systems (IROS), 2010 IEEE/RSJ International Conference on*, pp. 4225–4230. IEEE.

[57] Lionheart, W. R. (2004). Eit reconstruction algorithms: pitfalls, challenges and recent developments. *Physiological measurement 25*(1), 125.

[58] Lissmann, H. (1958). On the function and evolution of electric organs in fish. *Journal of Experimental Biology 35*(1), 156–191.

[59] Ma, Y., Z. Zheng, L.-a. Xu, X. Liu, and Y. Wu (2001). Application of electrical resistance tomography system to monitor gas/liquid two-phase flow in a horizontal pipe. *Flow Measurement and Instrumentation 12*(4), 259–265.

[60] MacIver, M. A., E. Fontaine, and J. W. Burdick (2004). Designing future underwater vehicles: principles and mechanisms of the weakly electric fish. *IEEE Journal of Oceanic Engineering 29*(3), 651–659.

[61] Maciver, M. A. and M. E. Nelson (2001). Towards a biorobotic electrosensory system. *Autonomous robots 11*(3), 263–266.

[62] McLeod, D., J. Jacobson, M. Hardy, and C. Embry (2013). Autonomous inspection using an underwater 3d lidar. In *Oceans-San Diego, 2013*, pp. 1–8. IEEE.

[63] Mintchev, S., C. Stefanini, A. Girin, S. Marrazza, S. Orofino, V. Lebastard, L. Manfredi, P. Dario, and F. Boyer (2012). An underwater reconfigurable robot with bioinspired electric sense. In *Robotics and Automation (ICRA), 2012 IEEE International Conference on*, pp. 1149–1154. IEEE.

[64] Münz, H. (1989). Functional organization of the lateral line periphery. In *The mechanosensory lateral line*, pp. 285–297. Springer.

[65] Murai, T. and Y. Kagawa (1985). Electrical impedance computed tomography based on a finite element model. *IEEE Transactions on Biomedical Engineering* (3), 177–184.

[66] Nelson, M. E. and M. A. Maciver (1999). Prey capture in the weakly electric fish apteronotus albifrons: sensory acquisition strategies and electrosensory consequences. *Journal of Experimental Biology 202*(10), 1195–1203.

[67] Purcell, E. M. and C. R. Pennypacker (1973). Scattering and absorption of light by nonspherical dielectric grains. *The Astrophysical Journal 186*, 705–714.

[68] Rasnow, B. (1996a). The effects of simple objects on the electric field of apteronotus. *Journal of Comparative Physiology A: Neuroethology, Sensory, Neural, and Behavioral Physiology 178*(3), 397–411.

[69] Rasnow, B. (1996b). The effects of simple objects on the electric field of apteronotus. *Journal of Comparative Physiology A 178*(3), 397–411.

[70] Rigaud, B., J.-P. Morucci, and N. Chauveau (1995). Bioelectrical impedance techniques in medicine. part i: Bioimpedance measurement. second section: impedance spectrometry. *Critical reviews in biomedical engineering 24*(4-6), 257–351.

[71] Schöberl, J. (1997). Netgen an advancing front 2d/3d-mesh generator based on abstract rules. *Computing and visualization in science 1*(1), 41–52.

[72] Servagent, N., B. Jawad, S. Bouvier, F. Boyer, A. Girin, F. Gomez, V. Lebastard, C. Stefanini, and P.-B. Gossiaux (2013). Electrolocation sensors in conducting water bio-inspired by electric fish. *IEEE Sensors Journal 13*(5), 1865–1882.

[73] Silverman, Y., J. Snyder, Y. Bai, and M. A. MacIver (2012). Location and orientation estimation with an electrosense robot. In *Intelligent Robots and Systems (IROS), 2012 IEEE/RSJ International Conference on*, pp. 4218–4223. IEEE.

[74] Simon, D. (2006). *Optimal state estimation: Kalman, H infinity, and nonlinear approaches*. John Wiley & Sons.

[75] Simon, D. (2010). Kalman filtering with state constraints: a survey of linear and nonlinear algorithms. *IET Control Theory & Applications 4*(8), 1303–1318.

[76] Smith, J., T. White, C. Dodge, J. Paradiso, N. Gershenfeld, and D. Allport (1998). Electric field sensing for graphical interfaces. *IEEE Computer Graphics and Applications 18*(3), 54–60.

[77] Smith, J. R., E. Garcia, R. Wistort, and G. Krishnamoorthy (2007). Electric field imaging pretouch for robotic graspers. In *Intelligent Robots and Systems, 2007. IROS 2007. IEEE/RSJ International Conference on*, pp. 676–683. IEEE.

[78] Snyder, J., Y. Silverman, Y. Bai, and M. A. MacIver (2012). Underwater object tracking using electrical impedance tomography. In *Intelligent Robots and Systems (IROS), 2012 IEEE/RSJ International Conference on*, pp. 520–525. IEEE.

[79] Solberg, J. R., K. M. Lynch, and M. A. MacIver (2007). Robotic electrolocation: Active underwater target localization with electric fields. In *Robotics and Automation, 2007 IEEE International Conference on*, pp. 4879–4886. IEEE.

[80] Solberg, J. R., K. M. Lynch, and M. A. MacIver (2008a). Active electrolocation for underwater target localization. *The International Journal of Robotics Research 27*(5), 529–548.

[81] Solberg, J. R., K. M. Lynch, and M. A. MacIver (2008b). Active electrolocation for underwater target localization. *The International Journal of Robotics Research 27*(5), 529–548.

[82] Srivastava, N., G. E. Hinton, A. Krizhevsky, I. Sutskever, and R. Salakhutdinov (2014). Dropout: a simple way to prevent neural networks from overfitting. *Journal of Machine Learning Research 15*(1), 1929–1958.

[83] Theremin, L. S. and O. Petrishev (1996). The design of a musical instrument based on cathode relays. *Leonardo Music Journal 6*(1), 49–50.

[84] Tikhonov, A. N., V. A. Arsenin, and F. John (1977). *Solutions of ill-posed problems*, Volume 14. Winston Washington, DC.

[85] Vedaldi, A. and K. Lenc (2015). Matconvnet: Convolutional neural networks for matlab. In *Proceedings of the 23rd ACM international conference on Multimedia*, pp. 689–692. ACM.

[86] von der Emde, G. (1990). Discrimination of objects through electrolocation in the weakly electric fish, gnathonemus petersii. *Journal of Comparative Physiology A 167*(3), 413–421.

[87] von der Emde, G. (1999). Active electrolocation of objects in weakly electric fish. *Journal of experimental biology 202*(10), 1205–1215.

[88] von der Emde, G. (2006). Non-visual environmental imaging and object detection through active electrolocation in weakly electric fish. *Journal of Comparative Physiology A 192*(6), 601–612.

[89] von der Emde, G. and H. Bleckmann (1992). Differential responses of two types of electroreceptive afferents to signal distortions may permit capacitance measurement in a weakly electric fish, gnathonemus petersii. *Journal of Comparative Physiology A 171*(5), 683–694.

[90] von der Emde, G. and S. Fetz (2007a). Distance, shape and more: recognition

of object features during active electrolocation in a weakly electric fish. *Journal of Experimental Biology 210*(17), 3082–3095.

[91] von der Emde, G. and S. Fetz (2007b). Distance, shape and more: recognition of object features during active electrolocation in a weakly electric fish. *Journal of Experimental Biology 210*(17), 3082–3095.

[92] von der Emde, G., K. Gebhardt, and K. Behr (2012). Non-visual orientation and communication by fishes using electrical fields: A model system for underwater robotics. In *Robotics and Automation (ICRA), 2012 IEEE International Conference on*, pp. 1143–1148. IEEE.

[93] von der Emde, G., S. Schwarz, L. Gomez, R. Budelli, and K. Grant (1998). Electric fish measure distance in the dark. *Nature 395*(6705), 890–894.

[94] Wang, J. J. (1982). A unified and consistent view on the singularities of the electric dyadic green's function in the source region. *IEEE Transactions on Antennas and Propagation 30*, 463–468.

[95] Wang, K., L. Cui, and K. D. Do (2016). An underwater electrosensory membrane bio-inspired by weakly electric fish. In *29rd IEEE/RSJ 2016 International Conference on Intelligent Robots and Systems, IROS 2016*.

[96] Wikipedia (2008). Absorption spectrum of liquid water — Wikipedia, the free encyclopedia. [Online; accessed 10-Oct-2017].

[97] Xu-Friedman, M. A. and C. D. Hopkins (1999). Central mechanisms of temporal analysis in the knollenorgan pathway of mormyrid electric fish. *Journal of Experimental Biology 202*(10), 1311–1318.

[98] York, T. (2001). Status of electrical tomography in industrial applications. *Journal of Electronic Imaging 10*(3), 608–619.

[99] Yurkin, M. A. and A. G. Hoekstra (2007). The discrete dipole approximation: an overview and recent developments. *Journal of Quantitative Spectroscopy and Radiative Transfer 106*(1), 558–589.

[100] Zhdanov, M. (2002). *Geophysical Inverse Theory and Regularization Problems*. Methods in Geochemistry and Geophysics. Elsevier Science.

[101] Zimmermann, E., A. Kemna, J. Berwix, W. Glaas, and H. Vereecken (2008). Eit measurement system with high phase accuracy for the imaging of spectral induced polarization properties of soils and sediments. *Measurement Science and Technology 19*(9), 094010.